In the name of God

Communications in Catalysis (Abbreviation: CIC) is an international, open access, online/printed scholarly biannual publication issued by the Department of Chemistry, Azarbaijan Shahid Madani University, Tabriz, Iran. High quality original papers in English dealing with experimental, theoretical and applied research related to catalysis science and technology are welcomed by CIC. This journal provides a forum for publication of original research papers, short communications, and critical reviews in all branches of chemical science and technology, on catalysts and their application in several areas, such as: organic, inorganic, bioorganic, analytical, polymer, etc. Publication process of the manuscripts submitted to CIC is free of charge. All the submitted manuscripts are peer-reviewed by the editorial board and reviewers of the CIC before acceptance for publication. To submit a new manuscript, please start by reading the journal instructions for authors (http: cic.azaruniv.ac.ir).

Prof. A. Salimi
(Department of Chemistry, Faculty of Science, University of Kurdistan, Kurdistan, Iran.)
Prof. H. Valizadeh
(Chemistry Department, Faculty of Science, Azarbaijan Shahid Madani University, Tabriz,Iran.)

Contents

Communications In Catalysis
Vol. 2, No. 1, 2023, pp.3-20
DOI: 10.22049/CIC.2023.28017.1027
Azarbaijan Shahid Madani University

Synthesis and Evaluation of Biological and Antioxidant Activity of Some New Heterocyclic Compounds of Mefenamic Drug Derivatives

Hala Shkyair Lihumis [1], Hayfaa A.Mubarak [2], Ameer A.Alameri [3*] Saadon Abdullah Aowda[4]

[1,2,3]Department of Chemistry, Faculty of science, University Babylon, Babylon, Iraq

[4]Department of Chemical engineering, Faculty of engineering, University Babylon, Babylon, Iraq

E-mail address: sci.hala.shkair@uobabylon.edu.iq

Received: 2022-09-23, Accepted: 2023-01-30

Abstract

In this study new heterocyclic derivatives were prepared. The most available Mefenamic acid (M) has been reacted with thionyl chloride to get (M1 compound). (M1) compound treated with hydrazinecarboxamide to get (M2) derivative then a ring closer reaction has been made to compound (M2) by NaOH solution to get the 1,2,4-triazole-3-ol ring compound (M3). Compound (M)reaction with phenyl hydrazine hydrate to give (M4) compound then a ring closer reaction have been made using carbon disulfide and hydrazine hydrate in basic media to get (M5) . Compound (M1) treated with 3-aminopropanoic acid to get (M6) compound. (M7) compound has been synthesis by reacting (M6) compound with benzaldehyde in the presence of acetic anhydride to get oxazin ring (M7 compound). The synthesized compounds' antibacterial activity and antioxidant activity (M1-M7) were examined using the (DPPH) technique. The compounds show substantial antioxidant activity equivalent to the well-known (ascorbic acid) (IC50=31.95 g/mL) employed.

Keywords: Mefenamic acid, Hydrazinecarboxamide, Phenylhydrazine, Oxazin, Antioxidant activity

Introduction

Mefenamic acid (MA) [$C_{15}H_{15}NO_2$] or Ponstan or 2-(2,3-Dimethyl phenyl) amino] benzoic acid is a non-steroidal anti-inflammatory drug (NSAID) used in acute conditions and chronic of inflammation and pain. MA belongs to the aromatic amino acids group (Figure 1) [1]. Mefenamic acid is a derivative of "anthranilic acid", is inhibits proliferation and triggers apoptotic cell death of several human carcinoma cell lines. In addition to the analgesic and antipyretic properties predictable of NSAIDS, MA has been exposed to be effective as therapeutic agent in carcinoma cell lines and Alzheimer's disease [2-5]. Mefenamic acid contains carboxylate and amino groups. It is used as a therapeutic drug for fever and inflammation pain such as pain after traumas or dental. In spite of the wide used, (NSAIDs) caused a large variation of toxicity which may include severe nephrotoxicity, hepatotoxicity, and (GI) tract disorders. All classical (NSAIDs) inhibit biosynthesis of prostaglandin, MA shows the identical effect that may be accountable for the anti- inflammatory, antipyretic and, analgesic properties of all traditional drugs of (NSAIDs) [6]. Oxazine is aromatic heterocyclic six-membered compounds and it is containing the oxygen atom and the nitrogen atom are both present in their composition. [7]. 1,2-oxazine offered a wide range of recreational activities, such as antibacterial, paradises [8-9]. Triazole an aromatic heterocyclic compound which including 5 membered cyclic system containing in their structure the 2 carbon atoms and 3 nitrogen atoms and has 2 isomers, which are very important compounds in medical and pharmaceutical chemistry and are considered to be among the compounds involved in the pharmaceutical industry [10-13].

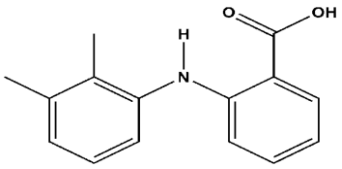

Figure 1. Chemical structure of Mefenamic acid

Experimental

Merck chemicals were purified and BDH was employed with KBr disk, "Testseon Shimadzu (FT- IR 8400Series Japan). The ^{1}HNMR spectra were obtained using DMSO as the solvent and TMS as the internal standard (Bruker, Ultra Shield 500 MHZ Switzerland).

Synthesis of 1- 2-((2,3-dimethylphenyl) amino) benzoyl chloride (M1) [6]

In 50 ml a round bottom flask with a reflux condenser, 0.01 mol of compound (M) was dissolved in 75 mL of $SOCl_2$, for 3 h and then the oil product was collected (Table 1).

Synthesis of 2-(2-((2,3-dimethylphenyl) amino) benzoyl)

hydrazine-1- carboxamide (M2) [4]

(0.03 mol) of hydrazine carboxamide and the 10% NaOH (75 mL) solution is mixed with stirring for 20 minutes. In 50 mL of dioxane, a mixture of (0.01 mol) of compound (M1) was dissolved dropwise for 30 minutes. With stirring for 24 h, ice water is added to the mixture, stirred for 30 minutes and acidified with HCl. The progress of the interaction was monitored by TLC. (Table 1).

Synthesis of 5-(2-((2,3-dimethylphenyl) amino) phenyl)-4H-1,2,4-triazol-3-ol (M3) [3]

For four hours, a combination of compound (W2) (0.01 mol) and NaOH 4% (0.03 mol) was refluxed and stirred and the mixture was allowed to be cool. The TLC was used to monitor the process while it was acidified with concentrated HCl and recrystallized from 100% ethyl alcohol. (Table 1).

Synthesis of 2-((2,3-dimethylphenyl) amino)-N'-phenylbenzohydrazide (M4) [10]

In a round bottom flask, 0.01mol of compound (M) was added, followed by a mixture of phenyl hydrazine (0.02 mol) and ethanol (40 ml). The mixture was then refluxed with stirring for five to six hours, after which the precipitate was dried and recrystallized from absolute ethyl alcohol (Table 1).

Synthesis of 5-(2-((2,3-dimethylphenyl) amino) phenyl)-4-(phenylamino)-4H-1,2,4-triazole-3-thiol (M5) [1]

Compound (M4) (0.01 mol) and CS_2 (0.02 mol, 1.52 mL) were mixed together with KOH (0.02 mol, 1.12 g) and ethyl alcohol (20 mL) for 12 h washing with diethyl ether and purified via water (10 mL) and then adding NH_2NH_2 80 % (0.02 mol, 0.64 g) for 1 h. The product was cooled and acidified with acetic acid, the excess solvent was evaporated with a rotary evaporator, TLC was used to trace the process, and 100% ethanol was recrystallized (Table 1).

Synthesis of (2-((2,3-dimethylphenyl) amino) benzoyl) glycine (M6) [4]

After that, a stirring solution of 3-aminopropanic acid (0.03 mol, 2.25 g) and NaOH was added to the compound (M5) (0.01 mol, 4.69 g) dissolved in dioxane (5 mL) and stirred overnight and then acidified with concentrated HCl. The solution was concentrated using a rotary evaporator. The response was monitored using TLC. After that, the remaining precipitate was dissolved in ethanol (Table 1).

Synthesis of (E)-2-(2-((2,3-dimethylphenyl) amino) phenyl)-5-styryl-2,5-dihydro-6H-1,3-oxazin-6-one (M7) [2]

Benzaldehyde (0.03 mol) was added to a combination of compounds (M6) (0.01 mol) with CH_3COOH (20 mL) and $(CH_3COO)_2O$ (80mL) and the mixture was refluxed for 6-7 h.TLC was employed to monitor the process, and absolute ethyl alcohol was recrystallized (Table 1).

Table 1. Some of physical properties of compounds (M1-M7).

Com. NO.	Molecular Formula	M.Wt	Color	m.p. °C	Yield%	Rf	(TLC)
M1	$C_{15}H_{14}ClNO$	259	Reddish-brown	Oily	97	--	--
M2	$C_{16}H_{18}N_4O_2$	314	Off -white	166-168	93	0.77	Acetone: n-hexane 1:2
M3	$C_{16}H_{16}N_4O$	296	Light brown	190-192	64	0.65	Benzene: acetone1:1
M4	$C_{21}H_{21}N_3O$	255	Green Yellowish	176-179	69	0.68	Acetone: n-hexane 1:2
M5	$C_{22}H_{21}N_5S$	311	Reddih Brown	190-192	54	0.7	Acetone: n-hexane 1:2
M6	$C_{18}H_{20}N_2O_3$	298	Yellow	188-189	64	0.62	n-hexane: $CHCl_3$ 1:1
M7	$C_{26}H_{24}N_2O_2$	384	Black	298 -202	86	0.76	petrolum ether: $CHCl_3$ 1:1

Results and discussion

Spectral investigation of Compound (M1)

The FTIR spectrum of M1) is shown in Figure 2. Compound M1 is identified by the appearance of OH band of carboxylic acid in (M) at 3404 -2400 cm^{-1} and the appearance of a new band at 1772 cm^{-1} that refers to the carbonyl group of acid chloride, NH at 3212 cm^{-1}, CH_{ar} at 3021 cm^{-1}, CH_{alph} at 2947-2826 cm^{-1}, C=C group at 1577cm-1-1492 cm^{-1}, C-N at 1353 cm^{-1}, C-O group at 1224-1246 cm^{-1}, and C-O group at 1224-1246 cm^{-1}.

Spectral investigation of Compound (M2)

The FTIR spectrum of M2 is shown in Figure 3. The compound M2 is identified by the appearance of CO-Cl at 1772 cm^{-1}, NH_2 at 3307 cm^{-1} and NH at 3214 cm^{-1}, C-H_{ar} at 3008 cm^{-1}, CH_{alph} at 2850-2975 cm^{-1}, C=C_{ar} at 1573 cm^{-1}, NH-C=O at 1647 cm^{-1}, C-N at 1358 cm^{-1}, and C-O at (1191- 1256 cm^{-1}.

^{1}HNMR spectrum of the compound M2 is shown in Figure 4. Singlet peaks at 3.57 ppm owing to CH_3 and at 7.39-7.82 ppm is for $CH_{ar.}$ Peak at 8.09 ppm is owed to O=C-NH, 8.23 ppm for (NH_2), 2.02 ppm of O =C-NH, and 2.04 ppm of NH.

Spectral investigation of Compound (M3)

The FTIR spectrum of M3 is shown in Figure 5. Compound M3 is identified by appearance of NH group at 3248 cm^{-1}, OH group at 3413 cm^{-1}, C=C at 1588 cm^{-1}, CH_{alph} at 2922-2985cm^{-1}, CH_{ar} at 3081 cm^{-1}, C=N at 1620 cm^{-1}, C-N at 1360 cm^{-1}, 1220-1269 cm^{-1} to C-O.

^{1}HNMR spectrum of M3 is shown in Figure 6. Signals appeared are attribute to CH_3 at 3.79 ppm, $CH_{ar.}$ at 7.39-8.10 ppm, OH at 10.48 ppm, NH_{trizol} at 11.52 ppm, NH at 8.73 ppm.

^{13}CNMR spectrum of M3 is shown in Figure 7. Signals at 50.79 ppm and 50.00 are related

to C-triazol, C_{ar} at 127.75-142.84 ppm, 158.02 ppm of C-OH in triazol ring, 50.52 ppm of CH_3 and NH at 161.95 ppm.

Spectral investigation of Compound (M4)

The FTIR spectrum of M4 is shown in Figure 8. OH, band of COOH in (M) is at 3448-2400 cm^{-1}, NH at 3266- 3175 cm^{-1}, CONH at 1626 cm^{-1}, C=C at 1588 cm^{-1}, CH_{alph} at 2992-2864 cm^{-1}, CH_{ar} at 3075 cm^{-1}, C-N at 1337 cm^{-1}, C-O at 1196-1307 cm^{-1}.

^{1}HNMR spectrum of M4 is shown in Figure 9 which demonstrated that the singlet signal of OH had vanished OH at 11.07 ppm in carboxylic group of (M), NH at 8.67 ppm, O=C-NH at 8.71 ppm and CH_3 at 3.45 ppm, and $(CH)_{ar.}$ at 7.46-7.89 ppm.

Spectral investigation of Compound (M5)

The FTIR spectrum of M5 is shown in Figure 10. It is shown that SH group is at 2063.83 cm^{-1}, NH at 3317- 3290 cm^{-1}, $C=C_{ar}$ at 1519 cm^{-1}, C=N at 1677 cm^{-1}, CH_{alph} at 2959-1868 cm^{-1}, CH_{ar} at 3090- 1408cm^{-1}, C-N at 1245,1287 cm^{-1}.

^{1}HNMR spectrum of M5 is shown in Figure 11. Appeared signals are for NH at 8.30 ppm, and CH_3 at 3.74 ppm, and CH_{ar} at 7.21-7.73 ppm, SH at 13.73 ppm.

^{13}CNMR spectrum of M5 is shown in Figure 12. Signal at 51.46 is related to NH-C, $CH_{ar.}$ at 125.90-135.89 ppm, C-SH at 178.34 ppm, N=C -N at 159.48 ppm.

Spectral investigation of Compound (M6)

The FTIR spectrum of M6 in shown in Figure 13. The compound M6 is identified by appearance of oH band of COOH at 3433-2622 cm^{-1}, NH at 3204- 3122 cm^{-1}, C=O acid and amide at 1710 cm^{-1} and 1625 cm^{-1}, $C=C_{ar}$ at 1544 cm^{-1}, CH_{alph} at 2970- 2857 cm^{-1}, CH_{ar} at 3031 cm^{-1}, 1382 cm^{-1} to C-N, C-O at 1218 -1268 cm^{-1}.

^{1}H-NMR spectrum of M6 is shown in Figure 14. Signals of HN-CH_2COOH at 4.65 ppm, N-NH, at 2.05 ppm, CH_3 at 3.65 ppm, CH_{ar} at 7.34- 8.15, O=C-NH-CH_2 at 8.73 ppm, and signal OH of COOH group at 11.47 ppm are shown respectively.

Spectral investigation of Compound (M7)

The IR spectrum of M7 is shown in Figure 15. OH, of acid at 3433-2400 cm^{-1}) and C=N at 1586 cm^{-1}, 3266 cm^{-1} to NH, CH at 2938-2864 cm^{-1}, CH_{ar} at 3006 cm^{-1}, C=O ester at 1731 cm^{-1}, 1492 cm^{-1} to C=C, C-N at 1335 cm^{-1} and C-O at 1205 cm^{-1} are represented.

^{1}HNMR spectrum of M7 is represented in Figure 16 showing that CH_3 signal at 3.63ppm, $CH_{ar.}$ at 7.47-7.63 ppm, s,3H CH=C, s,2HCH=C at 7.65 ppm, 7.90 ppm and NH at 7.53 ppm are appeared.

^{13}CNMR spectrum of M7 is shown in Figure 17, representing CH=C signal are appeared at 113.51 ppm, 113.51 ppm, $CH_{ar.}$ at 123.51-135.21 ppm,128.90 ppm-135.82 ppm, Coxazol ring at 131.65 ppm, C=O at 169.07-169.08 ppm, O-C=N at 171.07- 169.14 ppm, and C-NH at 168.59 ppm.

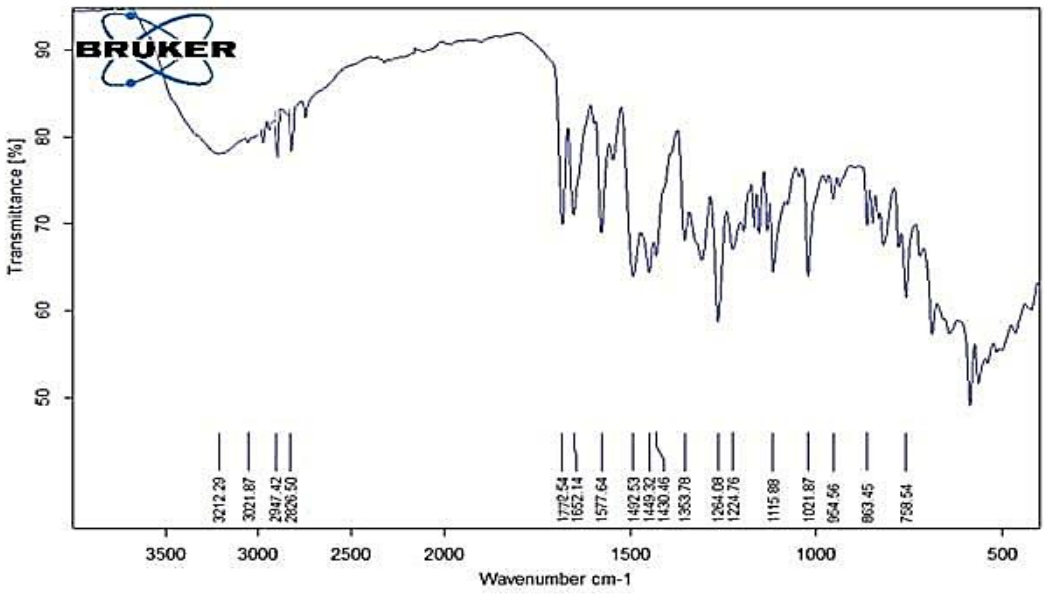

Figure 2**.** FTIR spectrum of M1

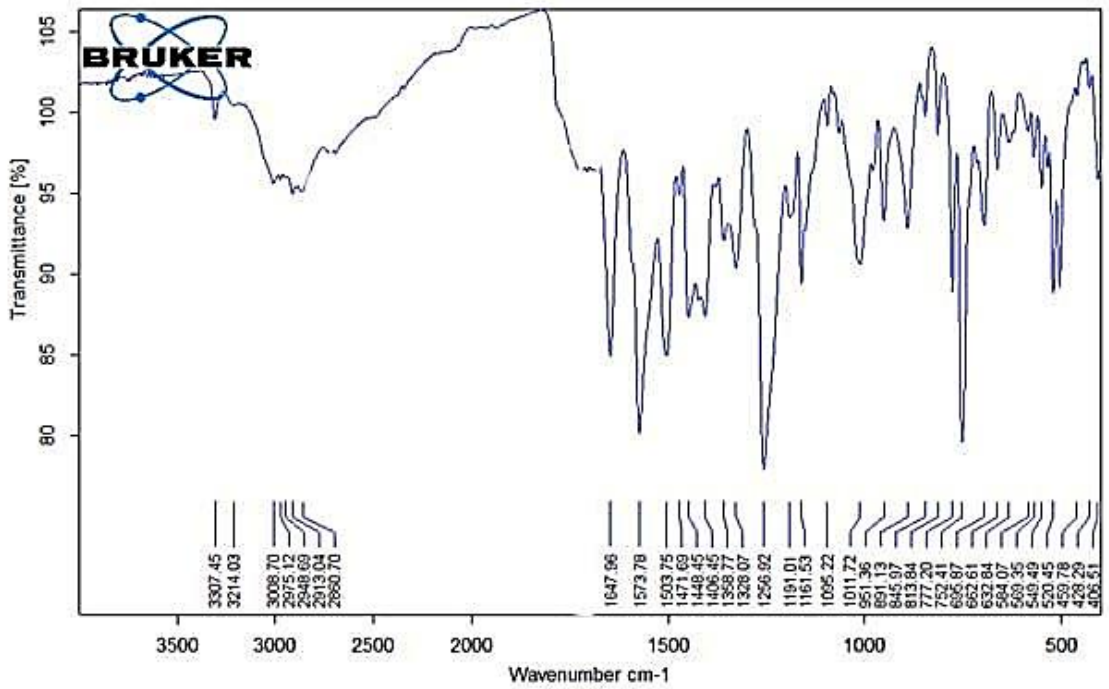

Figure 3. FTIR spectrum of M2

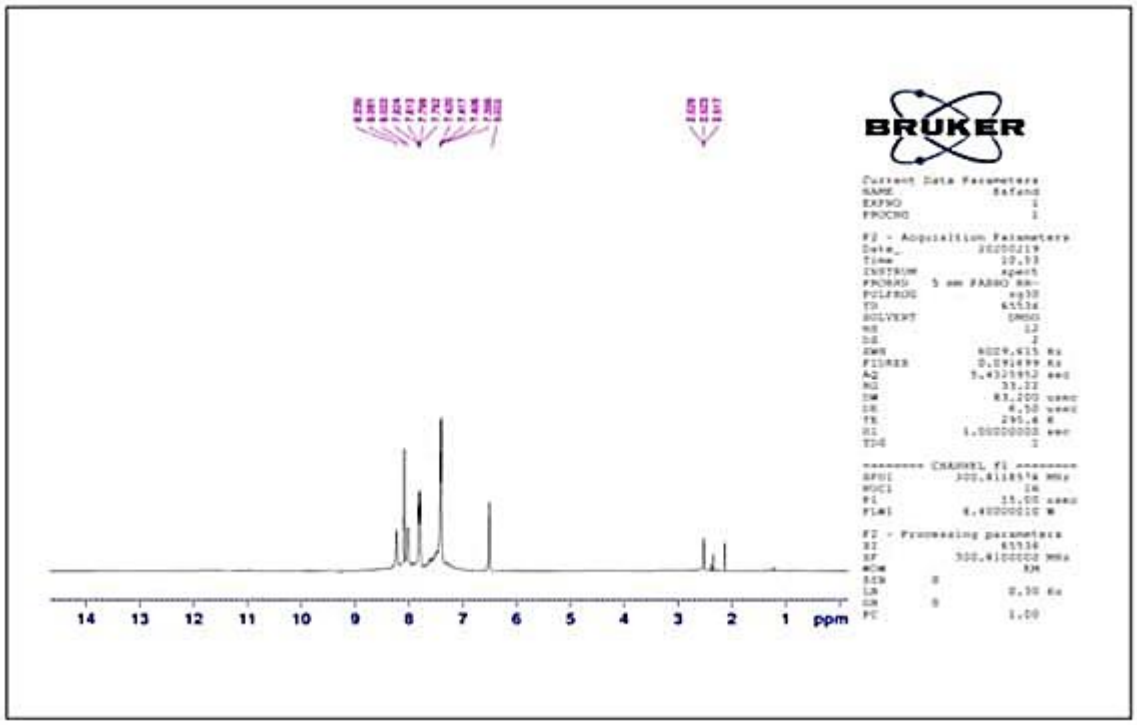

Figure 4. [1]HNMR spectrum of M2

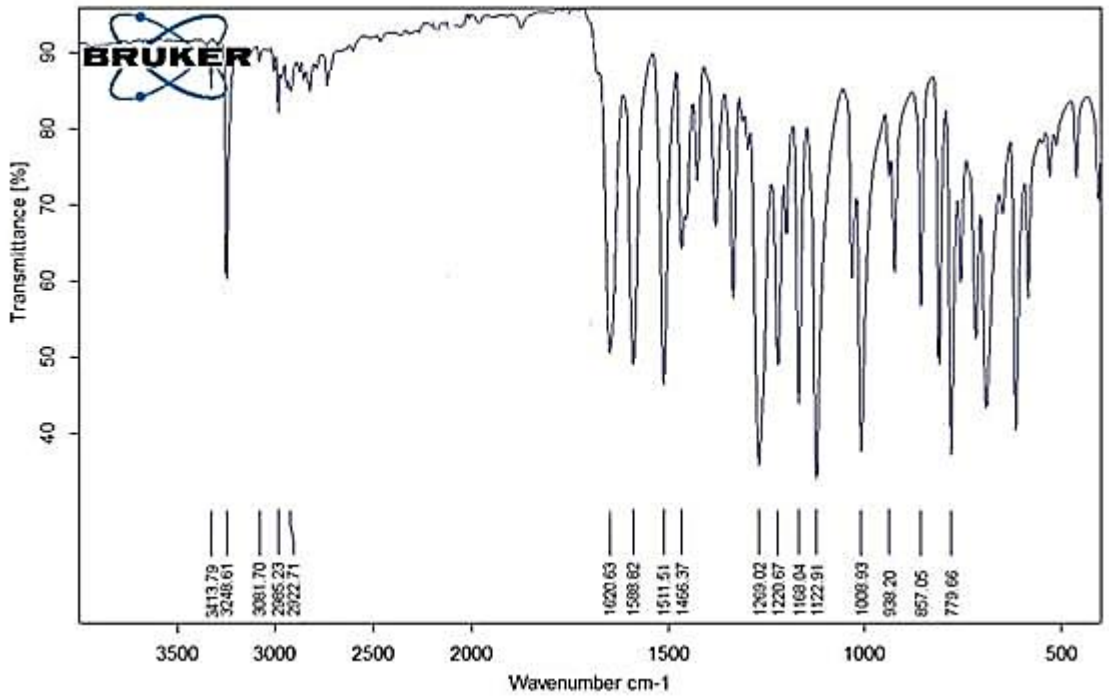

Figure 5. FT-IR spectrum of M3

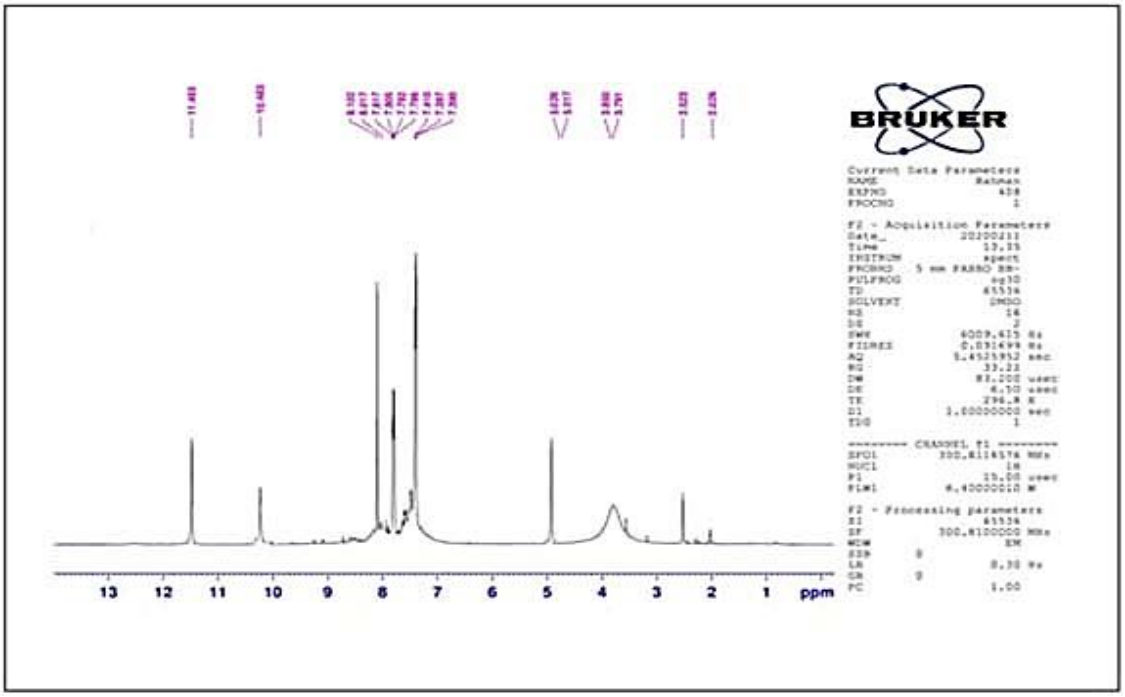

Figure 6. [1]HNMR spectrum of M3

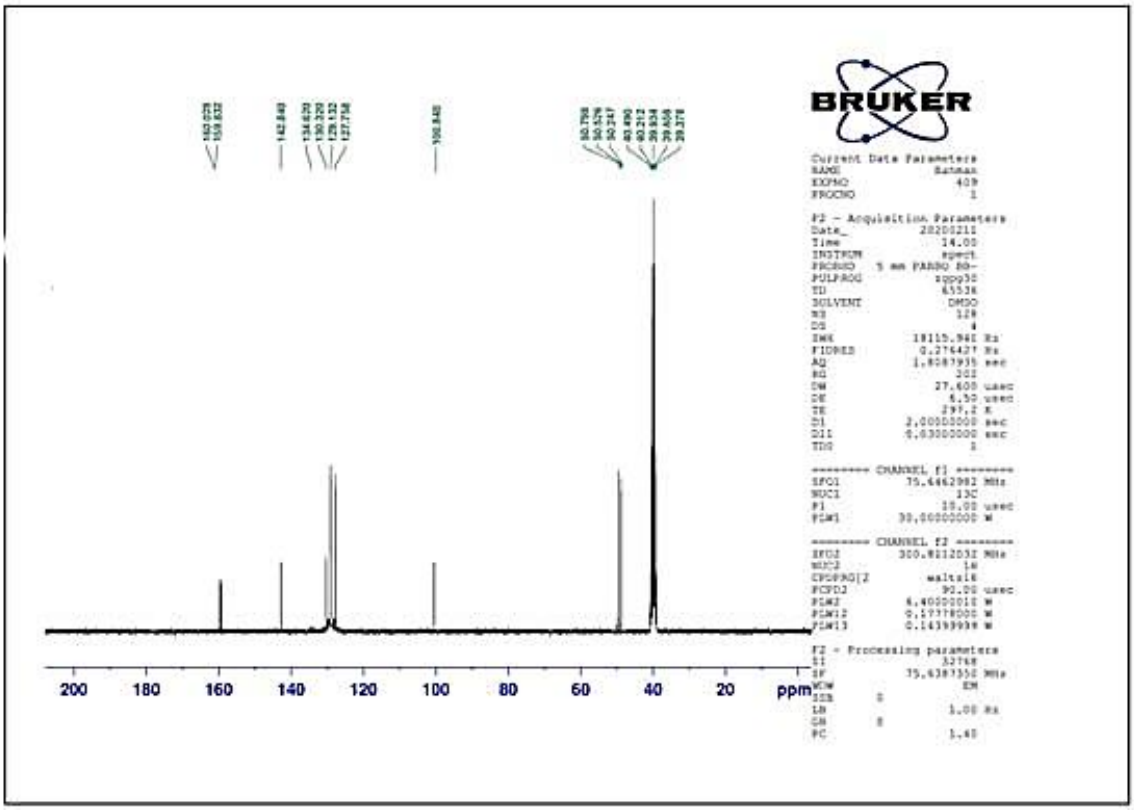

Figure 7. [13]CNMR spectrum of M3

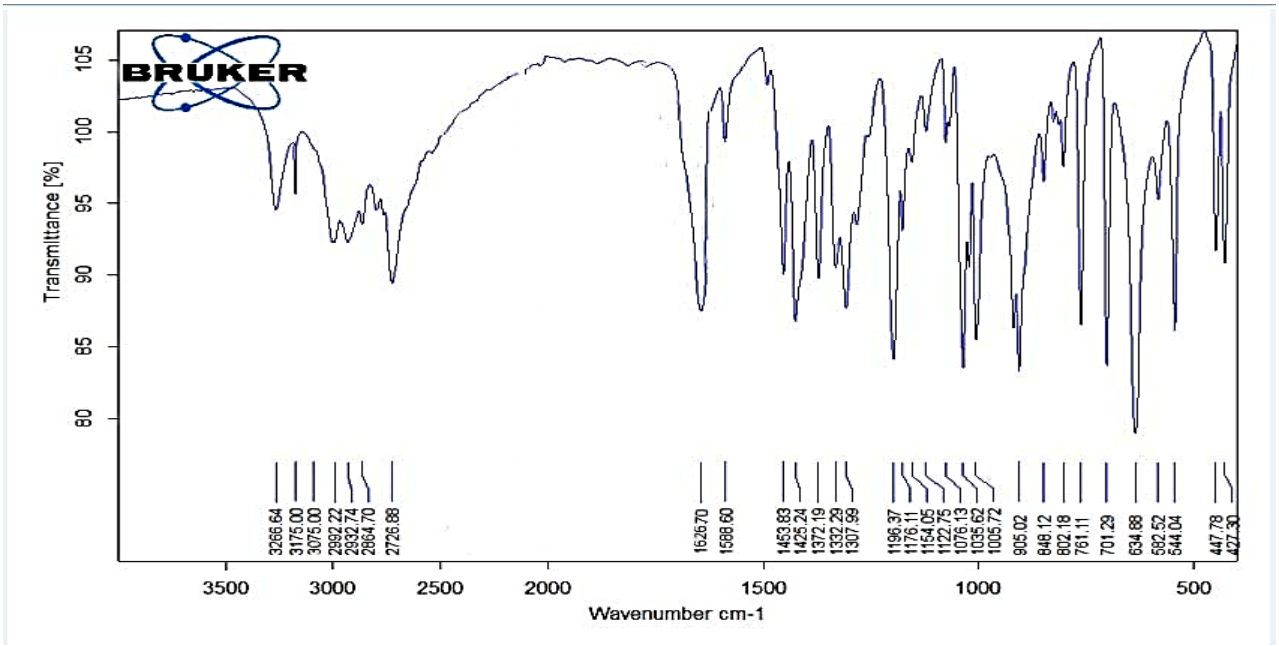

Figure 8. FT-IR spectrum of M4

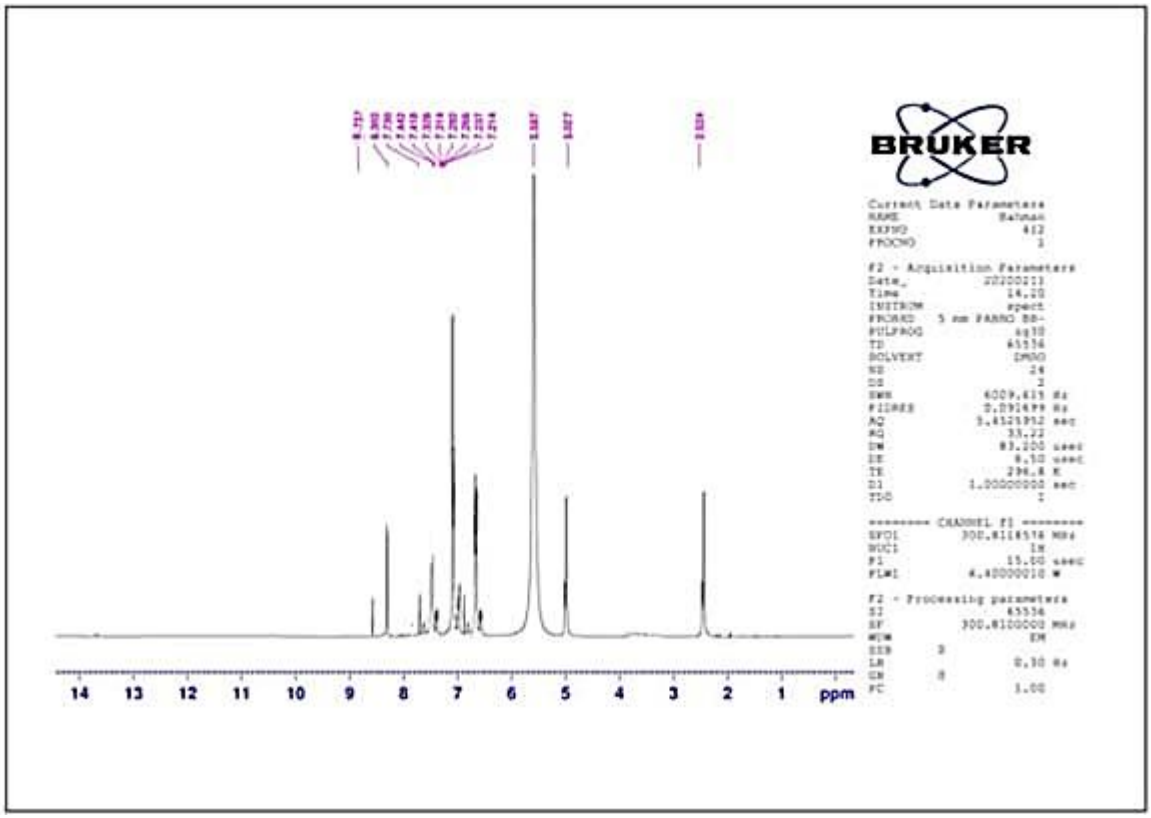

Figure 9. [1]HNMR spectrum of M4

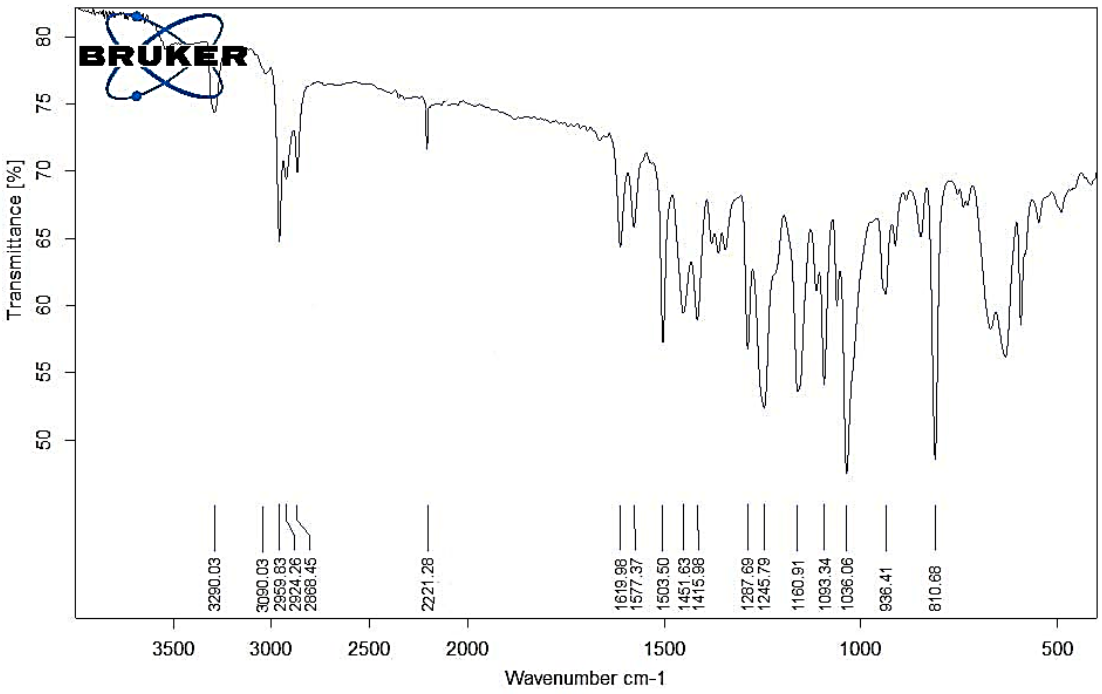

Figure 10. FTIR spectrum of M5

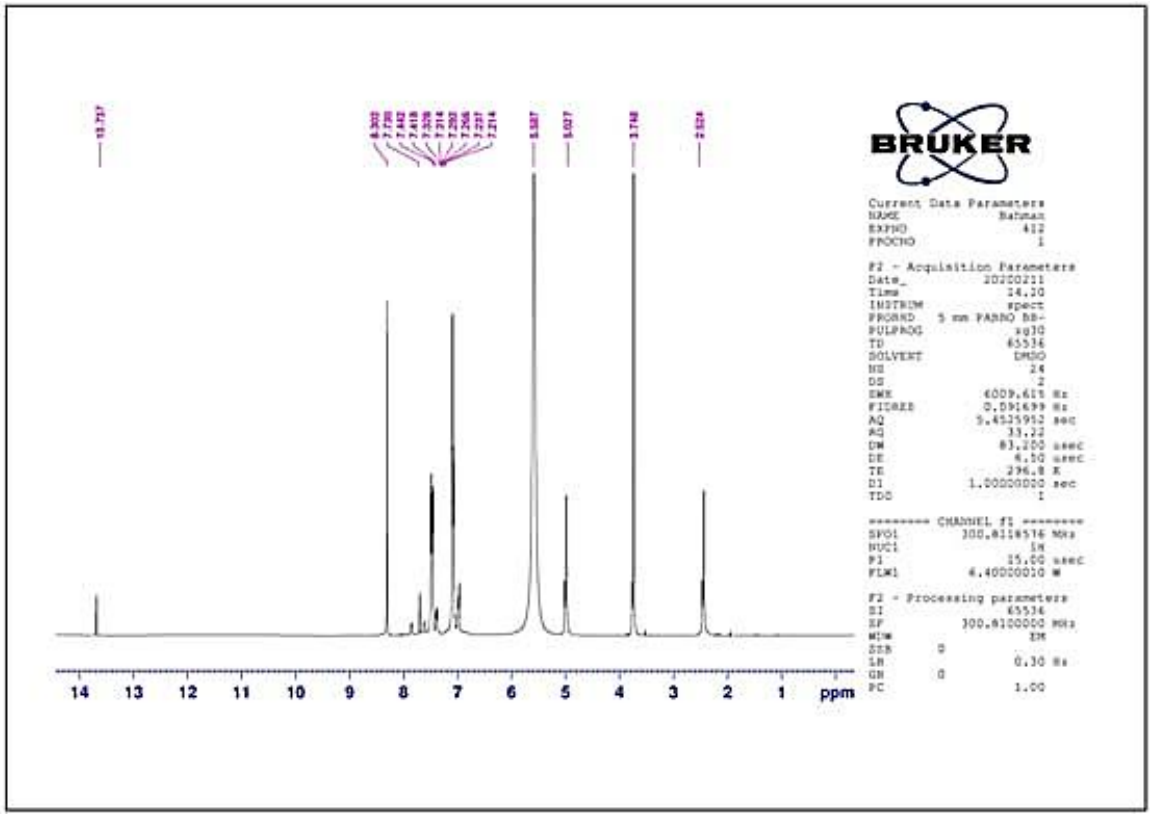

Figure 11. [1]HNMR spectrum of M5

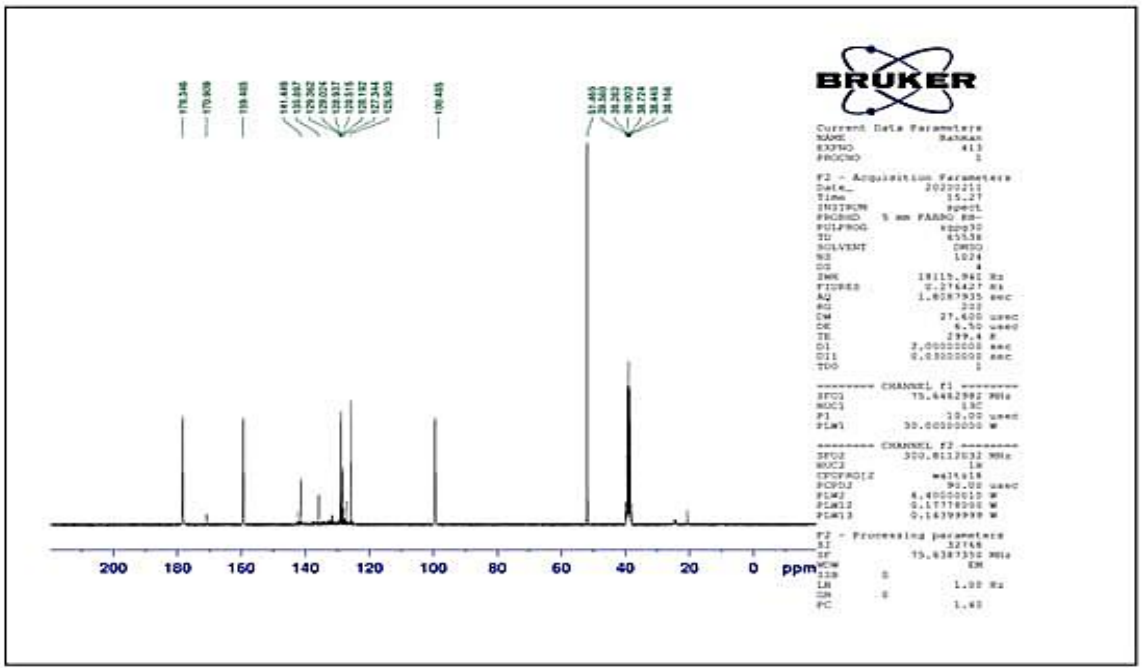

Figure12. ^{13}CNMR spectrum of M5

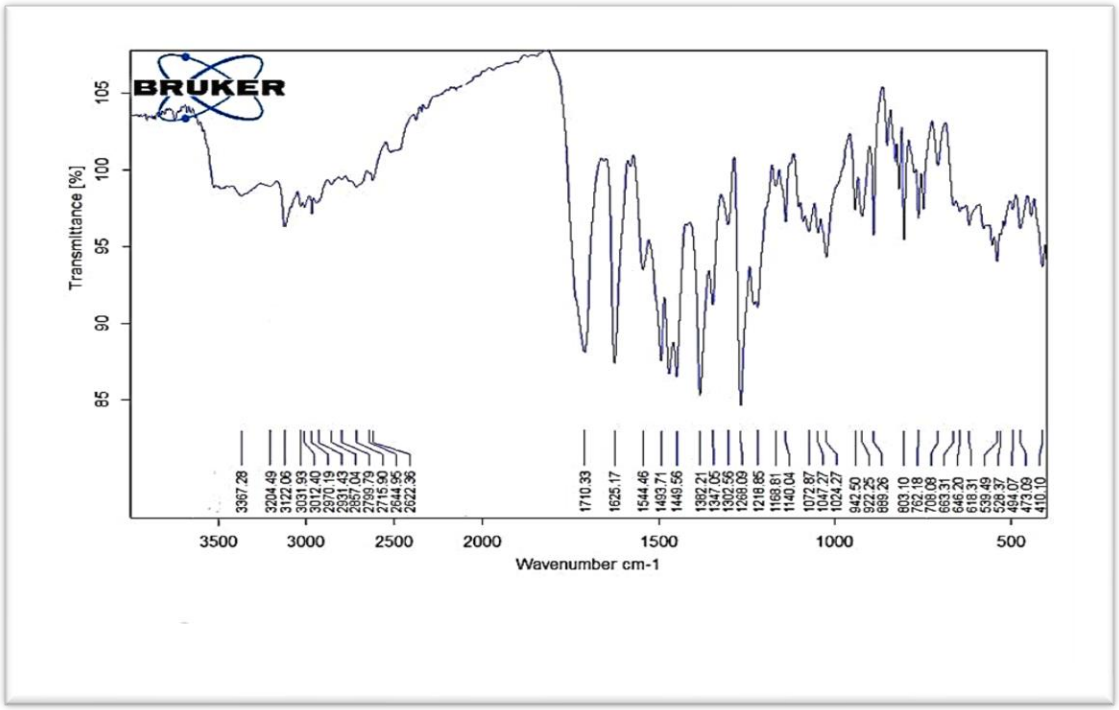

Figure 13. FTIR spectrum of M6

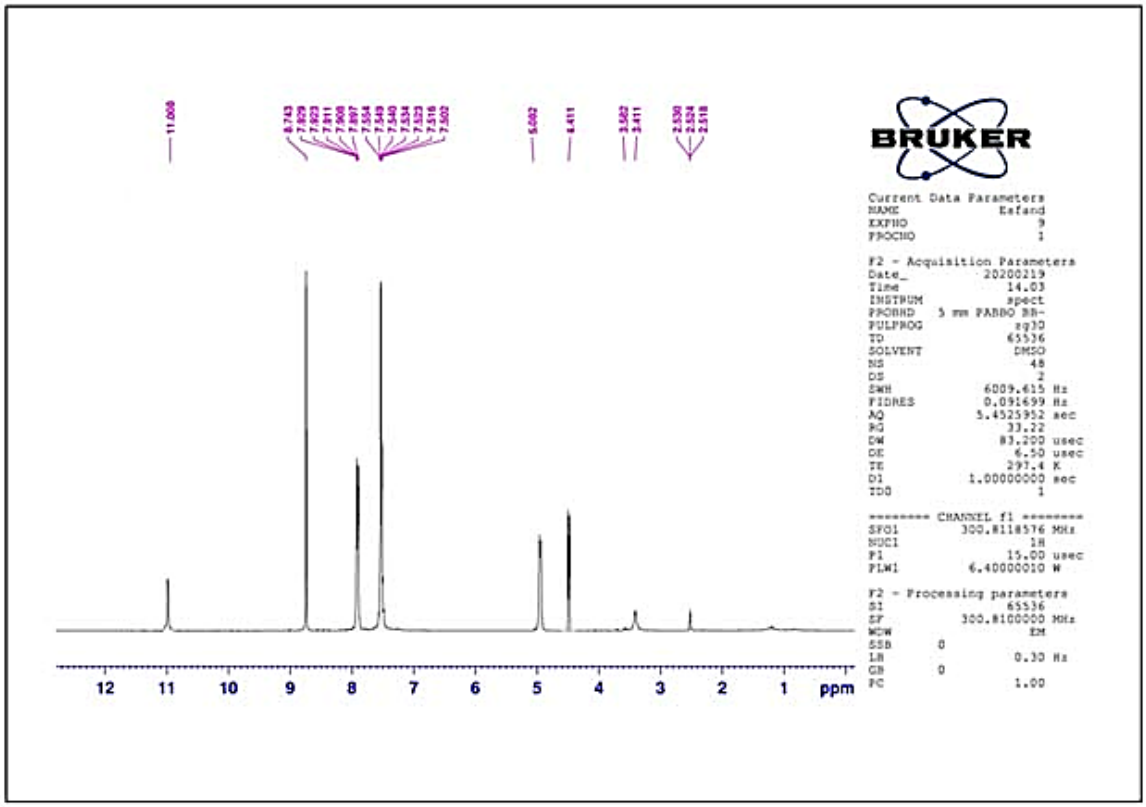

Figure 14. [1]HNMR spectrum of M6

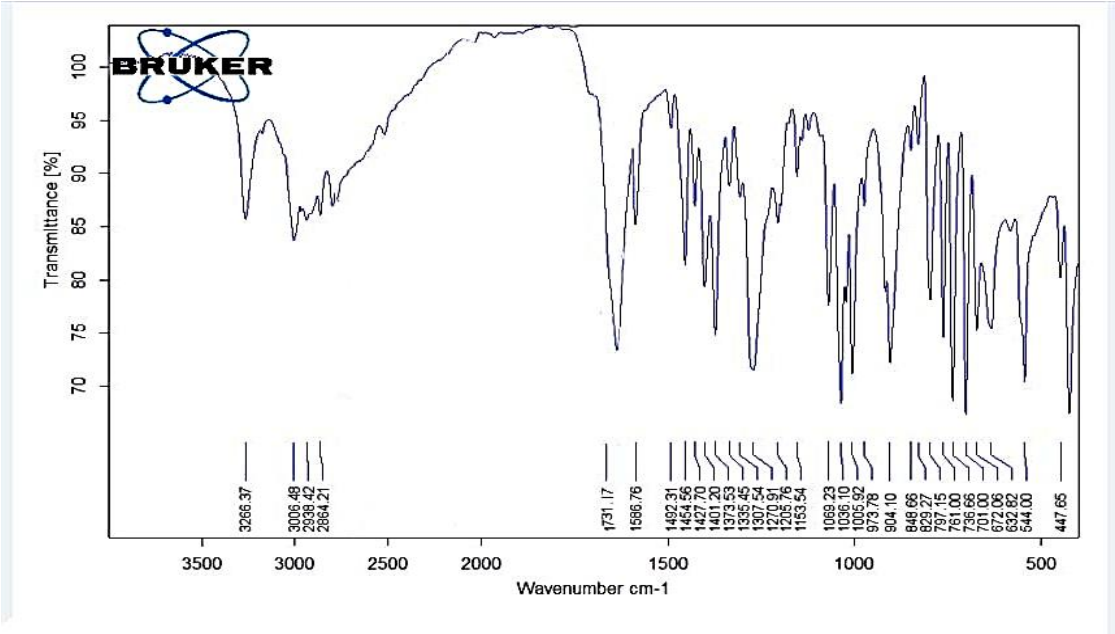

Figure 15. FTIR spectrum of M7

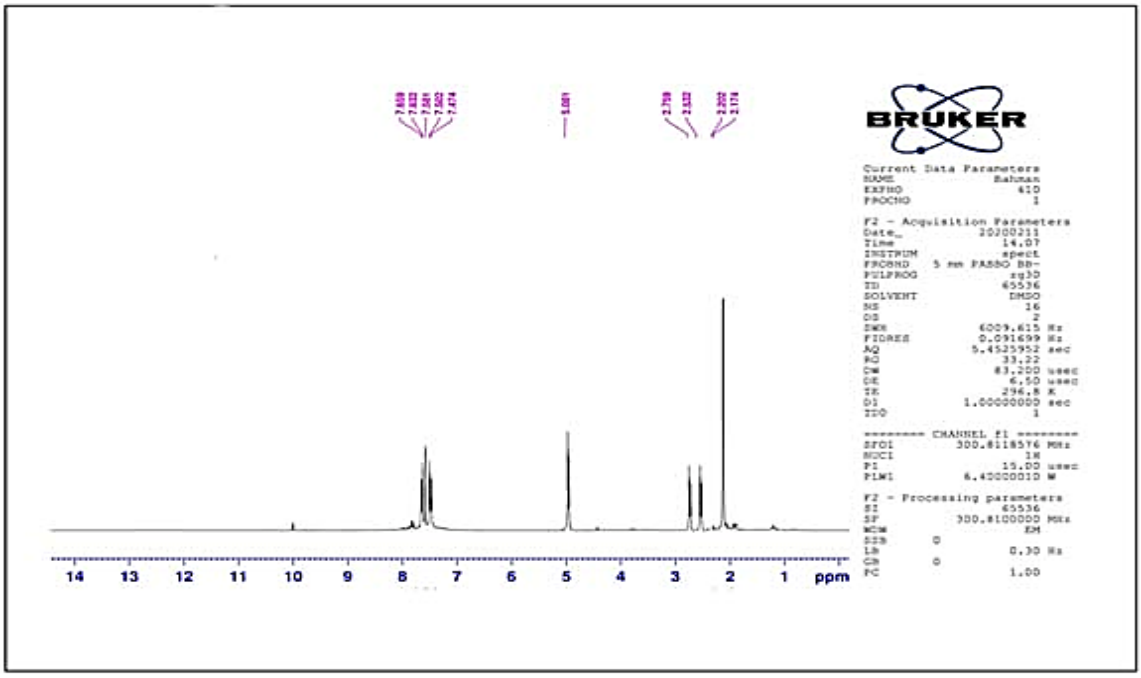

Figure 16. [1]HNMR spectrum of M7

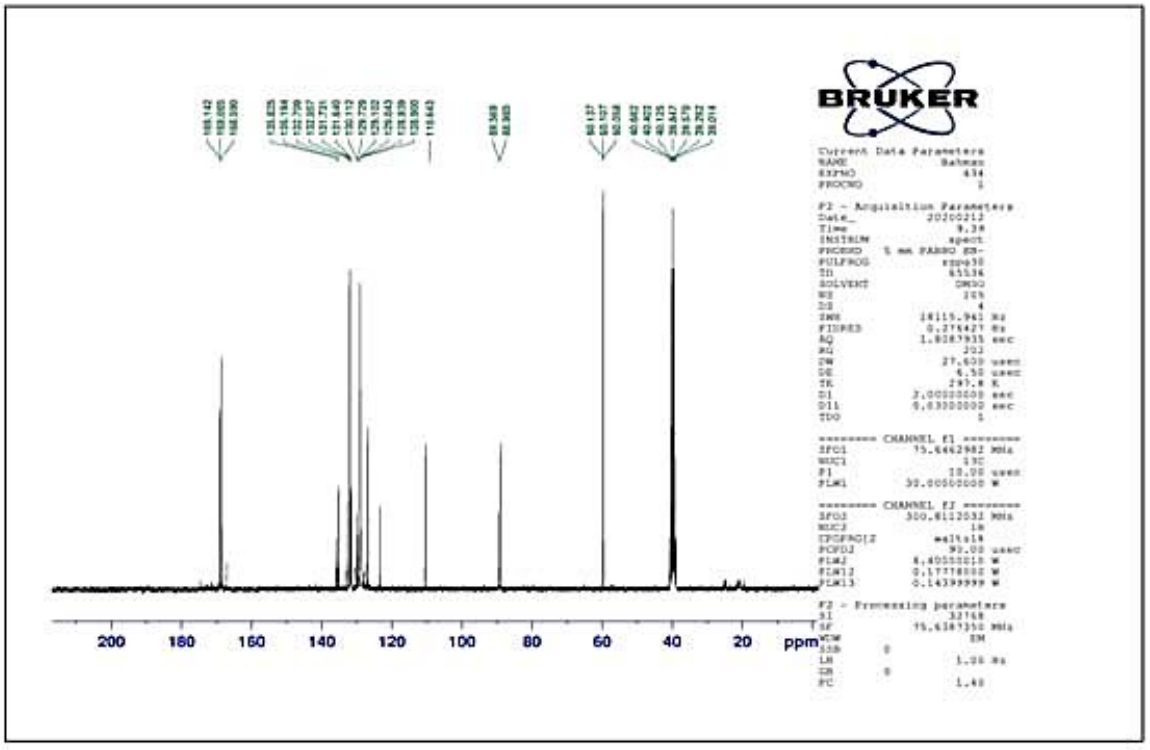

Figure 17. [13]CNMR spectrum of M7

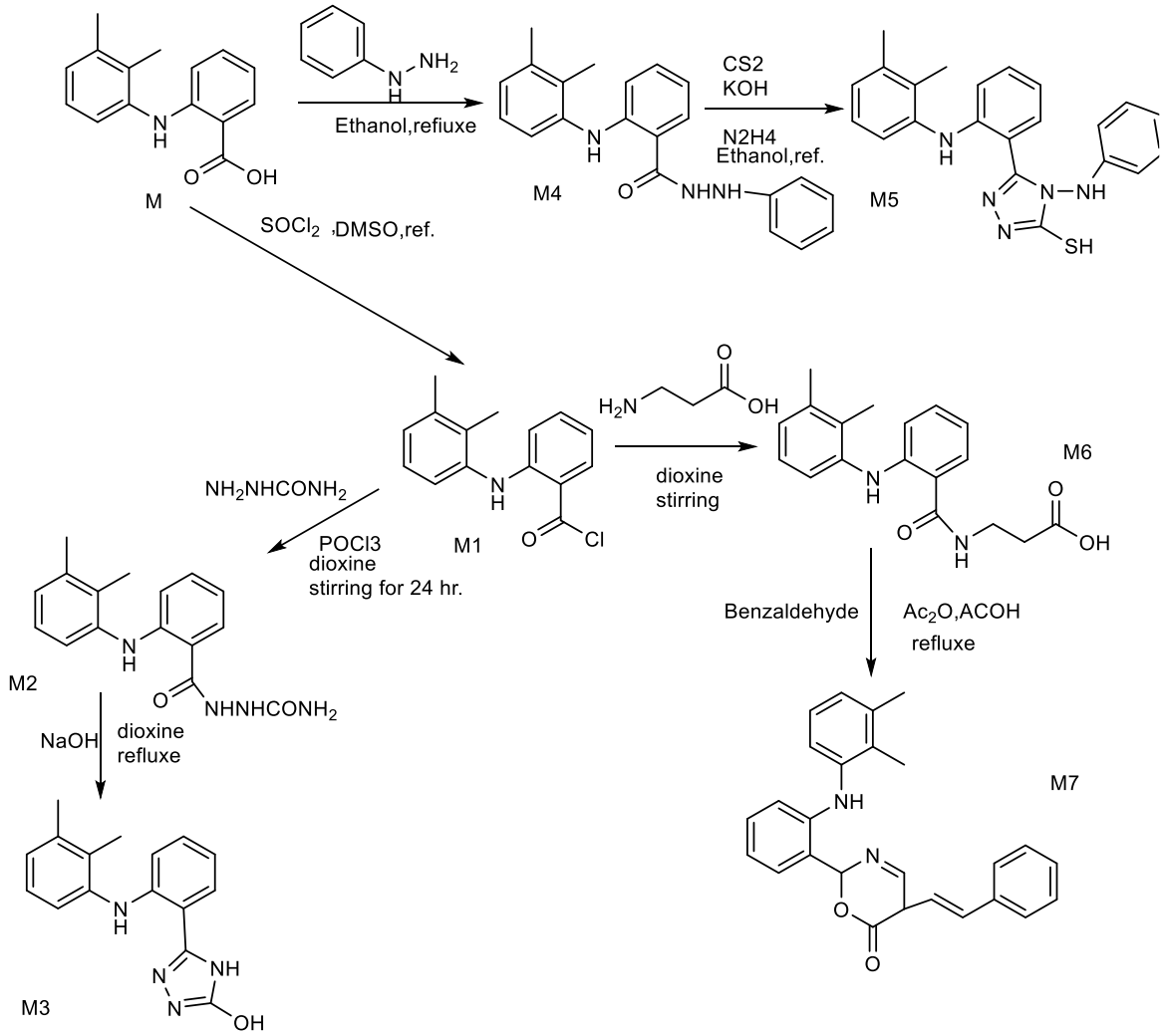

Scheme 1. Synthesis of Compounds M1-M7

Biological productivity

The biological activity was studied E. coli (G-) and Staph. Aureus (G+) are two species of bacteria, the compounds (M2, M3, M4, M5, M6) were found to inhibit the growth of(G-), the compounds (M2, M3, M6, M7) were found to have high activity against (G+), when compared with the biological activity of ciprofloxacin.

Table 2. The biological activity of (M1-M7) compounds

Comp. No.	Escherichia coli	Staphylococcus aureus
Ciprofloxacin (Antibiotic) Standard	12	18
M1	10	16
M2	14	20
M3	12	18
M4	15	14
M5	14	10
M6	28	24
M7	10	25

Figure 18. Biological Effect of compounds

Antioxidant Action

The standard DPPH approach was used to perform the antioxidant operation on the compounds. [13]. A standard solution of DPPH (1.3 mg/mL) was prepared in MeOH, and 100 mL DPPH was added to 3 mL MeOH. (25, 50, 75, and 100 µg\mL) were prepared, the tubes were exposed to light for 30 minutes and the absorbance was measured at 517 nm on a "UV-VIS spectrophotometer. Figure 19 and Table 3, showed the compounds (M1-M7) have moderate to high antioxidant activity due to OH, NH and SH

groups with compared to normal (ascorbic acid) activity (IC50=31.95 µg\mL).

Table 3. Antioxidant activity of (M1-M7) compounds

Conc. µg\mL	M1	M2	M3	M4	M5	M6	M7	STD (Ascorbic acid)
25	46.76	49.41	51.34	41.44	46.35	40.42	38.24	46.12
50	47.83	56.42	58.21	50.25	59.22	41.63	59.52	60.14
75	50.77	61.26	67.23	61.32	60.16	59.73	62.7	65.01
100	66.21	68.44	73.11	70.65	67.18	66.22	69.81	78.3
IC50 µg\mL	43.09	29.82	24.91	48.72	34.24	58.28	45.11	31.95

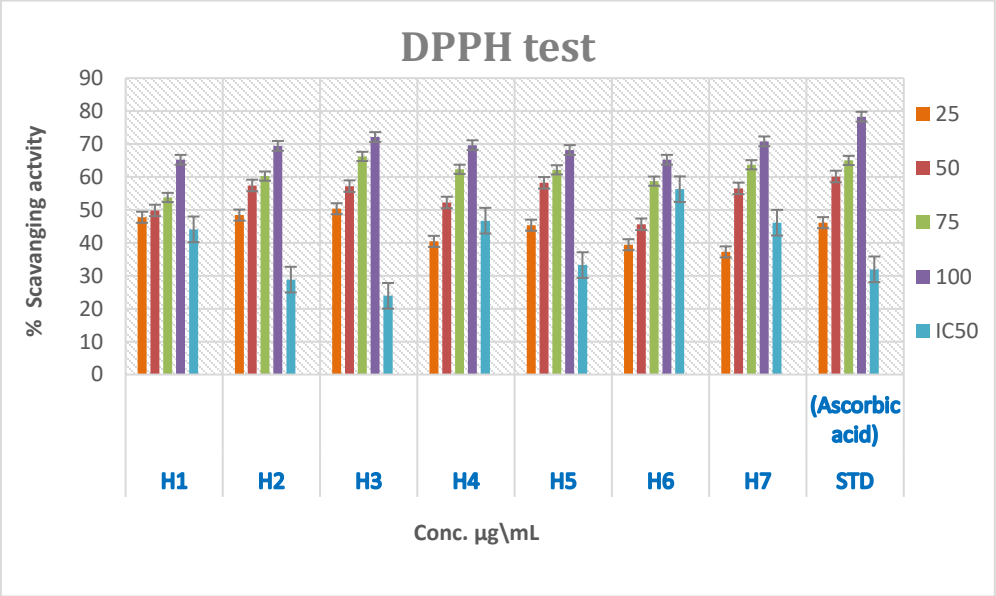

Figure 19. DPPH test of compounds (M1-M7).

Conclusion

New derivatives can be prepared due to the presence of effective groups The ratio of productions was good and useful for the continuation of the next step. Compounds possess significant antioxidant and antibacterial activity.

Acknowledgements

The authors thank for Babylon University (collage of science) and Ministry of Higher Education Iraq for support this research.

Research Funding
This work wasn't financially supported

Conflict of Interest
No conflict of interest was declared by the authors.

Disclosure statement

No potential conflict of interest was reported by the authors

References
[1] Domirbas N., Domirbas A., Karaoylu S. Celik E. Arkivoc, 2005, 75- 91.
[2] Figueroa-Valverde Lauro, Díaz-Cedillo Francisco, Rosas-Nexticapa Marcela, García-Cervera Elodia,1 Pool-Gómez Eduardo, López-Ramos María,Hau-Heredia Lenin, J. chem. 2014, 2-9.
[3] Hussain A. K. Sharba , Rida H.Al-Bayati ,Nadjet Rezki & Mohammed R. Aouad, 2005, 10,1155-1156.
[4] Katritzky, A. R., Yoshioka-Tarver, M., El-Gendy, B. E. D. M., & Hall, C. D. 2011, 2224-2227.
[5] Mizushima, T. 2010, 1614-1636.
[6] Mohammed Ridha Abood, Shireen Ridha Rasool, 2016, 7, 5
[7] Murti Y., Yogi B. & Pathak D, 2014, 3452-3454.
[8] Pavia, D. L., Lampman, G. M., Kriz, G. S., & Vyvyan, J. A, 2008
[9] Priyanka Bose, Vinod K. Tiwari, 2011
[10] Rana N., Nagham M. Aljamali , J. Majid. 2014,664-676
[11] Sriamomsak P., Limmatvapirat S., Piriyaprasarth S., Mansukmanee P. & Huang Z, 2015, 121-127.
[12] Shah K, Shrivastava SK & Mishra P, 2014, 70-77
[13] You-Chen Lin, Joshua G. 2022, 480-529.

Graphical abstract

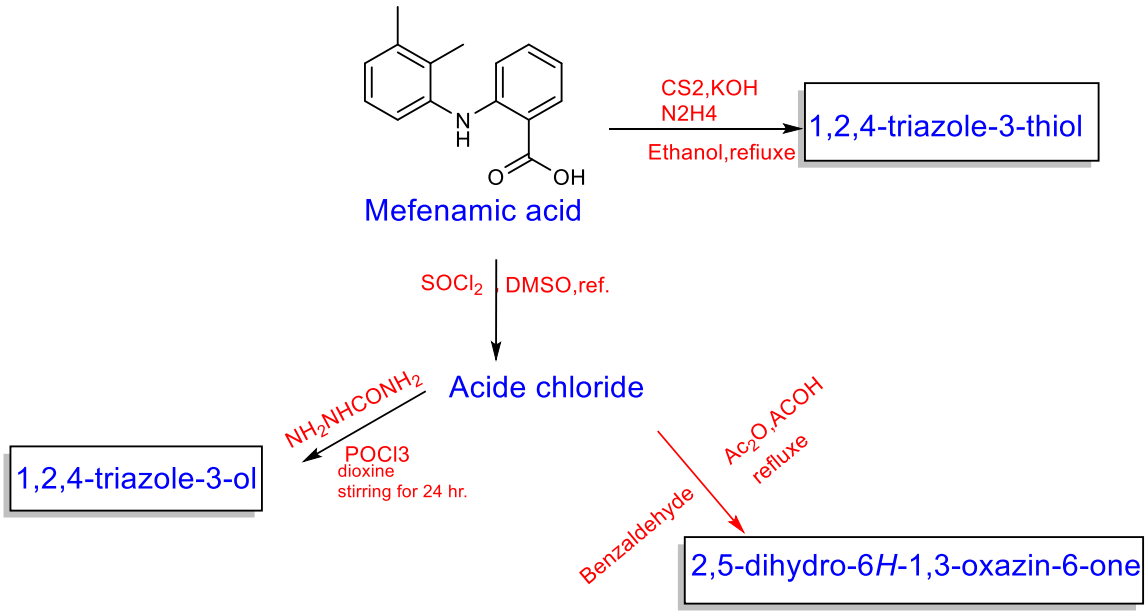

Communications In Catalysis
Vol. 2, No. 1, 2023, pp.21-36
DOI: 10.22049/CIC.2023.28343.1031

Azarbaijan Shahid Madani University

Extraction and identification of active ingredients in *Rhubarb* plant

Ramin Roohparvar[1,*]

[1]Cereal Research Department, Seed and Plant Improvement Institute, Agricultural Research, Education and Extension Organization (AREEO), Karaj, IRAN

Email: r.roohparvar@areeo.ac.ir

Received: 2023-02-22, Accepted: 2023-03-17

Abstract

Rhubarb is a plant from the Polygonaceae family, native to Asia (likely Siberia or the Himalayas). In this study, Rheum plants were dried in a cool and dark place, and then the stem and flower powders were extracted using hexane, chloroform, and methanol solvents at room temperature with a Soxhlet apparatus. Column and plate chromatography were then used for the main separation of the extract components. The hexane, chloroform, and methanol extracts of the Rheum stem were separated into 11, 8, and 7 parts, respectively, using the solvent systems of ethyl acetate/petroleum ether, chloroform/methanol/ethyl acetate, and methanol/ethyl acetate/water/acetic acid. The pure compounds were identified using FT-IR, ^{1}HNMR, and ^{13}CNMR spectroscopy.

Keywords: *Rhubarb* plant, Extraction, Steam evaporation, Spectroscopy investigation

Introduction

Rhubarb is a perennial plant, belonging to the family Polygonaceae and the genus Rheume, which grows in dry and semi-arid mountainous areas, and is usually well adapted to the slopes of the mountains, under the rocks. It grows in spring and early summer and has a common root that grows one to two meters in the ground and is resistant to cold and frost. It has two types of stems; one is an underground stem which is called a rhizome [1, 2]. After growing, the rhizome becomes fleshy and woody, and aerial stems and broad leaves grow from its buds. The second type is aerial stems that grow up to one and a half meters. In the years when the average annual rainfall is at least 130 mm. *Rhubarb* produces flowering stems 50 to 80 centimeters high. At the end of the flowering stem, the yellow, cream-colored flower is well visible in early spring (May). *Rhubarb* is a perennial herb that is widespread in southern and central parts of Asia. According to reports, it was used as a medicinal plant in China before the Christian era. *Rhubarb* grows in Iran in the foothills of the Alborz Mountains, the mountains of Azerbaijan, the Binaloud range north of Tehran, and in the mountainous village of Robat-e-Tork. The plant has 60 species [3-6] and is used to treat a variety of diseases such as liver disease, gastrointestinal bleeding, hepatitis, colds, hemorrhoids, coughs, anxiety, headaches, indigestion, stomach pain, constipation, and has antibacterial, anticancer, and antidiabetic properties [7]. *Rheum Ribes* tolerates very cold temperatures and survives even below 20 degrees Celsius. Leaves turn pink or red at low temperatures and dark green at temperatures above 30°C. *Rhubarb* is more productive in rainy areas and grows better in soft and fertile soils rich in potassium [8, 9]. This plant can be grafted to other species that are compatible with plants from other species. This plant prefers relatively neutral soils. But it can grow in acidic or alkaline soils. It can also tolerate harsh weather conditions and conditions with a lack of light and dry lands [10-12].

Out of 60 species of *Rheum*, 3 species grow in the climatic conditions of Iran, including *Rheum Persium*, *Rheum Ribe*, and *Rheum tarkestanicum* [13, 14]. In the years 1998 and 1995, five stilbene derivatives and six anthraquinone derivatives were extracted from the roots of Rheum. 57 different anthraquinone, stilbene, and flavonoid compounds have been identified from the roots and stems of *Rheum australe*. According to phytochemical studies carried out on *Rheum* ribes in the years 1961, 1973, 1978, 1982, 1988, and 1989, anthraquinone derivatives were discovered, and stilbene derivatives were also confirmed during studies conducted in 1984, 1971, and 1988 [14-17]. The effective compounds identified by HPLC analysis show that the most common components of anthraquinone and stilbene, which are shared by most genera of this plant. Different species of the *Rheum* genus contain polyphenolic compounds such as anthraquinones, anthocyanins, flavanols, stilbenes, and naphthalene. This plant contains vitamins A, B, and C. The content of phenolic and flavonoid compounds in stem and root extracts of Rheum obtained with methanol and chloroform solvents have also been determined.

Experimental

Materials

Methanol, ethanol, chloroform, diethyl ether, dichloromethane, ethyl acetate, hexane, petroleum ether, and chromatography silica gels including TLC Silica gel60 GF254 and column chromatography silica gel 60 (0.063-0.2) from Merck were used.

Charactrization

FT-IR spectra were recorded using a Bruker FT-IR instrument in the range of 400-4000 cm^{-1} with KBr pellets. For centrifugation, a Hettich D-785321 Tuttlingen centrifuge, a JENWAY1000 magnetic stirrer, a Sartorius LA1205 balance, 20 × 20 cm glass plates, and a Heidolph Heizbad Wb solvent evaporator were used. ^{1}HNMR and ^{13}CNMR spectra were recorded using a Bruker SP-100 AVANC (100MHZ) instrument.

Plant preparation and scientific verification

Rhubarb plant (*Rheum Ribes*) was collected from East Azarbaijan province, from the mountains around the city of Tasuj, and its scientific name was scientifically confirmed by members of the faculty of botany at Shahid Madani University. Then the plant was dried in a place away from light and with proper ventilation for 3 weeks. After complete drying, the stems and flowers were separated and packed in glass containers and paper boxes where air could enter and exit.

Methods of extracting the essence from the stem and flower of the plant

The stems and flowers are ground to a powder using a mill. The different parts of the plant should be powdered enough to ensure proper extraction. 15 grams of completely powdered fresh *Rheum Ribes* stems were placed in 280 mL of hexane solvent under the Soxhlet extraction system. After the extraction was complete (when the solvent became colorless on the system's finger), the flask containing the extract was subjected to solvent evaporation using a Heidolph Heizbad. The resulting extract is in hexane form, and in the next steps, chloroform and methanol extracts were prepared using this method of extraction. The extraction process was also carried out for the *Rheum Ribes* flower, and hexane, chloroform, and methanol extracts were obtained from the flower accordingly.

Method of identifying natural compounds present in *Rhubarb* plant

Identification tests for alkaloids, flavonoids, steroids, glycosides, anthraquinones, tannins, terpenoids, and saponins were performed on the species under study [18-20].

Method for separation of compounds in Rheum Ribes plant

In this study, to separate the compounds present in the *Rheum Ribes* plant, hexane, chloroform, and methanol extracts were prepared from the stem and flower of the plant using a *Soxhlet* apparatus. Then, a thin-layer chromatography (TLC) system was selected as a solvent system to separate the components of the extracts. Some of the components of the extracts were separated using column chromatography, and others were separated using plate chromatography under the selected solvent system. In cases where the number of spots observed in the thin-layer chromatography was not suitable, column chromatography was used for

separation. In this process, after the chromatography column was activated with silica gel, the extracts were mixed with some silica gel and slowly transferred to the column. Then, the column was gently washed with a suitable solvent system as the mobile phase. The resulting components were collected and concentrated (the separated components are recorded in the results section of the charts).

Method of purifying the separated extracts of hexane stem (H) and flower (GH), chloroform stem (2C) and flower (GC), methanol stem (M) and flower (GM) of the Rheum Ribes plant

Purification method for H4

H4 is a brownish-purple color and appears as a bright pink under a UV lamp at a wavelength of 366 nm. This component was dissolved in chloroform and then purified using TLC with pure methanol as the solvent.

Purification method for 2C7

2C7 is a cloudy green substance that appears as a bright blue under a UV lamp at a wavelength of 254 nm. It was dissolved in methanol and then further purified using the Nobel recrystallization method with chloroform as the solvent.

Purification method for 2C8

2C8 is a muddy green substance that appears pink under a UV lamp at a wavelength of 366 nm and dissolves in chloroform. The purification process continued by column chromatography using a system of methanol and chloroform, followed by recrystallization with methanol to obtain a white precipitate that dissolves in chloroform. The desired combination was separated by further purification using ethyl acetate and methanol as solvent.

M6 Purification Method

M6 is a golden orange color and appears dark under a UV lamp with a wavelength of 366 nm. It was dissolved in methanol and purified using a chromatography column with a chloroform and ethyl acetate solvent system. Finally, the pure compound was obtained by crystallization with chloroform.

GH9 Purification Method

GH9 is green and appears pink under a UV lamp with a wavelength of 366 nm. Methanol was added dropwise to the chloroform solution of GH9, resulting in white precipitates. The purification process was continued, leading to the pure compound.

GH10 Purification Method

GH10 is yellow and appears pink under a UV lamp with a wavelength of 366 nm. It was dissolved in hexane or chloroform and purified using a chromatography column with a dichloromethane and chloroform solvent system. Then, a mixture of methanol and water was added to the hexane solution of GH10, resulting in a two-phase mixture that was separated using a separatory funnel. Finally, the organic phase was concentrated using a pranayl solvent, resulting in white precipitates.

Result and discussion

Using the Soxhlet extraction method, higher amounts of hexane, chloroform, and methanol extracts were obtained from the

flower of *Rheum Ribes* compared to the stem extracts. The results are presented in Table 1.

Table 1. Amounts of hexane, chloroform, and methanol extracts from stem and flower *Rhubarb*

Name of extract (g)	**Amount of extract from stem (g)**	**Amount of extract from flower (g)**	**Initial powder weight (g)**
Hexane	0.26	0.67	15
chloroform	0.507	1.7	15
methanol	2.161	3.91	15

The thin-layer chromatography technique was also used to separate each extract into various solvent systems. In extracts made with hexane and chloroform, there were more separated components. In Figures 1 and 2, the separation images are displayed.

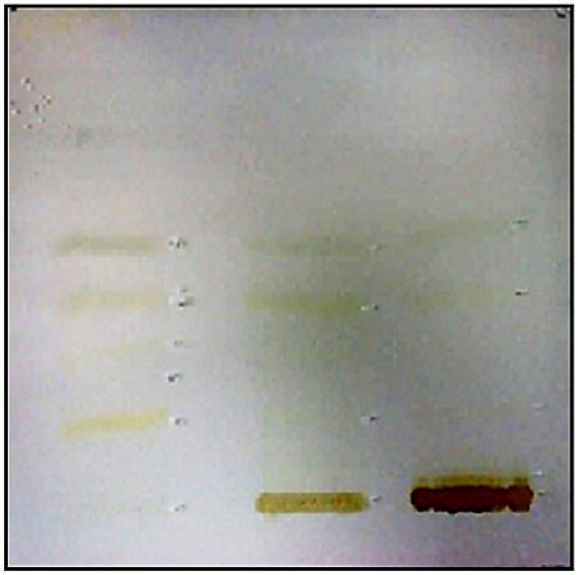

Figure 1. Separation of hexane, chloroform, and methanol extracts from flower (from left to right)

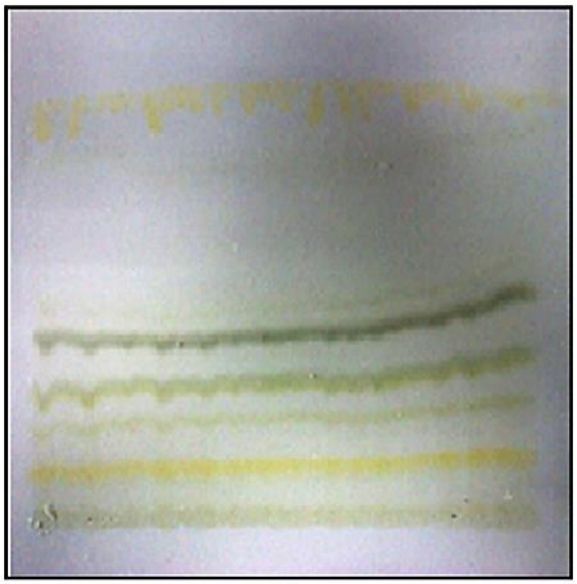

Figure 2. Separation of hexane extracts from stem

Identification tests were carried out to determine the kinds of natural compounds that were present in the stem and flower extracts of Rheum Ribes. Table 2 displays the outcomes of these tests. Solvents are required in addition to the column chromatography technique to dissolve the extracted materials on silica gel plates (in the TLC method). Table 3 includes a list of these solvents.

Table 2. Results of identification tests for natural compounds present in the *Rheum* plant

Flower	**Stem**	**Type of identification tests**
Observed	Observed	Tannin
Observed	Observed	Terpenoid
Observed	Observed	Anthraquinone
Observed	Observed	Saponin
Absent	Absent	Alkaloid
Observed	Observed	Flavonoid
Observed	Observed	Glycoside

Table 3. Required solvents for washing silica gel plates components

Used Extracted Components	Solvent	Used Extracted Components	Solvent	Used Extracted Components	Solvent	Used Extracted Components	Solvent
H1	Acetone and ethanol	2C1	ethanol and methanol	M4	Chloroform and ethanol and methanol	GH6	Chloroform
H2	Acetone and chloroform	2C2	Chloroform and methanol	M5	methanol/ ethanol (1:1)	GH7	Chloroform
H3	Acetone and chloroform	2C3	methanol	M6	methanol/ ethanol (1:1)	GH8	Chloroform
H4	chloroform	2C4	methanol	M7	Acetone and chloroform	GH9	Chloroform
H5	Acetone and chloroform	2C5	Acetone and chloroform	M8	Acetone and chloroform	GH10	Hexane
H6	chloroform	2C6	methanol	GH1	Acetone and chloroform	GC1	Ethyl acetate and chloroform,
H7	Acetone and chloroform	2C7	chloroform	GH2	Acetone and chloroform	GC2	Acetone and chloroform
H8	chloroform	M1	methanol/ ethanol (1:1)	GH3	chloroform	GC3	Acetone and chloroform
H9	chloroform	M2	methanol/ ethanol (1:1)	GH4	chloroform	GC4	Chloroform
H10	Hexane and chloroform	M3	methanol/ ethanol (1:1)	GH4	chloroform	GC5	Chloroform
H11	and chloroform	GM2	distilled water and methanol	GM4	Chloroform and ethanol and methanol	GC6	Chloroform
GM1	ethanol and methanol	GM3	Chloroform and ethanol and methanol	GM5	Chloroform and ethanol and methanol	GM6	Chloroform

Table 4. Components separated from the plate

Components	R_F	Components	R_F	Components	R_F
H1	0.055	M1	0.055	2C1	0.055
H2	0.083	M2	0.088	2C2	0.1
H3	0.11	M3	0.127	2C3	0.16
H4	0.16	M4	0.33	2C4	0.28
H5	0.22	M5	0.41	2C5	0.41
H6	0.24	M6	0.55	2C6	0.63
H7	0.2	M7	0.66	2C7	0.79
H8	0.32	M8	0.67	GC1	0.055
H9	0.33	GM1	0.055	GC2	0.072
H10	0.5	GM2	0.083	GC3	0.15
H11	0.8	GM3	0.16	GC4	0.36
GH6	0.37	GM4	0.33	GC5	0.44
GH7	0.47	GM5	0.47	GH1	0.055
GH8	0.58	GM6	0.5	GH2	0.11
GH9	0.69	GM7	0.055	GH3	0.22
GH10	0.80	GH5	0.3	GH4	0.27

The RF distances of the separated components of the hexane, chloroform, and methanol stem and flower extracts are given in Table 4.

FT-IR and ^{1}HNMR spectra of compound 2C7

A broad and strong absorption at 3418 cm^{-1} is related to the stretching vibrations of the acidic OH group, and the absorption at 1650 cm^{-1} is related to the carbonyl group of the acidic group. The absorption bands at 12953-2843 cm^{-1} are related to the stretching vibrations of the aliphatic side chain C-H, and the absorption band at 1660 cm^{-1} is related to the C=C group of the aromatic ring. The absorption band at 1113 cm^{-1} is related to C-O. In the ^{1}HNMR spectrum, the peaks at 10 ppm are related to the phenolic OH group, the peak at 11 ppm is related to the acidic OH group, and the peaks at 7.047-7.068 ppm are related to H1 in the ortho position of the acidic and phenolic groups on the aromatic ring. The peaks at 7.55-7.622 ppm are related to H2 and H3 on the aromatic ring. Based on the analysis, the aromatic nature of a part of the compound is confirmed. However, due to the complexity of the peaks in the aliphatic region, identification of this part of the molecule was not possible, and no structure was proposed for it (Figures 1 and 2).

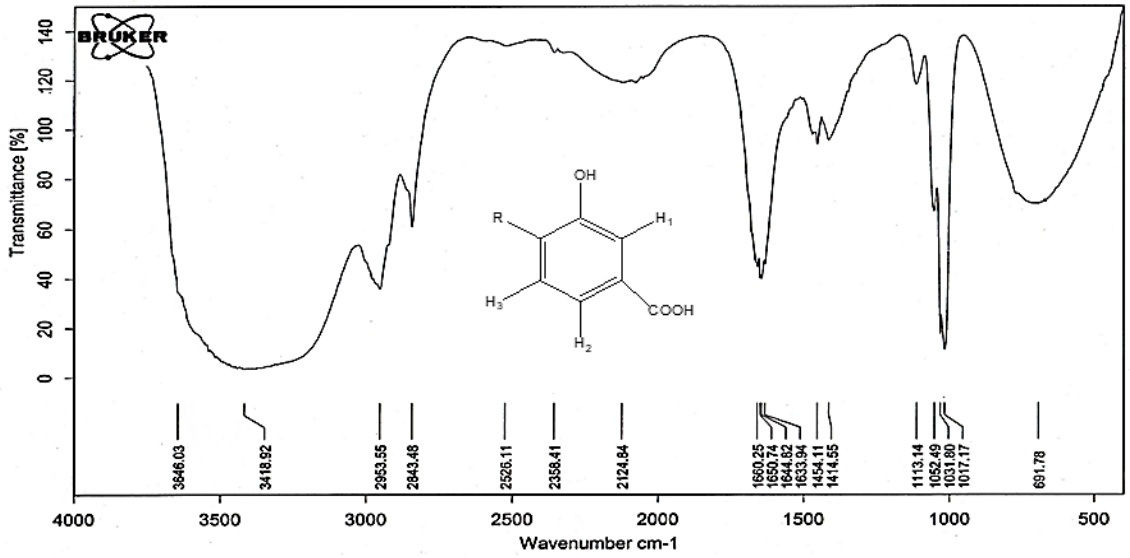

Figure 1. FT-IR spectrum of compound 2C7

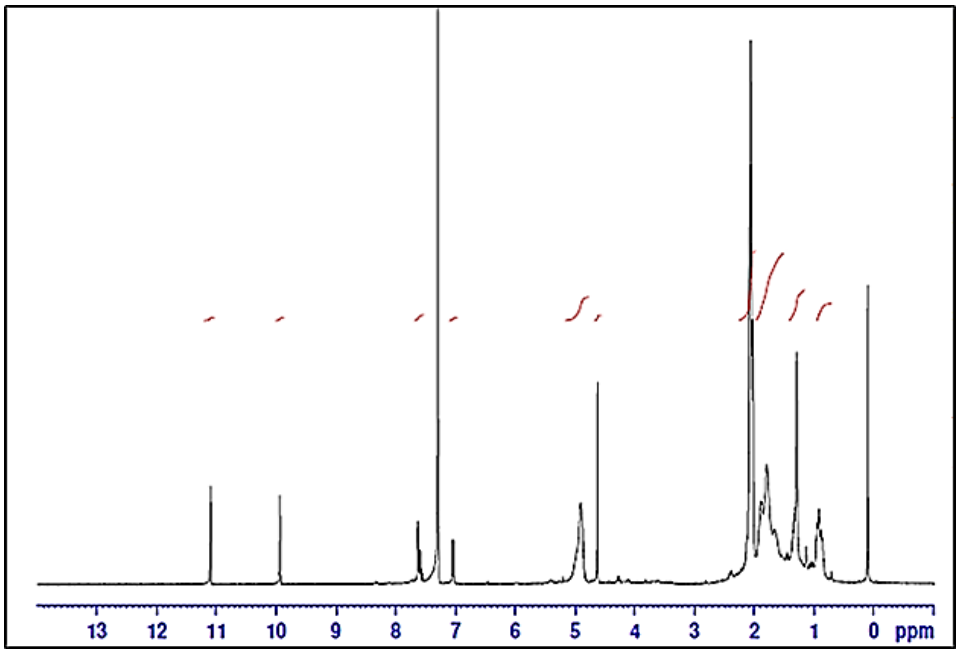

Figure 2. ^{1}HNMR spectrum of compound 2C7

FT-IR and ^{1}HNMR spectra of compound GH9

Strong absorptions in the range of 2920-2849 cm^{-1} are related to the stretching vibrations of aliphatic C-H, and the absorption at 1463 cm^{-1} is related to the vinyl C=C group. The absorptions at 1261 and 1096 cm^{-1} are related to C-O. In the ^{1}HNMR spectrum, the peaks at 4.714-4.616 ppm are related to H1 and H3, and the peak at 5.374 ppm is related to the CH_2 group. Again, due to the complexity of the side group structure, identification was not possible (Figures 3 and 4).

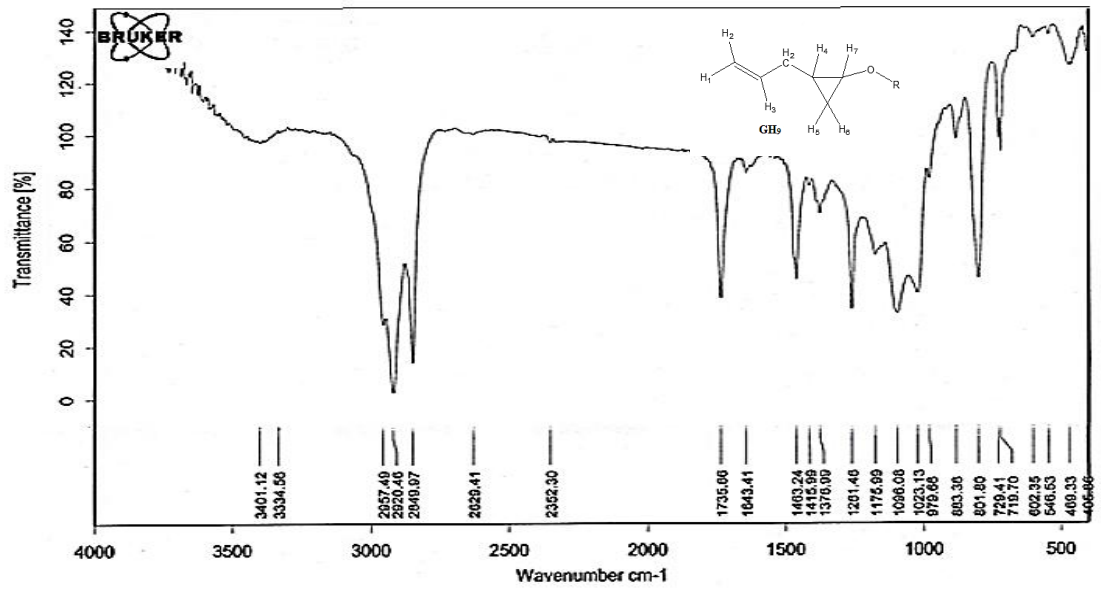

Figure 3. FT-IR spectrum of compound GH9

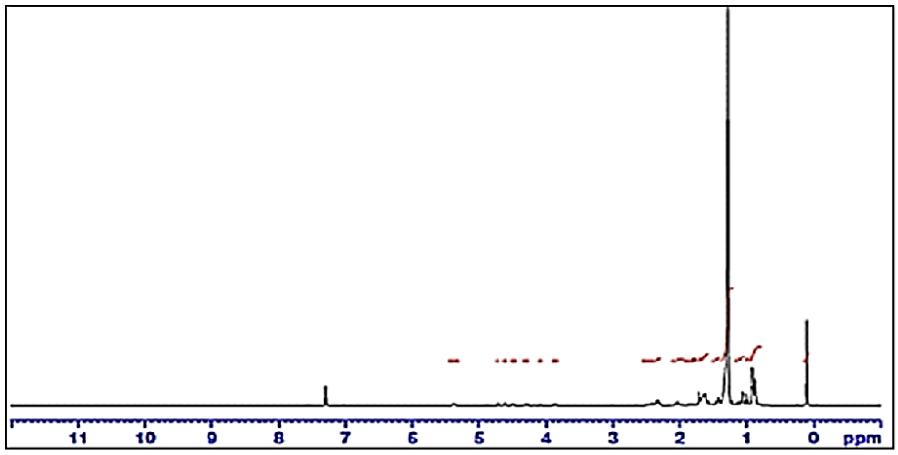

Figure 4. [1]HNMR spectrum of compound GH9

FT-IR and H1NMR spectra of GH10 compound

The absorption bands at 1460 cm^{-1} and 1265 cm^{-1} are related to the aliphatic C-H and C-O stretching vibrations, respectively. In the [1]HNMR spectrum, the peaks at 5.73-5.879 ppm are related to H5, the peak at 5.373 ppm is related to H4, and the peak at 2.917 ppm is related to H9. Due to the complexity of the side structure, no proposed structure was presented (Figures 5 and 6).

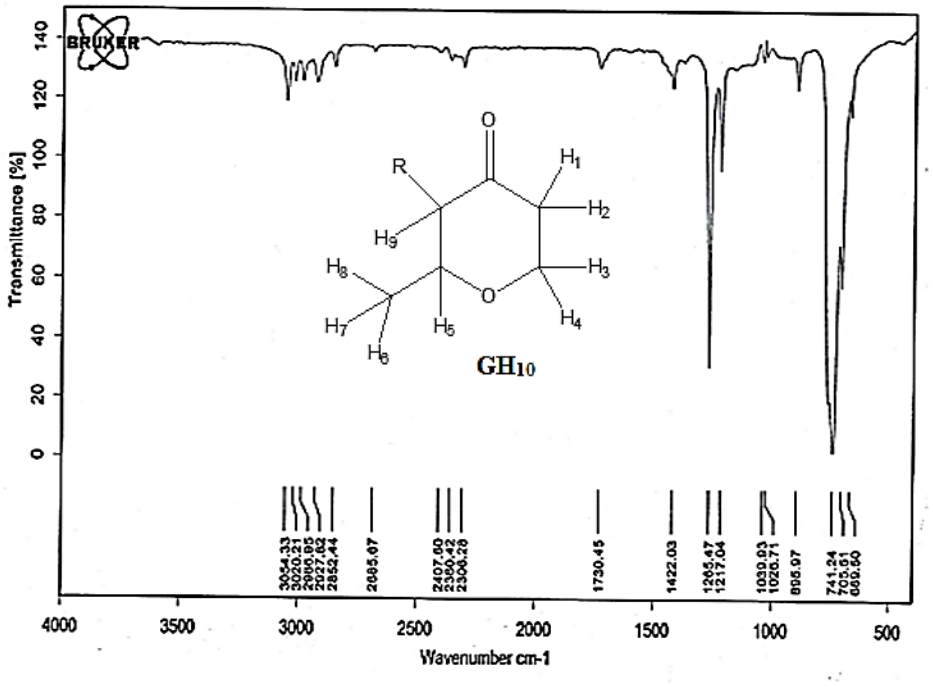

Figure 5. FT-IR spectrum of compound GH10

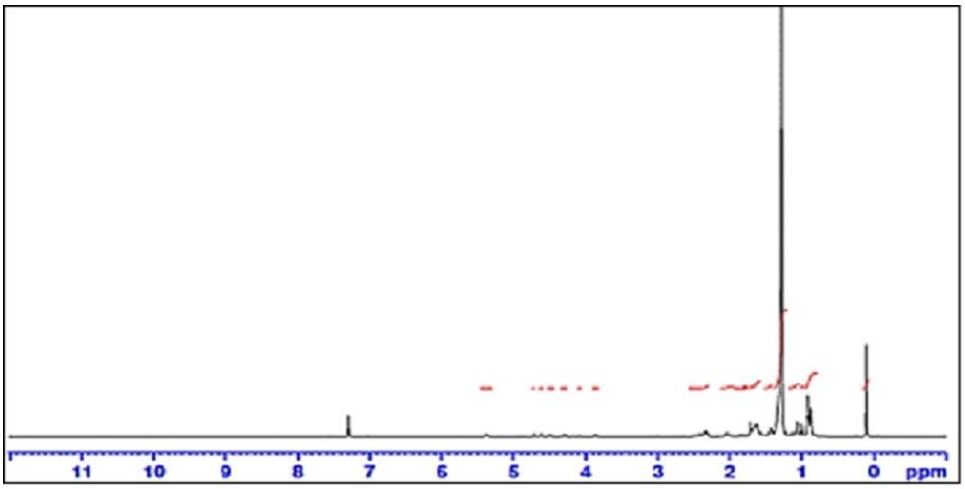

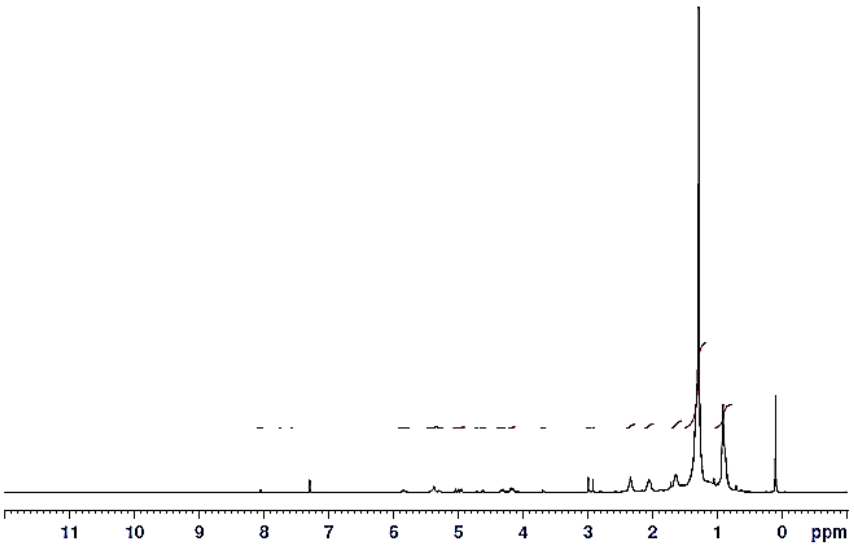

Figure 6. [1]HNMR spectrum of compound GH10

FT-IR and [1]HNMR spectra of M6 compound

The broad and strong absorption band at 3460 cm^{-1} is related to the stretching vibrations of the acid group OH, the absorption bands at 2843 cm^{-1} and 1644 cm^{-1} are related to the aliphatic C-H stretching and the C=C stretching of the aromatic group, respectively. The absorption band at 1016 cm^{-1} is attributed to the C-O stretching vibration. In the [1]HNMR spectrum, the peaks at 7.157-7.117 ppm are related to H2, and the peaks at 6.815-6.757 ppm are related to H5. Due to the complexity of the side structure, no proposed structure was presented (Figures 7 and 8).

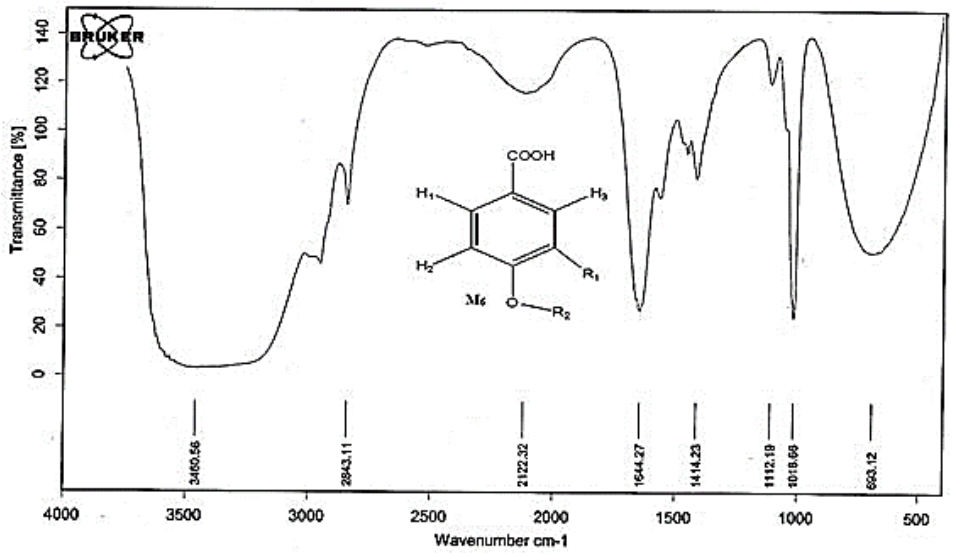

Figure 7. FT-IR spectrum of compound M6

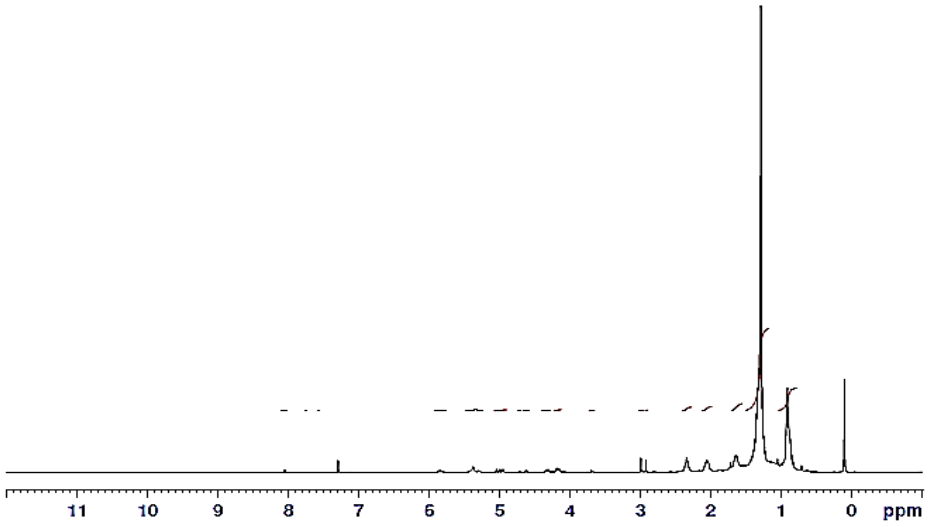

Figure 8. [1]HNMR spectrum of compound M6

FT-IR and [1]HNMR spectra of compound H4

FT-IR of H4 reveals absorptions in the region of 2881-2966 cm^{-1} corresponding to aliphatic C-H stretching vibrations, and an absorption at 1730 cm^{-1} corresponding to the carbonyl group of a ketone. In the [1]HNMR spectrum, peaks at 2.072 and 2.052 ppm are attributed to hydrogens of group a, while peaks in the region of 1.288-1.360 ppm are attributed to hydrogens of group b. Peaks at 0.907 and 0.876 ppm are attributed to H3, while peaks at 1.665 and 1.883 ppm are attributed to H4 and H5, respectively (Figures 9 and 10).

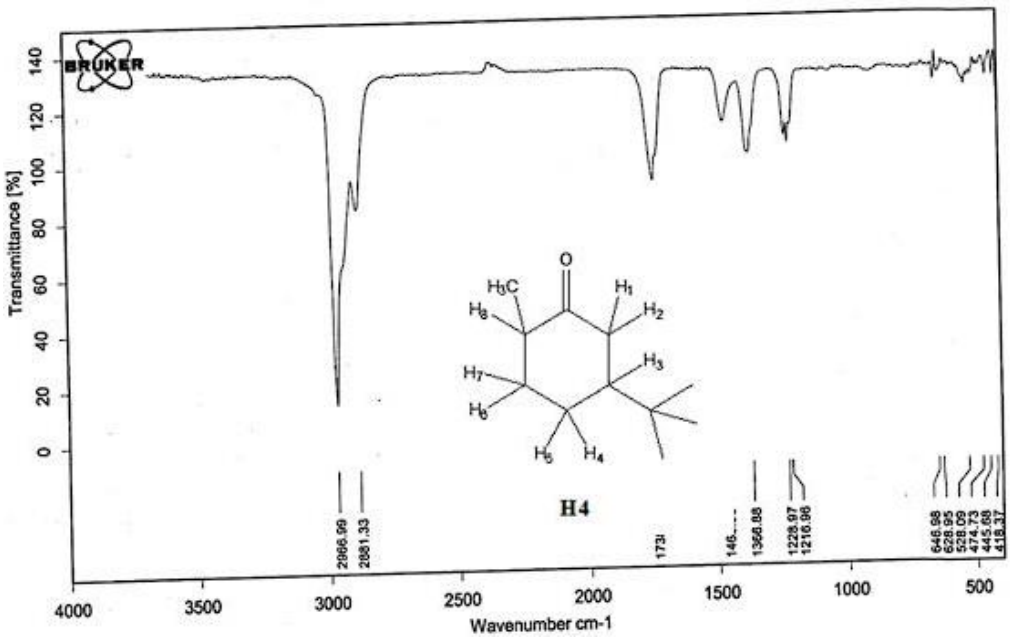

Figure 9. FT-IR Spectrum of compound H4

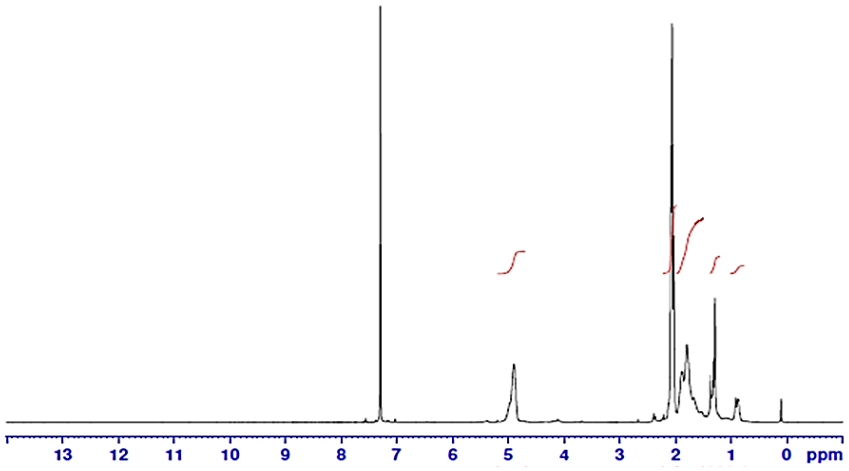

Figure 10. [1]HNMR Spectrum of compound H4

FT-IR and [1]HNMR spectra of compound 2C8

FT-IR of 2C8 reveals a sharp absorption in the region of 3083-3000 cm^{-1}, corresponding to the stretching vibrations of C-H bonds in the aromatic ring. The presence of a peak at 1622 cm^{-1} is attributed to the carbonyl group in the aromatic rings, while the peak at 1583 cm^{-1} corresponds to the C=C bond in the aromatic rings, and the peak at 1100 cm^{-1} is related to the C-O bond. In the [1]HNMR spectrum, the peaks in the region of 7.028-7.222 ppm are related to H1, H2, H3, and H4, while the peaks in the region of 6.602-6.484 ppm are related to H5-H6, and the peaks in the region of 5.408-5.332 ppm are related to H8. Due to the complexity of the R1 and R2 structures, a definite structure cannot be proposed for the compound (Figures 11 and 12).

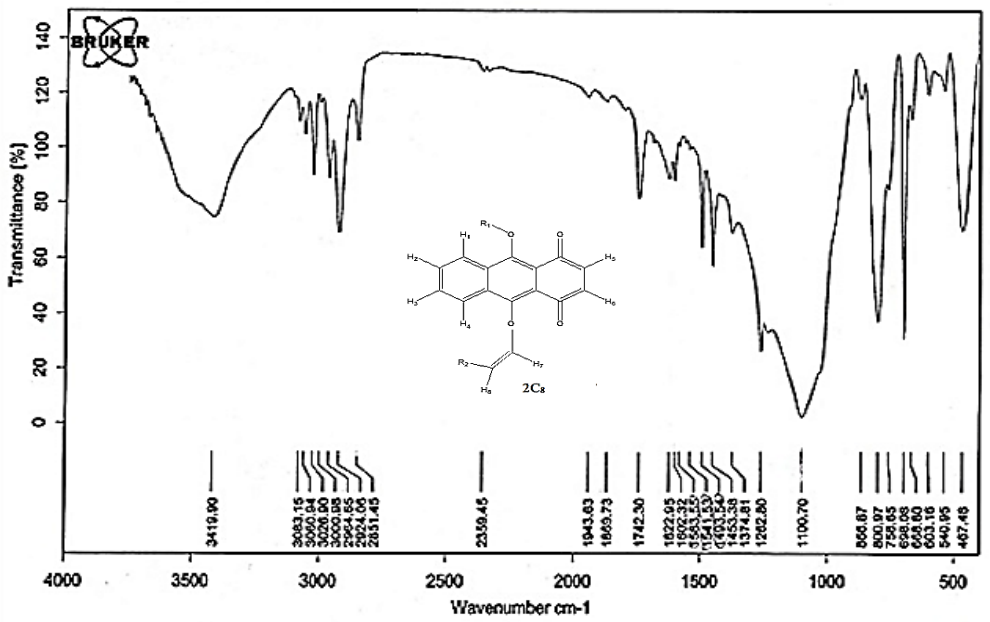

Figure 11. FT-IR Spectrum of compound 2C8

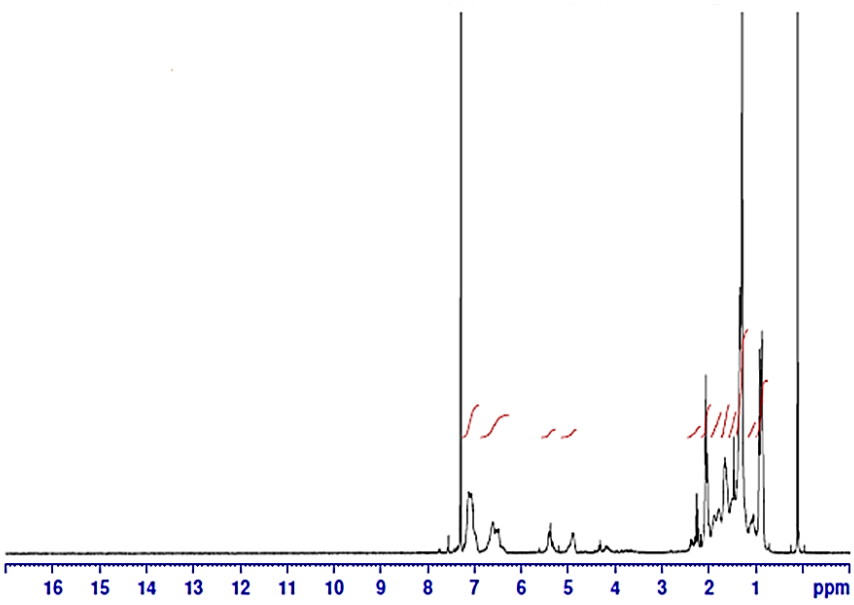

Figure 12. [1]HNMR Spectrum of compound 2C8

Based on the results shown in Table 1, the amount of extract obtained from 15 g of the flower and stem of the *Rhubarb* plant is higher in the methanol, chloroform, and hexane extracts of the flower. According to the identification tests performed on the *Rhubarb* plant (Table 2), it contains tannins, terpenoids, anthraquinones, saponins, alkaloids, flavonoids, and glycosides. According to the results shown in Table 3, different solvents and single solvents can dissolve the components present in silica gel, and several compounds were purified using various methods such as crystallization, column chromatography, and thin-layer chromatography. Among these compounds, the ones with higher amounts were selected and identified using various methods, although some of the natural compound structures are too complex to be fully identified. This research on the *Rhubarb* plant's flower is innovative, and its purification method is cost-effective.

Conclusion

Using the Soxhlet extraction method, the amounts of hexane, chloroform, and methanol extracts of rhubarb flower were higher compared to the stem extracts. In order to identify the types of natural compounds present in the extracts of rhubarb plant stems and flowers, identification tests were performed. The results of these tests are shown in Table 2. Apart from the cases where the chromatography column is used for separation, to separate the extractable materials from the silica gel plate (in the plating method), solvents are needed to dissolve the desired extractable materials in itself, the natural extractable compounds include the following compounds: Tannins, terpenes, anthraquinones, alkaloids, flavonoids and glycosides.

References

[1] Zghonda N, Yoshida S, Ezaki S, Otake Y, Murakami C, Mliki A, Bioscience,

biotechnology, and biochemistry, 2012, 954-60
[2] Sitasawad SL, Shewade Y, Bhonde R. Journal of Ethnopharmacology, 2000, 71-9
[3] Aziz A, Khaliq T, Khan JA, Jamil A, Majeed W, Faisal MN, Pakistan Journal of Agricultural Sciences, 2017
[4] Ahmed SR, Rabbee MF, Roy A, Chowdhury R, Banik A, Kubra K, Plants, 2021, 1348
[5] Nirmala C, Shahar B, Dolma N, Santosh O. Applied Food Research, 2019
[6] Cai Y, Sun M, Xing J, Corke H. Journal of agricultural and food chemistry, 2004, 7884-90.
[7] Stanaway JD, Afshin A, Gakidou E, Lim SS, Abate D, Abate KH, 2018, 1923-94.
[8] Öztürk M, Aydoğmuş-Öztürk F, Duru ME, Topçu G. Food chemistry, 2007, 623-30.
[9] Ahmad A, Patel I. J Pharm Bioallied Sci, 2013, 326.
[10] Haggag E, Mahmoud I, Abou-Moustafa E, Mabry T. Asian Journal of Chemistry, 1999, 707-14.
[11] El-Hilaly J, Tahraoui A, Israili ZH, Lyoussi B. Pak J Pharm Sci. 2007, 261-8.
[12] Alenzi F, El-Bolkiny YE-S, Salem M. British journal of biomedical science, 2010, 20-8.
[13] Sousa PL, Quinet Y, Ponte EL, do Vale JF, Torres AFC, Pereira MG, Journal of Ethnopharmacology, 2012, 213-6.
[14] Agarwal S, Singh SS, Verma S, Kumar S. Journal of ethnopharmacology, 2000, 43-6.
[15] AKHTAR MS, QAYYUM MI, IRSHAD N, HUSSAIN R, HUSSAIN A, Yaseen M, Int J Curr Pharm Res, 2013, 36-7.
[16] Zargar BA, Masoodi MH, Ahmed B, Ganie SA. Food Chemistry, 2011, 585-9.
[17] He Z-H, He M-F, Ma S-C, But PP-H. Journal of ethnopharmacology, 2009, 313-7.
[18] Uddin G, Rauf A, Siddiqui BS, Shah SQ. Middle-East Journal of Scientific Research, 2011, 78-81.
[19] Patel V, Patel R. Journal of Chemical and Pharmaceutical Research, 2016, 1423-43.
[20] Aburjai TA. Phytochemistry, 2000, 407-10.

Communications In Catalysis
Vol. 2, No. 1, 2023, pp.37-49
DOI: 10.22049/CIC.2023.28599.1033
Azarbaijan Shahid Madani University

Investigation of Menthol and Caprylic acid based Deep Eutectic Solvent from the Point of View of Molecular Dynamics Simulation and COSMO-RS

Samaneh Barani Pour [1], Nasrin Jabbarvand Behrooz [2], Jaber Jahanbin Sardroodi [3,*], Alireza Rastkar Ebrahimzadeh [4], Mohammad Sadegh Avestan [5]

[1,2,3,4]Molecular Science and Engineering Research Group (MSERG), Molecular Simulation Lab, Azarbaijan Shahid Madani University, Tabriz, Iran

[5]Department of Chemistry, University of Cincinnati, Cincinnati, OH 45221, United States

E-mail: jsardroodi@azaruniv.ac.ir

Received: 2023-04-25, Accepted: 2023-05-04

Abstract

The widespread use of toxic and volatile organic solvents has led to a new challenge in the industry. In this regard, the design of green and biodegradable solvents such as deep eutectic solvents (DESs) has attracted a lot of attention. Molecular-level description of the interactions between HBA and HBA can provide a valuable perspective for the design of these green solvents. In order to, COSMO-RS was used for screening potential DESs qualitatively. Then, we herein performed molecular dynamics (MD) simulations on DES based on Caprylic acid (CAP) and menthol (MEN) which is very widely used in the process of separating pollutants and biomolecules from the water environment and it was observed that the hydroxyl group of menthol plays a key role in the formation of deep eutectic solvents based on MEN and CAP.

Keywords: DESs, MD, Spatial distribution function, Mean-Square Displacement, Caprylic acid, Menthol

Introduction

With the increasing expansion of the separation process using toxic and volatile organic solvents that produce a major part of dangerous air-polluting gases, green technology is seriously seeking to find suitable alternatives for these solvents in order to preserve the environment and reduce possible negative effects on human health. In this regard, ionic liquids (ILs) were used to replace these solvents [1]. Among the problems that exist in the use of ionic liquids is the high price of these compounds, so to overcome the high cost, new compounds called deep eutectic solvents (DESs), which have properties similar to ionic liquids, have recently attracted the attention of researchers [2].

Deep eutectic solvents are binary mixtures where the lack of charge stabilization through hydrogen bonding between the two hydrogen bond donor and acceptor components has led to a decrease in the melting point of this mixture compared to the pure components [3]. The most common DESs are based on choline chloride as a hydrogen bond acceptor, and carboxylic acids, citric acid, sugars, and other hydrogen bond donors such as urea and glycerol. DESs are very cheap, biodegradable, and non-toxic, which can be widely used in pharmaceutical and extraction industries.

A quick look at the DESs presented in the literature shows that the majority of these solvents are very hydrophilic. Recently, the chemical instability of hydrophilic solvents based on ammonium salts when in contact with water has motivated the design of hydrophobic DESs as green alternatives for organic solvents have doubled [4]. Hydrophobic DESs based on menthol and fatty acids are widely used in extracting biomolecules and pollutants from aqueous environments [5]. In this work the dynamical and structural properties of a DES composed of menthol and Caprylic acid were investigated through MD simulations at 298.15 K and the capability of menthol and Caprylic acid components in forming an acceptable DES was analyzed. Dynamical parameters such as mean square displacement (MSD), are calculated at the pressure of atmosphere. Structural parameters such as hydrogen bonds (H-bonds), radial and spatial distribution functions (RDF and SDF) were investigated. Also, for additional investigations of local polarization charge-density, sigma-profile determination analysis was performed in

COSMO-RS.

Methodology

The methods of preparation and simulation of the binary mixture were as follows: first, the molecules (HBA and HBD) were designed using the Visual Molecular Dynamics (VMD) program [6]. The screening charge density distribution on the surface of HBA and HBD (σ-profile) was calculated using the COSMO-RS methodology. The COnductor-like Screening MOdel for Real Solvents (COSMO-RS) model is a thermodynamic model based on quantum chemistry and statistical thermodynamics that is useful for the preliminary design of DESs [7].

Then, the simulation box containing menthol ($C_{10}H_{20}O$) and Caprylic acid ($C_8H_{16}O_2$) molecules at a (1:1) molar ratio were prepared using PACKMOL software [8]. A periodic boundary condition was employed for the MD simulation. The valet algorithm is used with an integration time step of 1 for solving Newton's equations of motion. The MD simulations were performed for 50000 steps in NPT ensembles using the NAMD_2.13 package [9] at 298.15 K. Langevin thermostat [10] and Nose-Hoover thermostat [11] have been used to setting temperature and pressure, respectively. To investigate Long-range electrostatics, the particle mesh Ewald (PME) method with a 12 Å cutoff was considered.

To evaluate the equilibrium of the binary mixture, the root-mean-square deviation (RMSD) of species with respect to a reference structure was obtained, as defined in Equation 1.

$$RMSD = \sqrt{\frac{1}{n}\sum_{i=1}^{n}(x_i - x_{i0})^2 + (y_i + y_{i0})^2(z_i + z_{i0})^2}$$

The results of Figure 1 show that the RMSD path increased at the beginning of the simulation, and then upon reaching convergence, the RMSD value for menthol and caprylic acid molecules reached constant values of 20.0 and 21.0, respectively (see Figure 1).

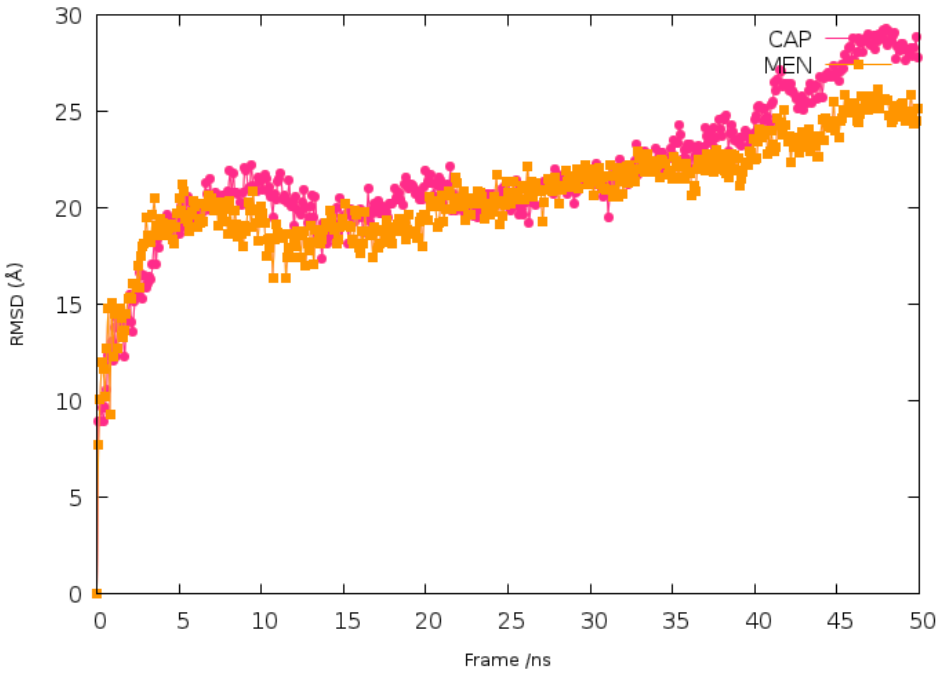

Figure. 1. Root mean square deviation (RMSD) analysis: RMSD of menthol and caprylic acid up to 50 ns.

Results and discussion

To understand and identify the effective interactions in the formation of DES based on menthol and Caprylic acid, the structural properties of the binary mixture were investigated for the last 20 ns of the MD simulations.

RDF and Combined Distribution Functions

The radial distribution function is a useful quantity that represents the probability of finding a molecule at a distance r from another tagged molecule [12]. The radial distribution function is given by Equation (2),

$$g(r) = \frac{1}{\rho N} \langle \sum_{ij} \delta(r - r_{ij}) \rangle \quad (2)$$

, which N and ρ are the numbers of particles and number density, respectively.

To explore in detail the structural properties of the binary mixture, the strategy of site-site RDFs was used. The atomic sites of CAP (C, H, and O atoms) were selected and how to place them around the hydroxyl group of menthol (O1) was investigated in the binary mixture.

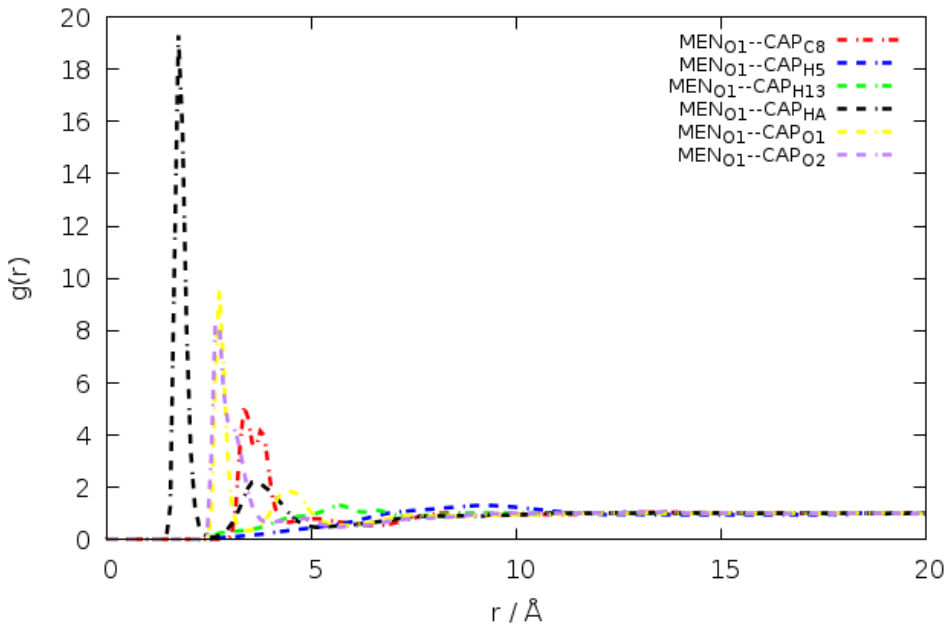

Figure 2. RDFs between different atoms of menthol and Caprylic acid molecules in the binary mixture at 323 K.

The first maximum of peaks for the RDFs between the different atoms of HBD and the O atom of MEN located near 2 Å for the CA-HA···MEN.O pair, 3 Å for the CAP.O1(O2)···MEN.O pairs, 4 Å for the CAP-C8··· MEN.O pair. The sharp RDF peak indicates the H-bond interaction between the carboxyl group (C (=O) OH) of acid and menthol molecules. In Figure 3, the RDFs for the menthol --menthol, HBA -- HBD pairs of the eutectic mixture at 298.15 K are shown. In addition, the first maximum of peak for $g(r)_{CAP-MEN}$ appears at closer intervals compared to the $g(r)_{MEN-MEN}$. It is likely that the hydrogen bonding interaction between HBA and HBD is significant in the mixture.

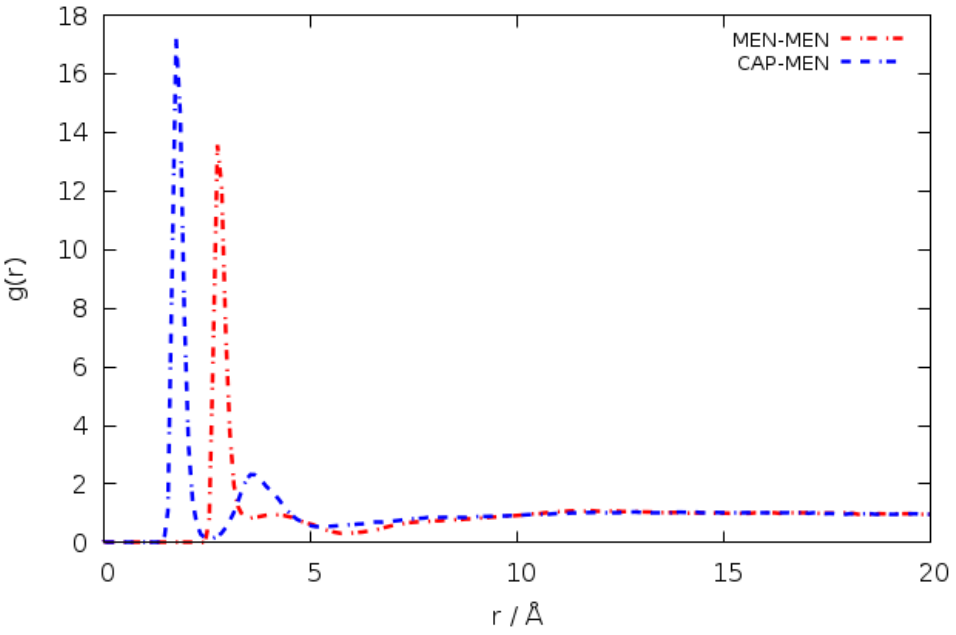

Figure. 3. RDFs between molecules in the binary mixture at 298.15 K.

Hydrogen-Bond Analysis

Hydrogen bonding between HBA and HBD led to a decrease in the melting point of the eutectic mixture compared to the two separated components [13]. H-band distance and angle criteria were considered as follows: the A–H distance ~ 3.5 Å and the D–H–A angle ~150 degrees. The average H-bond between species can be evaluated as follows (well-known Gaussian distribution):

$$F(X) = \frac{a}{\sigma\sqrt{2\pi}} exp^{\frac{-(X-\bar{X})^2}{2\sigma^2}} \qquad (3)$$

$\bar{X}$ and σ are the average numbers of H-bond and standard deviation, respectively.

Observations show that the average H-bond between species was found to be in the order of CAP−MEN (0.18) > MEN−CAP (0.14). The hydrogen bonding results show a strong interaction between the HBA and HBD compared to the interaction between menthol molecules.

Occupancy analysis was performed to investigate the ratio of the number of hydrogen bonds between the possible HBD and HBA pairs [14]. The occupancy ratio of the CAP-MEN hydrogen bond was 99% in the mixture, whereas that of the MEN---MEN interaction was only 85%. It seems that the stability of the hydrogen bond between HBA and HBD is significant compared to hydrogen

bonding between menthol molecules (Figure 5).

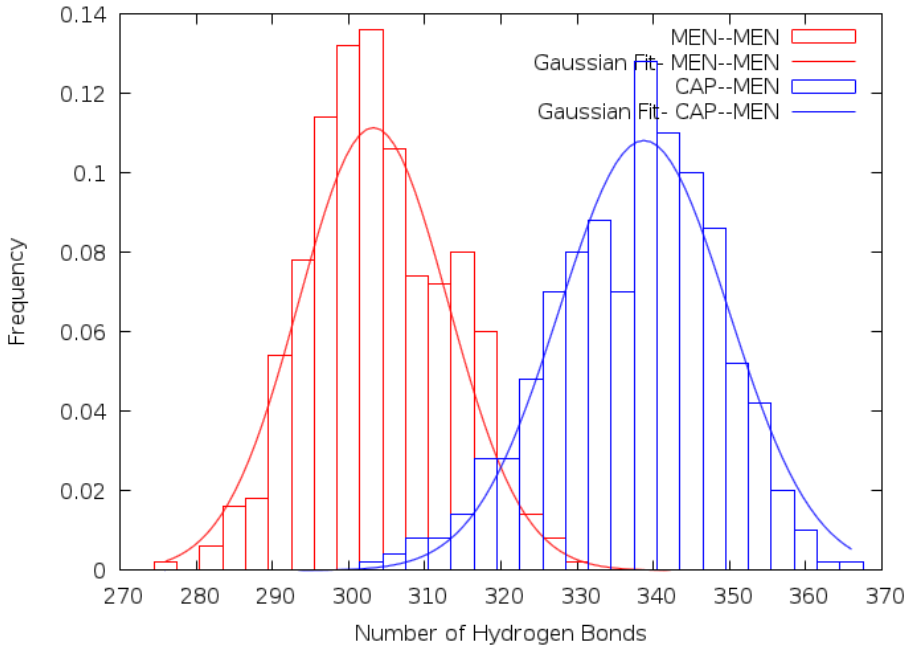

Figure. 4. The distribution of the H-bond number between MEN and CAP (and menthol molecules) in the binary mixtures at 298.15 K.

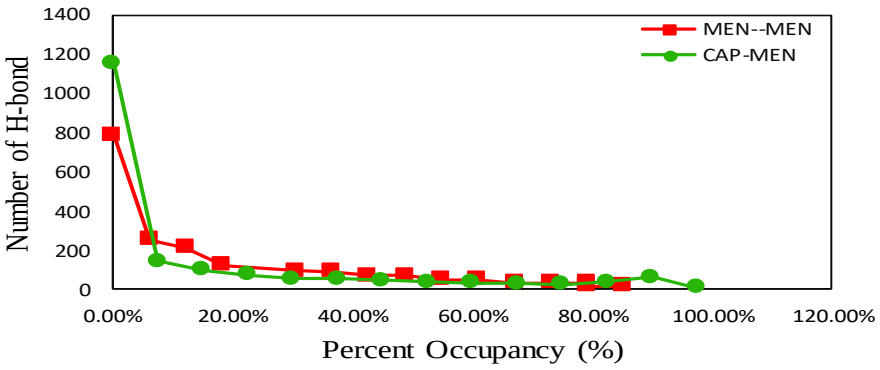

Figure 5. Hydrogen bond percent occupancies for MEN and CAP (MEN molecules) in the binary mixture at 310 K.

Spatial distribution function (SDF)

To get a clearer picture of the 3D-arrangement and placement of the OH group of menthol around Caprylic acid and the acidic functional group of Caprylic acid around menthol, spatial distribution function (SDF) analysis for studying effective sites in intermolecular hydrogen-bond interactions [15] was evaluated with Travis package [16]. As can be seen from Figure 6 (a and b), Caprylic acid is surrounded by the OH group of menthol with a condensed cup from the side of the acidic functional group, which indicates the presence of strong hydrogen bonds between the hydrogen and oxygen atoms of both components, and it can be said that the largest dense cap is related to menthol oxygen around Caprylic acid hydrogen atom, which confirms the narrow and sharp peak of menthol oxygen and Caprylic acid hydrogen at that distance in RDF.

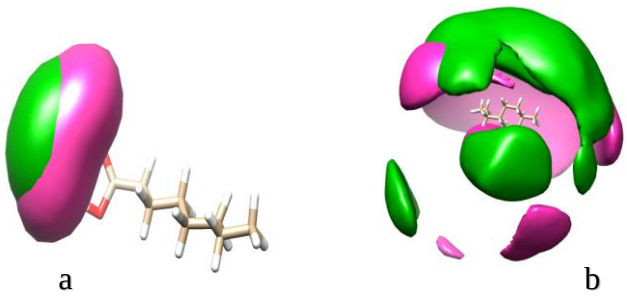

Figure 6. The SDF of (a) O--H of menthol (pink--green cap), around the Caprylic acid, and (b) the acidic functional group of Caprylic acid; HA (pink cap) around menthol.

Mean-Square Displacement (MSD)

Because the transfer of molecules plays a vital role in determining the thermodynamic properties of solvents [17], for this purpose, the microscopic dynamics of the eutectic solvent under our study was investigated by the relation of the MSD and the relationship related to this quantity are as follows:

$$MSD = \langle |r_i(t) - r_i(0)|^2 \rangle = \frac{1}{N} \langle \sum_{i=1}^{N} \left| r_i^{COM}(t) - r_i^{COM}(0) \right|^2 \rangle \quad (4)$$

, which r_i (t) and r_i (0) are the positions of the i-th particle at time t and 0, respectively [18]. The MSDs of the center of mass of menthol and Caprylic acid species in the considered system are evaluated, as illustrated in Figure 7.

The MSD of menthol and Caprylic acid is compared as a function of time in Figure 7 and as it can be seen from the image, the lower slope of the MSD curve of the center of mass of menthol despite the low molecular mass of Caprylic acid can be attributed to lower mobility, and subsequently, the presence of the ring and the effective role of the OH group in establishing strong hydrogen bonds.

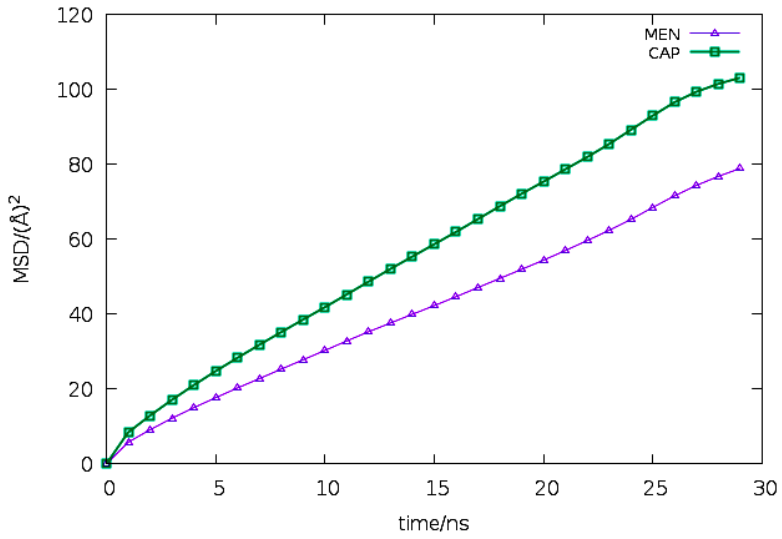

Figure 7. Comparison of the MSD of the center of mass of menthol and Caprylic acid species in the investigated DES.

COSMO-RS- Sigma profiles

In order to quantitatively describe the surface of the molecule and considering that the surface interaction energies depend only on the local polarization charge-densities (the net composition of the surface of each component

in the surface interactions of the local pair-wise) [19]. For this purpose, the sigma profiles of the components of the DES were evaluated and their diagrams are drawn in Figure 8. The COSMO-RS calculations were carried out using the Turbomole software package (TmoleX version 4.2) [20].

The σ profile of Caprylic acid and menthol showed two small peaks in the HBD region (σ < -0.01e/Å^2) around -0.013, -0.018 e/Å^2, respectively, the first peak due to a slightly higher peak of menthol and the second peak due to the higher peak of Caprylic acid, related to the hydrogen exposure of the OH group of menthol and the acidic functional group of Caprylic acid.

In the HBA region (σ > 0.01 e/Å^2) of the σ profiles, the peak of Caprylic acid at about 0.012 e/Å^2 was significantly higher than the peak of menthol (about 4.142 vs. 0.741) and then this trend decreased with the increase of σ, and at σ 0.016 e/Å^2, the peak related to menthol was higher.

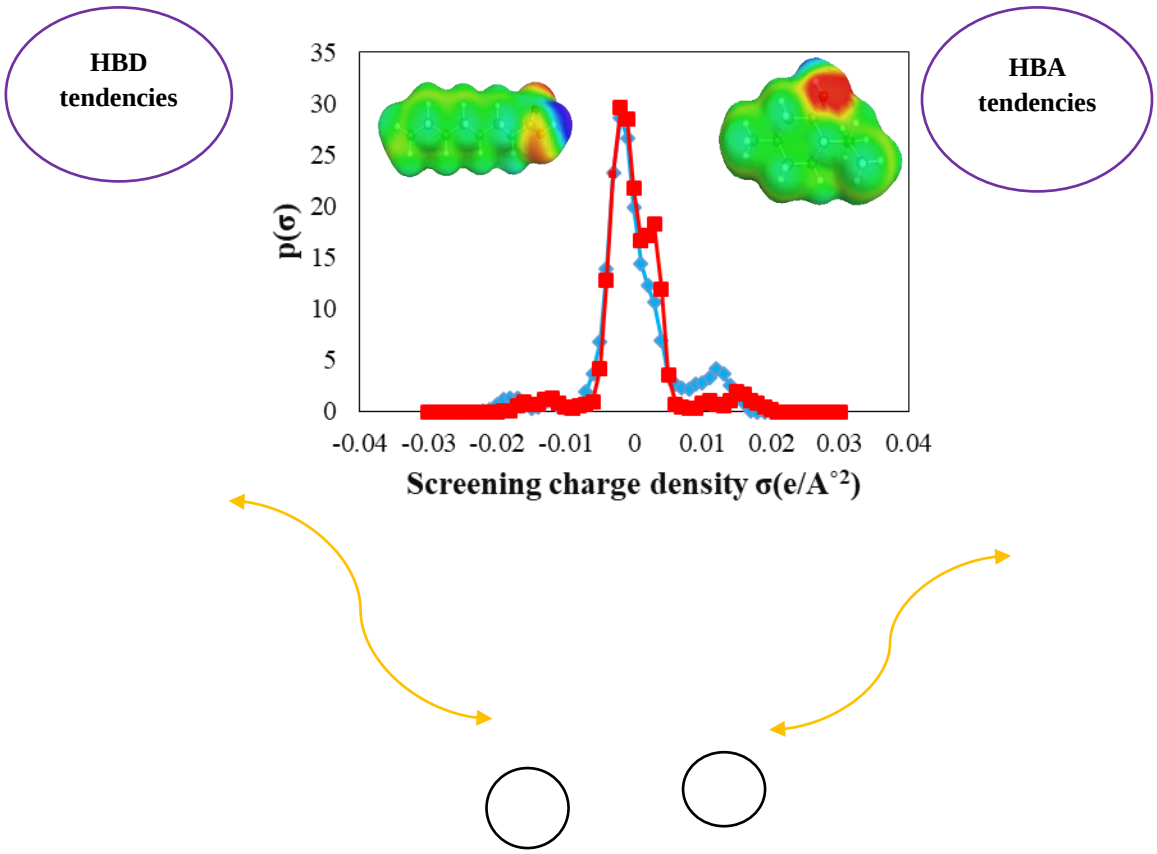

Figure 8. Sigma profiles of menthol (red), Caprylic acid (blue) and their sigma-surfaces representation

Conclusion

Molecular dynamics simulations were performed on the Menthol and Caprylic acid-based DES with Caprylic acid (CAP) as the HBD and menthol (MEN) as HBA at the temperature of 298.15 K. The structural analyses, namely RDF and SDF were then conducted to illustrate and confirm the formation of MEN-CAP, and MEN-MEN hydrogen bonds; the results were used to demonstrate the importance of $CAP_{HA}...{}_{O1}MEN$ interactions in the formation of the hydrogen bond network and the results showed that the number of H-bonds formed between MEN and CAP is more than between MEN-MEN. Dynamical properties such as MSD with respect to time were drawn; these were in good agreement with the results of previous analyses. Also, the possible molecular interactions of the mixture of HBA and the HBD (*i.e.* electrostatic, polar, and hydrogen bonding interactions) can be predicted through σ-profiles. These results, therefore, suggested that at the eutectic temperature, the presence of the ring and the OH group of menthol plays an effective role in establishing strong hydrogen bonds.

Because possible molecular interactions of HBA and HBD mixture (i.e. electrostatic, polar and hydrogen bond interactions) can also be predicted through σ profile, COSMO-RS analysis also showed that in the structure of MEN and CAP, the part corresponding to the hydroxyl and carboxylic group is more active and the charge density is concentrated in those points, and on the other hand, CAP's donating power and MEN's hydroxyl group's receiving power is greater.

Acknowledgments

This work has been supported by Azarbaijan Shahid Madani University.

References

[1] Brennecke, J.F. Maginn, E.J. American Institute of Chemical Engineers. AIChE Journal. 2001, 47- 84.

[2] Zhang, Q. Vigier, K.D.O. Royer, S. Jérôme, F. Chemical Society Reviews. 2012, 7108-46.

[3] Li, X. Wan, M. Gao, L. Fang, W. Scientific reports. 2016, 1-17.

[4] Kirchhoff, M.M. Environmental science & technology. 2003, 5349-53.

[5] Sas, O.G. Villar, L. Domínguez, Á. González, B. Macedo, E.A Environmental Technology & Innovation. 2022, 25-37.

[6] Humphrey, W. Dalke, A. Schulten, K. Journal of molecular graphics. 1996, 33-38.

[7] Wojeicchowski, J.P. Ferreira, A.M. Abranches, D.O. Mafra, M.R. Coutinho, J.A. ACS Sustainable Chemistry & Engineering, 2020,12132-41.

[8] Martínez, L. Andrade, R. Birgin, E.G. Martínez, J.M. Journal of computational chemistry. 2009, 157-164.

[9] Acun, B. Hardy, D.J. Kale, L.V. Li, K. Phillips, J.C. Stone, J.E. IBM journal of research and development. 2018, 1-4.

[10] Davidchack, R.L. Handel, R. Tretyakov, M. The Journal of chemical physics. 2009, 130-136

[11] Papapetrou, A. Proceedings of the Physical Society. Section A. 1951, 57-64.

[12] Sneha, P. Doss, C.G.P. Advances in protein chemistry and structural biology. 2016,181-224.

[13] Shah, D. Mansurov, U. Mjalli, F.S. Physical Chemistry Chemical Physics. 2019, 17200-8.

[14] Zikri, A.T. Pranowo, H.D. Haryadi, W. Indonesian Journal of Chemistry. 2020, 383-90.

[15] Reddy, T.D.N. Mallik, B.S. Physical Chemistry Chemical Physics. 2017,10358-70.

[16] Brehm, M. Kirchner, B. ACS Publications, 2011.

[17] Perkins, S.L. Painter, P. Colina, C.M. The Journal of Physical Chemistry B. 2013 10250-60.

[18] Kowsari, M.H. Fakhraee, M. Journal of Chemical & Engineering Data. 2015, 551-60.

[19] Marsh, K.N. ACS Publications, 2006.

[20] Lemaoui, T. Darwish, A.S. Hammoudi, N.E.H. Abu Hatab, F. Attoui, A., Alnashef, I.M. Industrial & Engineering Chemistry Research. 2020, 13343-54.

Communications In Catalysis
Vol. 2, No. 1, 2023, pp.50-61
DOI: 10.22049/CIC.2023.28350.1030

Azarbaijan Shahid Madani University

Molecular Insight into Dynamic and Structural Properties of the Deep Eutectic Solvent Based on Choline Chloride and Stearic Acid: A Molecular Dynamics Study

Samaneh Barani Pour [1], Mitra Dabbagh Hoseini Pour [2], Jaber Jahanbin Sardroodi [3,*] , Dr. Alireza Rastkar Ebrahimzadeh [4], Mohammad Sadegh Avestan[5]

[1,2,3,4] Department of Chemistry, Faculty of Basic Sciences, Molecular Science and Engineering Research Group (MSERG), Molecular Simulation Lab, Azarbaijan Shahid Madani University, Tabriz, Iran

[5] Department of Chemistry, University of Cincinnati, Cincinnati, OH 45221, United States

E-mail adress: jsardroodi@azaruniv.ac.ir

Received: 2023-02-22, Accepted: 2023-03-14

Abstract

In this work, the Structural and dynamic properties of eutectic solvents of choline chloride (Ch^+ Cl^-) and stearic acid (STA) were investigated using molecular dynamics simulations. Structural properties of the binary mixture of STA and [Ch^+] [Cl^-] with a molar ratio of 1:1 show a strong interaction between the (COOH) of STA and Cl^- anion in the binary mixture. Compared to the low molecular mass of the chloride anion, the strong interaction between the anion and HBD led to a decrease in the migration of this ion compared to acid. The results showed that Cl^- anion is an effective species in binary mixtures, playing a key role formation of deep eutectic solvents.

Keywords: MD Simulations; Stearic acid; Choline chloride; Deep eutectic solvent; Dynamic and Structural properties.

Introduction

In order to reduce human damage to the environment, green technology is to be seriously looking g new solvents to replace toxic and volatile organic solvents which produce a part of dangerous air pollutant gases [1]. The synthesis and use of ionic liquids (ILs) are the main developments in this field. Although ILs have attracted a lot of attention and many research articles have been published in this field, these solvents have not been well received in the industry due to their expensively. These solvents, which were called molten salts [2], are liquid at room temperature and they have unique physical and chemical properties such as high thermal stability, non-volatility, non-flammability and, adjustable polarity. Each of these properties can be adjusted by changing anion or cation in ILs [3]. Despite the diverse ability of these compounds, there are many limitations such as poor degradability, toxicity, corrosion, and high cost, which prevent their use in the chemical industry. Therefore, a new generation of solvents has appeared that is called deep eutectic solvents (DESs). DESs have a similar structure to ionic liquids and are a suitable alternative for ILs. The main advantage of DESs to ionic liquids is their easy synthesis. Deep eutectic solvents are a mixture of two or more components in which instability of charge between two donors and acceptor of hydrogen bond components is responsible for reducing the melting point of the eutectic mixture [4]. The common DESs are based on choline chloride as a hydrogen bond acceptor and carboxylic acids, citric acids, succinic acids, and other hydrogen bond donors such as urea and glycerol [5]. Choline chloride is a very cheap, biodegradable, and non-toxic from quaternary ammonium salt (QAS) [6]. Although DESs are made of choline chloride as an ionic species, DESs cannot be considered ionic liquids due to these solvents can be composed of non-ionic species. Though DESs have properties similar to ionic liquids, deep eutectic solvents have many advantages, including low price, easy preparation, nontoxic and biodegradable which can be used in various applications such as extraction. Molecular dynamics (MD) simulation is a new technique that is widely used to investigate the dynamic and structural properties of the binary mixture. In the MD simulation method, molecules are allowed to interact with each other for a certain period of time under the known classical laws. The main basis of this effective method is the solution of Newton's equations of motion for the individual particles (atoms, ions, …). MD simulation provides information at the microscopic level such as the new position of molecules. In fact, molecular dynamics

is the relationship between the structure of molecules and the gradual movement of molecules with time.

The instability of hydrophilic solvents based on ammonium salts in contacting with water has motivated the design of hydrophobic eutectic solvents as green alternatives for organic solvents. Recently, a large number of hydrophobic eutectic solvents based on natural compounds especially menthol, has been used to remove and separate micro-pollutants.

A quick look at the eutectic solvents presented in the literature shows that most of these solvents are very hydrophilic. The instability of hydrophilic solvents based on ammonium salts in contact with water has motivated the design of hydrophobic eutectic solvents as green alternatives for organic solvents. Recently, a large number of hydrophobic eutectic solvents based on natural compounds, especially menthol, have been used to remove and separate micro-pollutants [7]. Also, increasing the solubility of drugs, and extracting drugs from their synthesis environment are the pharmaceutical applications of these solvents [8]. Hydrophobic eutectic solvents based on terpenes and fatty acids are widely used in the extraction of biomolecules such as tryptophan, isophthalic acid, vanillin, and polycyclic aromatic hydrocarbons from aqueous solutions [9].

Therefore, the main goal of this article is to design and describe the structural properties of the eutectic mixture including choline chloride and stearic acid by MD simulation. The liquid phase of the binary mixture of choline chloride and stearic acid in its pure state has been investigated.

The structural and transport properties of the eutectic mixture of choline chloride salt and stearic acid were investigated at 353 K. The transport properties of the species in the binary mixtures were analyzed by studying the mean square displacement (MSD) of the centers of mass of the species, and diffusion coefficients.

Also, assessed structural properties include the radial distribution functions (RDFs), the hydrogen bonding network between species, and spatial distribution functions (SDF). Structural properties of the binary mixture of STA/ Ch^{+} Cl^{-} with a molar ratio of 1: 1 showed a decrease in the strong interaction between Choline and acid.

The analysis of the atom-atom RDFs and Spatial distribution functions (SDF) of the eutectic mixture was indicated the hydrogen atoms that dependent on the hydroxyl group of STA molecules are surrounded by chloride anions. In general, the results of this work are presented evidence that interactions between chloride anions and the HA atom of the carboxyl

groups of stearic acid play a key role in the formation of eutectic solvents based on STA and $Ch^+ Cl^-$.

Results and discussion

Radial distribution function

Radial distribution function or pair correlation function is a useful quantity in molecular dynamics simulation, which represents the probability of finding a molecule at a certain distance from an arbitrary central molecule. This function is widely used to understand effective interactions between molecules and is represented by g(r), where r is the intermolecular distance. The mathematical relationship of this equation is as follows:

$$g(r) = {dN}/{(4\pi r^2 p)} \qquad (1)$$

In equation (1), dN and ρ represent the number of molecules in a distance of radius (r) around the reference molecule and the average density of system, respectively [10]. The Intensity of the g(r) peak is increased and reduced, respectively, with increasing the number and distance of the molecules around the reference molecule.

The radial distribution function provides important insights into the structural properties of binary mixtures.

The change in the position of the molecules can be found by observing the difference in the position, height, and width of the peaks. RDF between Cl^- anion around Ch^+ cation and STA in the eutectic mixture is drawn in Figure 1a. RDF related to choline chloride Salt around STA has one sharp peak at distances of 2 Å.

The sharp peak of RDF between Ch^+ and Cl^- in the binary mixture was significantly reduced in the presence of acid molecules. In other words, STA molecules are surrounded by Cl^- anions (see Figure 1b).

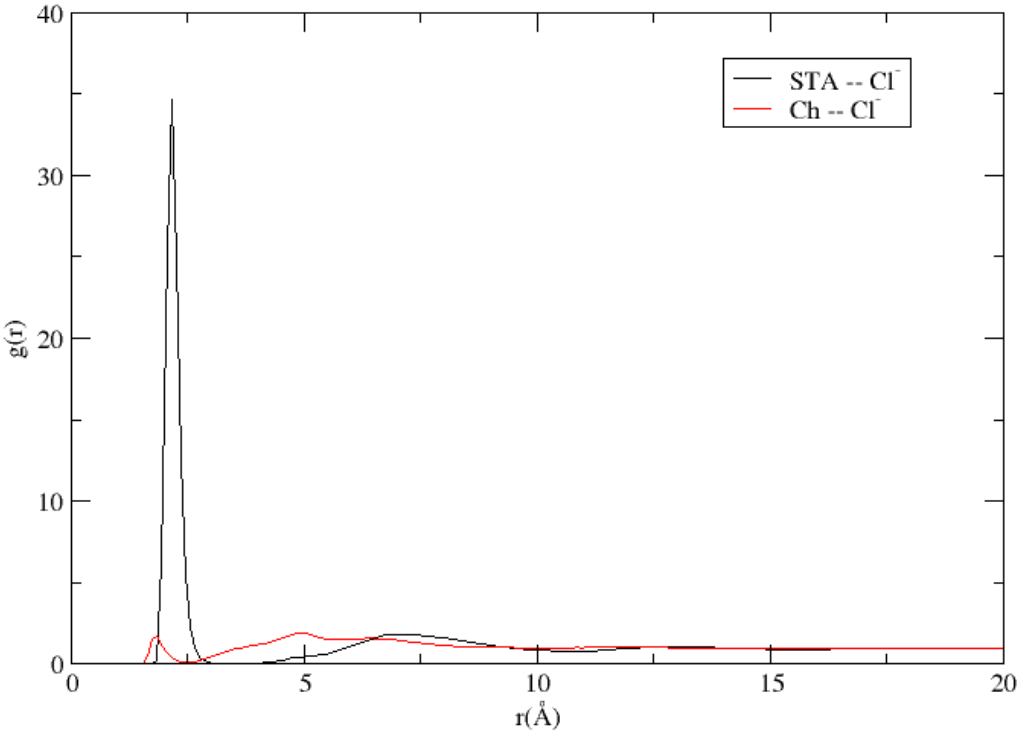

(a)

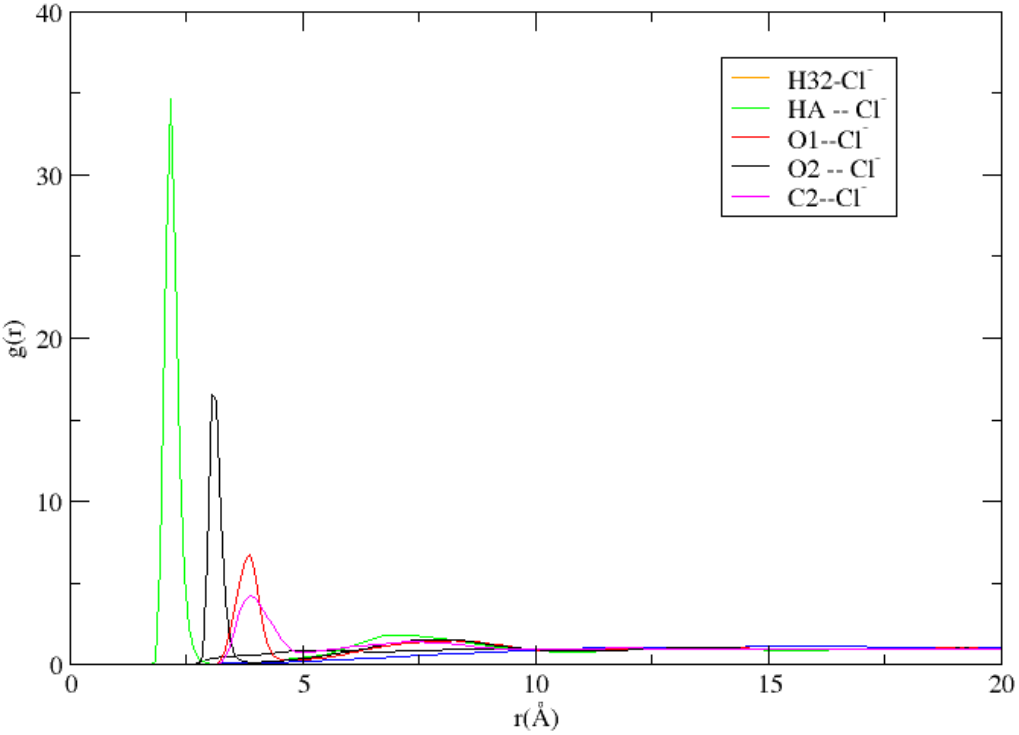

(b)

Figure 1. a) RDF between Cl^- anion around Ch^+ cation and STA in the eutectic mixture at 353 K and b) RDF between Cl^- anion around different atom of STA in the eutectic mixture at 353 K

Hydrogen-Bond Analysis

To understand which of the components of choline chloride can favorably establish strong hydrogen bonds with hydrogen bond donor, the average number of H-bonds between HBD and HBA was evaluated in the binary mixture. The number of hydrogen bonds between HBA and HBD was calculated by the VMD plugin. The cutoff distance of 3.5 Å and an angle cutoff for ∠DHA of 150° were selected for H-bond analysis. The average number of hydrogen bonds is obtained vis the fitting of Equation (2)

$$F(X) = \frac{a}{\sigma\sqrt{2\pi}} exp^{\frac{-(X-\bar{X})^2}{2\sigma^2}} \qquad (2)$$

Where σ, and $\bar{X}$ are the standard deviation and the average number of hydrogen bonds, respectively [11]. The distribution of the number of H-bonds between cation: STA and the anion: STA is shown in Figure 2. The hydrogen of the COOH group of Stearic acid interacts favorably with the anion of salt, forming a hydrogen bond that is stronger than the intermolecular interaction at the pure state.

The number of hydrogen bonds between HBA and HBD of eutectic solvent may not be adequate to justify the interaction between the two species. Hydrogen bond percent occupancies of the HA atoms of STA and Cl^- anion in the binary mixture at 353 K are shown in Figure 3. It is clearly seen that the hydrogen bond between anion and STA is more stable compared to other species.

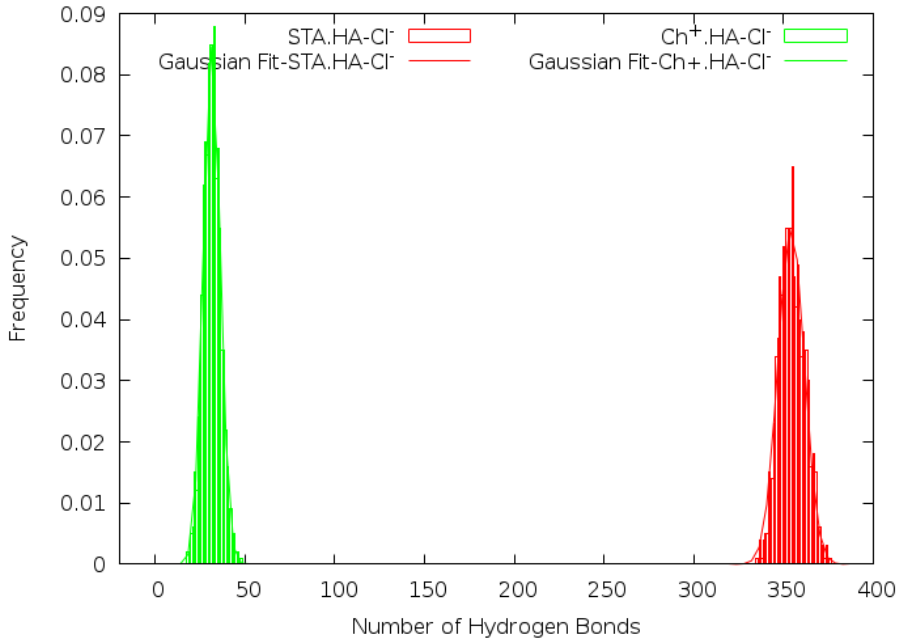

Figure 2. The distribution of the hydrogen bond between STA and Salt in the binary mixture at 353 K

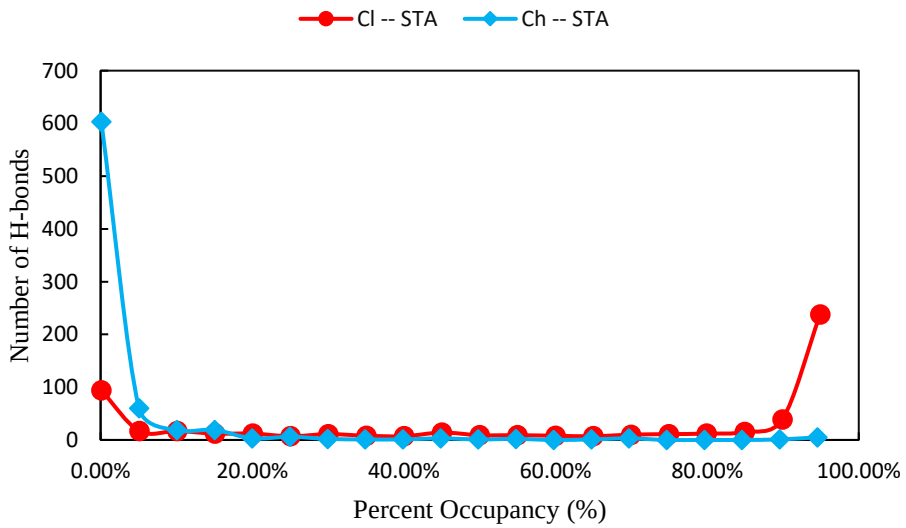

Figure 3. Hydrogen bond percent occupancies for Salt: STA in the binary mixture at 353 K

Spatial distribution function

The spatial distribution function (SDF) is another useful tool to visualize the distribution of molecules, which has provided valuable information about the three-dimensional density distribution of a species around a central molecule. The three-dimensional density distribution of

different species around a reference molecule is obtained using TRAVIS software [12]. To determine SDFs in the $[Ch^+]$ $[Cl^-]$ /STA binary mixture, the C9 atom and N atom are considered as the center of the mass stearic acid molecule and choline chloride, respectively. Investigating the spatial distribution function of the binary mixture shows that the distribution of choline chloride molecules around the carboxylic acid group has the highest value. Also, the distribution of choline chloride and acid molecules around the choline cation as a reference molecule shows the tendency of the hydroxyl group of the Ch^+ cation to form the intermolecular hydrogen bonds between HBA and HBD.

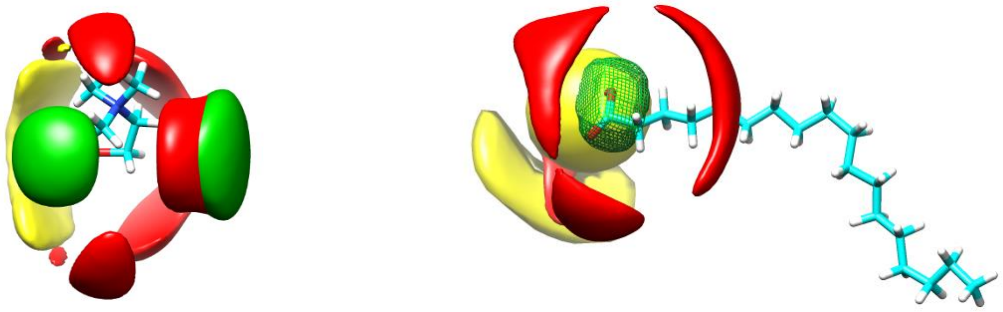

(a) (b)

Figure 4. Spatial distribution functions (SDFs) of the components of the binary mixtures at 353 K. a) SDFs of STA around Choline Chloride molecules in the binary mixture, b) SDFs of Choline Chloride around STA molecules. Green isosurfaces correspond to Cl^-, red isosurfaces are choline Cation

Dynamical and transport properties

Previous studies on deep eutectic solvents have shown that there is a significant relationship between intermolecular interactions and dynamic properties. Thus, self-diffusion coefficients, D_{self}, were calculated for the binary mixture. D_{self} were obtained by the well-known Einstein equation:

$$D = \frac{1}{6}\lim_{t\to\infty}\frac{d}{dt} < \Delta r(t)^2 > \qquad (3)$$

Where $\Delta r(t)^2$ is defined as the distance traveled by the specie i per unit of time or MSD [13]. In order to investigate the dynamic behavior of the molecules, the mean-square displacement (MSD) of the center of mass for each HBA/HBD was calculated in the binary mixture. MSDs of the center of mass for each $[Ch^+][Cl^-]$

/stearic acid as a function of time are drawn in Figure 5. The MSD of the FAs molecule is larger than that of the chloride anion. It seems that the stability of the H-bond between the HBA and HBD can lead to decreasing the self-diffusion coefficients of species in the binary mixture.

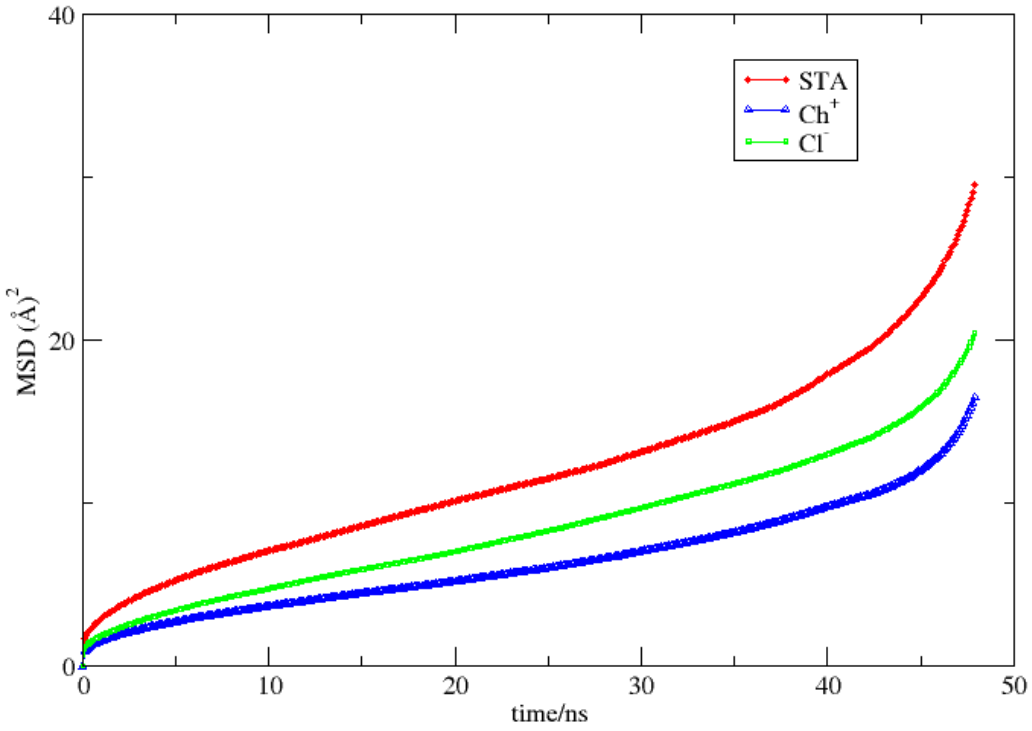

Figure 5. The MSDs of the species for the binary mixtures at 323 K

To ensure the values of Ds, the diffusion coefficient has been calculated in the diffusive region (β = 1). This parameter was proposed to determine the location of the diffusive regime by Del Popolo´ and Voth. In the diffusive region, MSD has a good relationship with time, therefore the Ds are taken in this region.

$$\beta = \frac{\mathrm{d}\log_{10} < \Delta r(t)^2 >}{\mathrm{d}\log_{10} t} \qquad (4)$$

$$< \Delta r(t)^2 >= \frac{1}{N}\langle \sum_{i=1}^{N} |r_i^c(t) - r_i^c(0)|^2 \rangle \quad (5)$$

$r_i^c(t)$ and $r_i^c(0)$ are positions of the center of mass of a molecule at time t and 0, respectively [14]. Self-diffusion coefficients for choline (D^+), chloride (D^-) and the HBD (D_{HBD}) at the temperatures listed in Table 1. The hydrogen bonding results confirm the low value of diffusion coefficient of the anion compared to the acid.

Table 1. Self Diffusion coefficients for HBA and HBD in the binary mixture at 353 K

		MSD		
system	**T/K(323)**	**D $_{Ch^+}$ (β)**	**D $_{Cl^-}$ (β)**	**D $_{HBD}$ (β)**
DES	353	0.0391	0.0540	0.7160

Conclusion

The HA $_{STA}$ -- anion RDFs have a main peak at a distance of 2 Å that the H-bonding formation between anion and acid in the binary mixtures. It seems that chloride anion plays a key role in the formation of eutectic solvents based on [Ch^+] [Cl^-] and STA. The structural correlation between anion and acid was confirmed the using spatial distribution function (SDF). The low slope of MSD of anion can be attributed to the stability of the H-bond between anion and hydrogen atoms of carboxyl (-COOH) of STA.

Computational Details

In order to determine whether DESs based on Stearic acid (STA) and choline chloride ([Ch^+] [Cl^-]) can be formed, first, the binary mixtures of STA and [Ch^+] [Cl^-] were simulated at a pure state. Initial configurations of the binary mixtures were prepared using PACKMOL package [15]. The all of MD simulation were carried out by NAMD 2.13 package [16]. For eliminating border effects, periodic boundary conditions (PBC) were used along with the X, Y, and Z-axis. To initiate the simulation, 2000000 steps of minimization was current out to remove the bad contacts of the initial configuration. Then, the binary mixture was heated to 353K in 30000 steps. Finally, the MD simulations were performed for 30 ns in NPT ensembles at 1 bar pressure and desired temperature. For this purpose, the Langevin thermostat, and Nose-Hoover Langevin piston barostat was employed to keep the temperature constant in simulations [17]. The Particle Mesh Ewald (PME) technique was used to calculate the long-range electrostatic interactions [18]. The cutoff distance for the calculation of the short-ranged Lennard-Jones interaction was set at 12 Å [19]. CHARMM36 force field parameters were used for choline chloride salt.

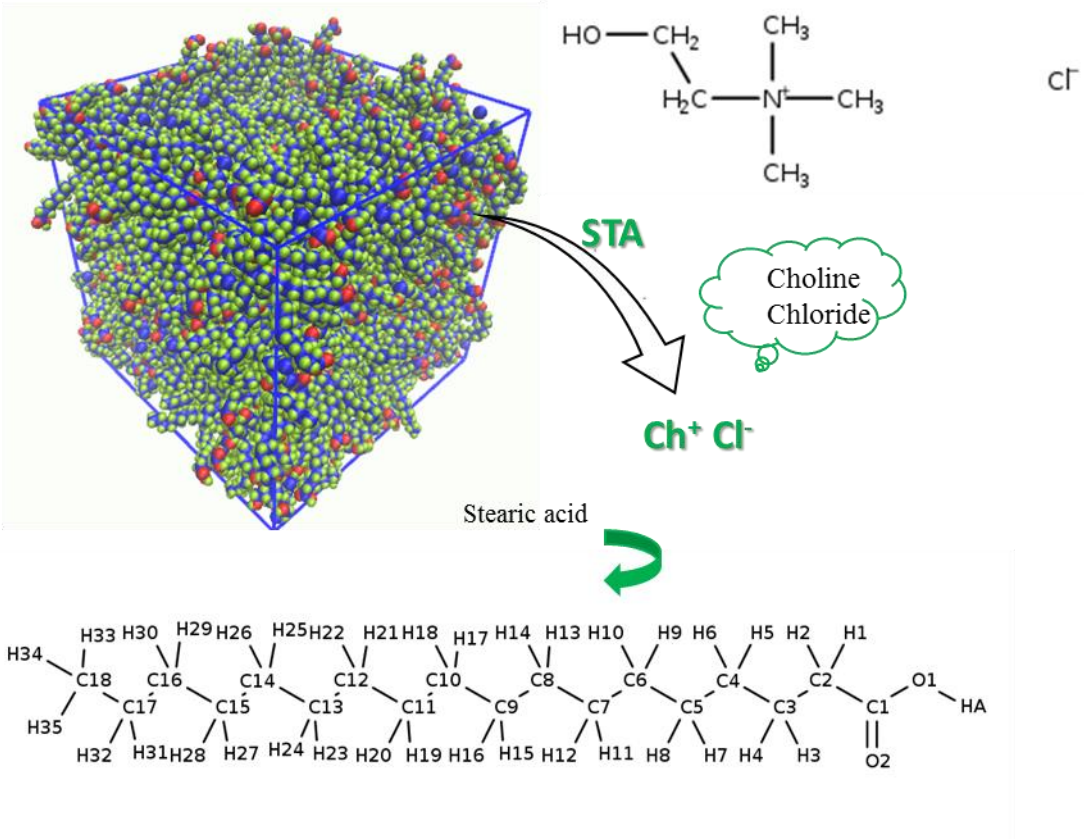

Figure 6. Schematic of the chemical structures of (a) choline [Ch $^{+}$] and (b) stearic acid with the main atomic labels

Acknowledgments

This work has been supported by Azarbaijan Shahid Madani University.

References

[1] Dua, R., Shrivastava, S., Shrivastava, S. L., Srivastava, S. Middle-East Journal of Scientific Research, 2012, 846-855
[2] Tavares, A. P., Rodríguez, O., Macedo, E. A. IntechOpen, 2013
[3] Pena-Pereira, F., Namieśnik, J. ChemSusChem, 2014, 1784-1800
[4] van Osch, D. J., Zubeir, L. F., van den Bruinhorst, A., Rocha, M. A., Kroon, M. C. Green Chemistry, 2015, 4518-4521
[5] Dwamena, A. K. Separations, 2019, 6- 9
[6] Smith, E. L., Abbott, A. P., Ryder, K. S. Chemical reviews, 2014, 11060-11082
[7] Van Osch, D. J., Dietz, C. H., Warrag, S. E., Kroon, M. C. ACS Sustainable Chemistry & Engineering, 2020, 10591-10612
[8] Nair, P. C., Miners, J. O. In silico pharmacology, 2014, 1-4
[9] Martins, M. A., Crespo, E. A., Pontes, P. V., Silva, L. P., Bülow, M., Maximo, G. J., Batista, E. A., Held, C., Pinho, S. P., Coutinho, J. A. ACS Sustainable Chemistry & Engineering, 2018, 8836-8846
[10] Mendez-Morales, T., Carrete, J., Bouzon-Capelo, S., Perez-Rodriguez, M., Cabeza, O., Gallego, L. J., Varela, L. M.

The Journal of Physical Chemistry B, 2013, 3207-3220
[11] Pour, S. B., Sardroodi, J. J., Ebrahimzadeh, A. R. Molecular Graphics and Modelling, 2022, 114- 126
[12] Brehm, M., Kirchner, B. ACS Publications, 2011, 28- 42
[13] Pour, S. B., Sardroodi, J. J., Ebrahimzadeh, A. R. Journal of Molecular Liquids, 2021, 334- 352
[14] Del Pópolo, M. G., Voth, G. A. The Journal of Physical Chemistry B, 2004, 1744-1752.
[15] Martínez, L., Andrade, R., Birgin, E. G., Martínez, J. M. Journal of computational chemistry, 2009, 2157-2164.
[16] Nelson, M. T., Humphrey, W., Gursoy, A., Dalke, A., Kalé, L. V., Skeel, R. D., Schulten, K. The International Journal of Supercomputer Applications and High Performance Computing, 1996, 251-268.
[17] Liu, J., Li, D., Liu, X. The Journal of chemical physics, 2016, 145- 164
[18] Shi, B., Sinha, S., Dhir, V. K. The Journal of chemical physics, 2006, 121-137
[19] Benazzouz, B., Zaoui, A. Applied Clay Science, 2012, 44-51.

Communications In Catalysis
Vol. 2, No. 1, 2023, pp.62-73
DOI: 10.22049/CIC.2023.28331.1028

Azarbaijan Shahid Madani University

Controlled Electrodeposited of Cobalt Oxide Nanoparticles on Graphenized Pencil Lead Electrode as Efficient Electrocatalyst for Oxygen Evolution Reaction in Alkaline Medium

Rahim Mohammad-Rezaei[1*], Sahand Soroodian[2]

[1,2]Department of Chemistry, Faculty of Basic Sciences, Azarbaijan Shahid Madani University, Tabriz, Iran

E-mail: r.mohammadrezaei@azaruniv.ac.ir, r.mohammadrezaei@ymail.com

Received: 2023-02-18, Accepted: 2023-03-14

Abstract

In this study cobalt oxide nanoparticles were electrodeposited on the surface of graphenized pencil lead electrode (GPLE) as a low cost and efficient electrocatalyst for the OER in alkaline media. The prepared cobalt oxide modified GPLE (CoOx/GPLE) was carefully characterized by scanning electron microscopy, energy-dispersive X-ray spectroscopy, electrochemical impedance spectroscopy and cyclic voltammetry techniques. The developed electrocatalyst represents remarkably low OER overpotential of 1.41V (vs. RHE) at the current density of 10 mA cm^{-2} and Tafel slope of 149 mV dec^{-1} in 0.1 M KOH solution. The CoOx/GPLE was highly stable and capable for maintaining catalytic activity for at least 5 h. Due to distinctive electrical conductivity, high mass transfer, and adequate active sites of GPLE, the electrocatalytic activity of the cobalt oxide nanoparticles were incredibly improved in CoOx/GPLE.

Keywords: Oxygen evolution reaction, Graphene, Cobalt oxide nanoparticles

Introduction

Abundance, ease of discovery, transportation and usability has made the fossil fuels such as natural gas, coal, oil and gasoline as the first source of energy for industrial and daily uses since 18th century. Massive consumption of these substances, can give off big amounts of carbon dioxide and sulfur dioxide leading to greenhouse effect and acid rains respectively. Due to global warming, oil leaks caused from transportations and oil rigs and non-renewable nature of these fuels, finding suitable alternatives energy source is necessary. In many studies hydrogen is proposed as a green, renewable and cheap candidate to fill the role. For this propose, researches are being conducted in different fields such as fuel cells [1], photocatalysis [2], electrolysis [3], biomass and CO_2 conversion technologies [4] to overcome the hydrogen evaluation challenge. Among these techniques, electrolysis and water splitting has various merits such as being pollution free process, high degree of purity, simplicity of the process and abundance of resource [5-8].

The process of electrochemical water splitting is a chemical reaction for splitting of water into its origin elements, which provides an efficient way for producing hydrogen. Water splitting consists of two half reactions of oxygen evaluation reaction (OER) and hydrogen evaluation reaction (HER). Kinetically, the OER is tardy and it necessitates over potential which are larger than the assessed theoretical over potential (1.23 V) [9]. For this reason, an efficient electrocatalysts needed to hasten reaction rate, reduce over potential, and improve the energy conversion efficiency. Noble metals and their oxides such as Ru, Pt and Pd have been used as the most efficient electrocatalysts for the task of water splitting [10]. Considering scarcity and high expenses of these elements, demand a suitable replacement which to be stable, cheap and active in various conditions is required. For this purpose, transition metal oxides/hydroxides, metal sulfides and

metal phosphides has drawn lots of attentions.

New studies tend to employ cobalt based electrocatalysts since they fulfill mentioned conditions [11-13]. Abundance, low expense, and its worthy electrocatalytic behavior for water splitting reactions make the cobalt-based materials as suitable choice for present study.

According to previous studies, exfoliation of pencil lead electrode (PLE) is a newly emerged method for obtaining graphene in a simple and inexpensive manner [14]. By applying anodic and cathodic potentials and successively, PLE exfoliates into graphenized pencil lead electrode (GPLE). Owing to outstanding properties of GPLE such as high surface to volume ratio and excellent conductivity and electron transfer rate, electrodeposition of cobalt oxide on GPLE could result an efficient electrocatalyst for OER.

In this study, cobalt oxide nanoparticles were controllably electrodeposited on the surface of GPLE. The developed electrocatalyst was successfully used for OER in alkaline media. High electrical conductivity, fast mass transfer, adequate active sites and cheapness have made the developed electrocatalyst as stable and utilizable electrocatalyst for OER.

Experimental

Chemicals and Materials

The pencil lead graphite rod (HB grade) was purchased from Rotring Co. LTD, Germany (R 505210N) with a diameter of 2.0 mm. $CoCl_2 \cdot 6H_2O$ was provided by Sigma-Aldrich (St. Louis, MO, USA). Standard solution of 0.1 M Co (II) and 0.1 M KNO_3 were prepared and stored at 4 ˚C for further use and diluted as necessary. All other chemicals were of analytical grade and were used without further purification.

Apparatus

Cyclic voltammetry (CV) and amperometry studies were carried out using an AUTOLABPGSTAT-204 (Metrohm, Switzerland) equipped with an USB electrochemical interface and driven NOVA software in conjunction with a

three-electrode system and a personal computer for data storage and processing. The utilized three electrode system was composed of a saturated (KCl) calomel electrode (SCE) as the reference electrode, a platinum wire as the auxiliary electrode and modified electrodes as the working electrodes. Scanning electron microscopy (SEM) images were obtained using a Phenom ProX scanning electron microscope (Hitachi, Tokyo, Japan). An AC/DC power supply was used for electrochemical exfoliation of pencil lead electrodes.

All the potentials recorded in this research work were converted to the reversible hydrogen electrode (RHE) values using the following equations:

$$E_{\mathrm{RHE}} = E_{\mathrm{Ag}/\mathrm{AgCl}} + 0.0591\ \mathrm{pH} + 0.197 \quad \text{(Eq. 1)}$$

and the overpotential (η) was acquired by the following equation:

$$\eta = E_{\mathrm{RHE}} - 1.23\ \mathrm{V} \quad \text{(Eq. 2)}$$

Preparation of graphenized pencil lead electrode

For preparation of GPLE, the obtained pencil lead electrodes (diameter of 2 mm) were polished using polishing papers (mesh of 800 and 1200), and after conjunction with a copper wire, the resulted electrode was wrapped in Teflon stripes to a point that only tip left exposed. Two of the resulting pencil lead electrodes as anode and cathode was rinsed with doubly distilled water and dipped upright in 1 M sulfuric acid solution for exfoliation process. The electrochemical exfoliation was carried out by applying an optimized potential (alternating bias between +8 V and −8 V for 5 cycles and each cycle consisting of 1 second). Through applying positive potentials to the PLE, positive charge at the electrode will be occurred, leading to attraction and intercalation of bulky negative ions such as sulfate anions. This process, in turn expands the interlayer spacing between graphene sheets and results in the subsequent exfoliation of the sheets. Similarly, in cathodic exfoliation by applying a negative bias to the PLE,

positively charged ions in the solution enter in between graphene layers, spacing sheets and aiding the exfoliation further. The prepared electrodes were left to dry in room temperature and stored until further use and modifications.

Preparation of cobalt oxide modified graphenized pencil lead electrode (CoOx/GPLE)

For electrodepositing of the CoOx on the fabricated GPLE, cyclic voltammetry method was employed. Figure 1 illustrates the successive CVs of the GPLE in 0.01 M Co (II) and 0.01 KNO_3 at the scan rate of 50 mV s^{-1}.

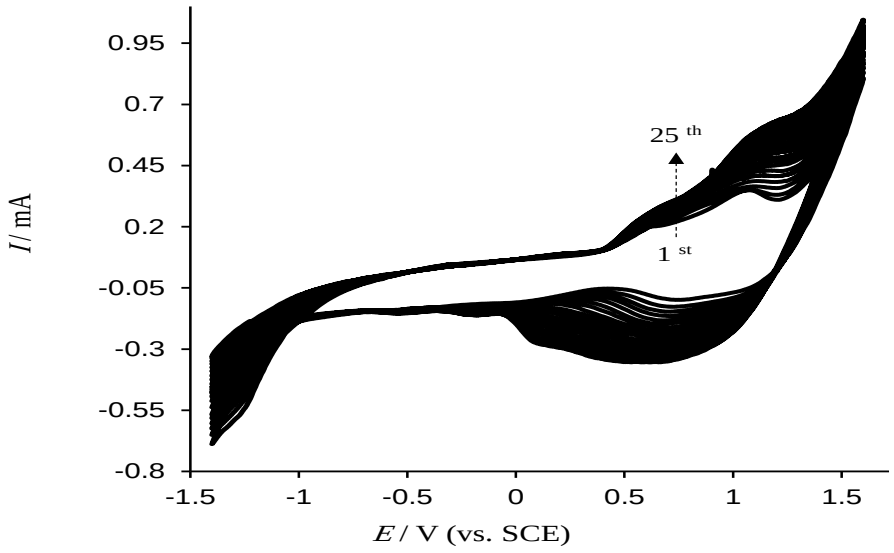

Figure 1. Cyclic voltammograms during the electrodeposition of cobalt oxide on GPLE in 0.01 M $Co(NO_3)^{2+}$ and 0.01 M KNO_3, scan rate of 50 mV s^{-1} for 25 cycles

At early cycles, two separate peaks appear at about 0.6 and 1.1 V, which gradually grows and merges into a single broad anodic peak in later cycles. Also, another cathodic peak was perceived at about 0.75 V which grows and broadens similarly. This uneven number of peaks and their location of occurrence indicates that this electrochemical process can be interpreted as quasi reversible [15]. Both of the oxidation and reduction peaks tend to intensify during increasing repetitive cycles indicating the deposition of CoOx on the

GPLE surface according to equations 3 and 4:

$$Co(OH)_2 + OH^- \longleftrightarrow CoOOH + H_2O + e^- \quad \text{(Eq. 3)}$$

$$CoOOH + OH^- \longleftrightarrow CoO_2 + H_2O + e^- \quad \text{(Eq. 4)}$$

Results and discussion

Characterization of CoOx/GPLE

For the purpose of studying characteristics of the CoOx/GPLE electrode, SEM images of the GPLE as well as fabricated CoOx/GPLE were acquired Fig. 2. As apparent in Figure 2A and 2B, exfoliation of graphite into a rough, jagged and three dimensional layered of graphene can be seen on the surface of GPLE. As these images show, a semi porous morphology was obtained by utilizing harsh exfoliation method. SEM Imaging of CoOx/GPLE electrode clearly depicts the fact that cobalt oxide nanoparticles are properly dispositioned and trapped in the spikey network of the graphene layers and has formed a granular nanocluster on porous exfoliated graphene layers (3C and 3D).

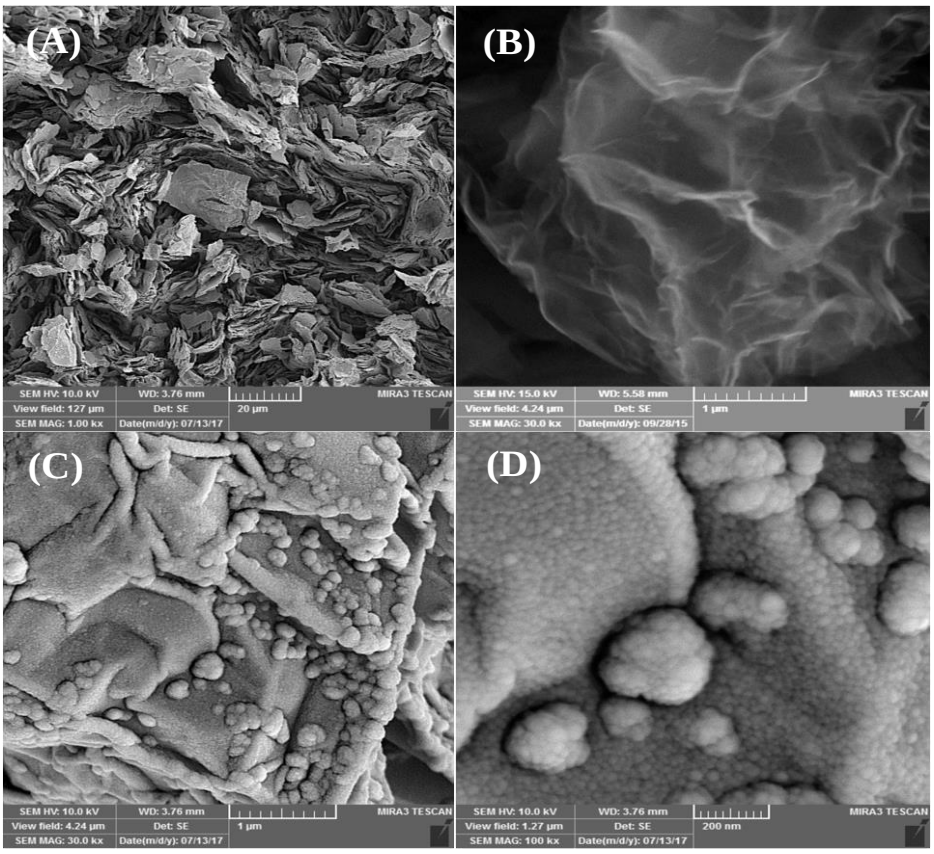

Figure 2. SEM images taken from surface of GPLE (A and B), and CoOx/GPLE at different magnifications (C and D)

Results from the acquired images supports the idea of suitability of the GPLE for the task of electrodeposition of solid-state transition metal oxides, and fabrications of desired electrochemical electrodes. Similarly, encrusted rough structure of GPLE could be supportive for mass transfer and stabilization of electroactive reagents in desired modified electrodes.

Electrochemical behavior of CoOx/GPLE

After completion of electrochemical deposition procedure of CoOx on GPLE, the fabricated electrodes were engaged in CV method for electrochemical characteristic assessment. Cyclic Voltammograms of CoOx/GPLE, GPLE, and PLE were assessed in 0.01 M solution of NaOH (pH=12) with potential window of -1 V to 0.9 V and scan rate of 0.05 mV s^{-1}. Comparison of the three obtained CVs are shown in Figure 3. As represented, there are no redox peaks for neither of PLE nor GPLE, albeit an amplified background current for GPLE is obvious. Attained electrochemical behavior of CoOx/GPLE is almost identical to its electrodeposition plot, but the redox peaks have occurred in different potential values.

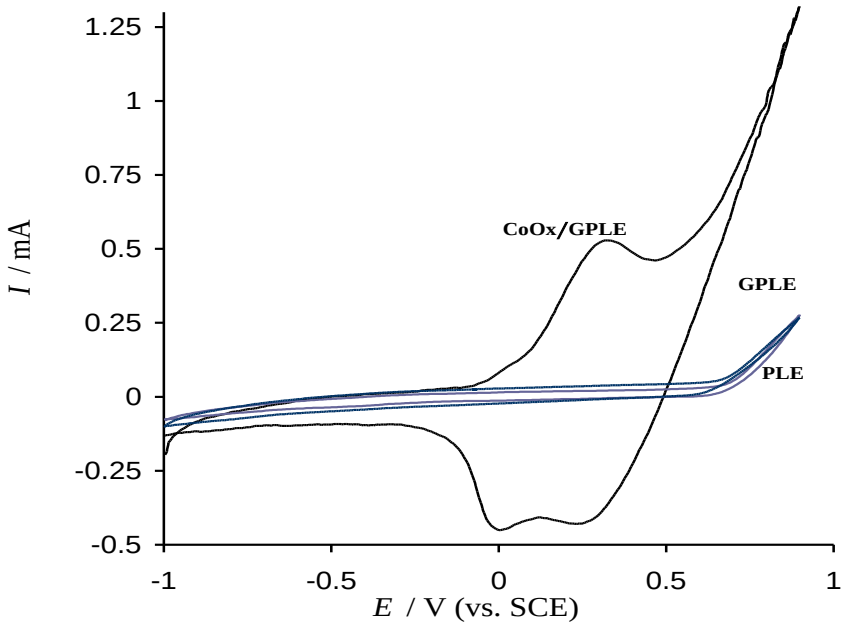

Figure 3. Cyclic voltammograms corresponding to electrochemical behavior of CoOx/GPLE in 0.1 M KOH, at the scan rate of 25 mVs^{-1}

In order to obtain more information about the nature of the electrode reaction, cyclic voltammograms of CoOx/GPLE were recorded in different scan rates (25 to 175 mV s^{-1}) in 0.01 NaOH (Figure 4). The well-ordered increase in all peaks current vs. scan rate express a linear behavior which anticipated for surface redox reactions.

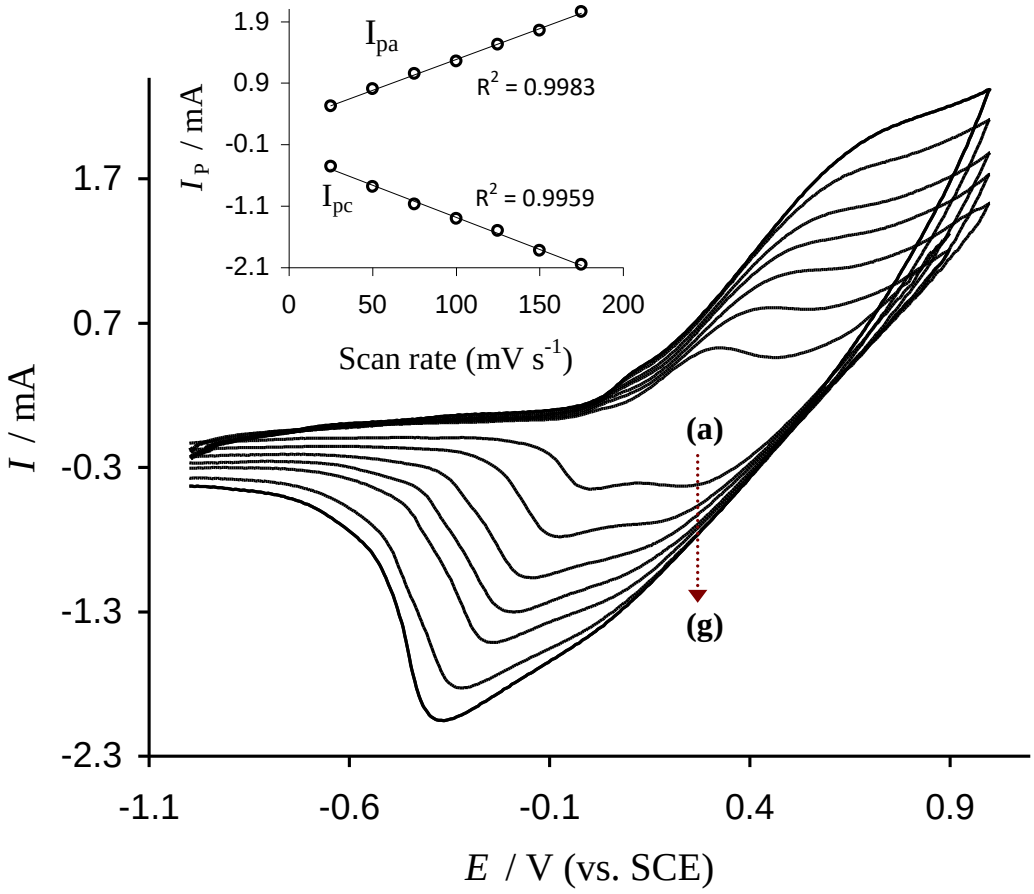

Figure 4. Cyclic voltammograms of the CoOx/GPLE in 0.1 M KOH solution (pH 12), at different scan rates; Inset shows the relation of anodic and cathodic peak currents vs. the scan rate

To compare the charge transfer rate of PLE, GPLE and CoOx/GPLE, Nyquist plots of the electrodes were recorded in the frequency of 0.1 to 10^5 HZ and the results was shown in Figure 5. As can be seen, the semi-circle radius of the Nyquist diagram for the CoOx/GPLE (c) in decreased in comparison with PLE (a) and GPLE (b) proving that charge transfer performance of CoOx/GPLE in intensified.

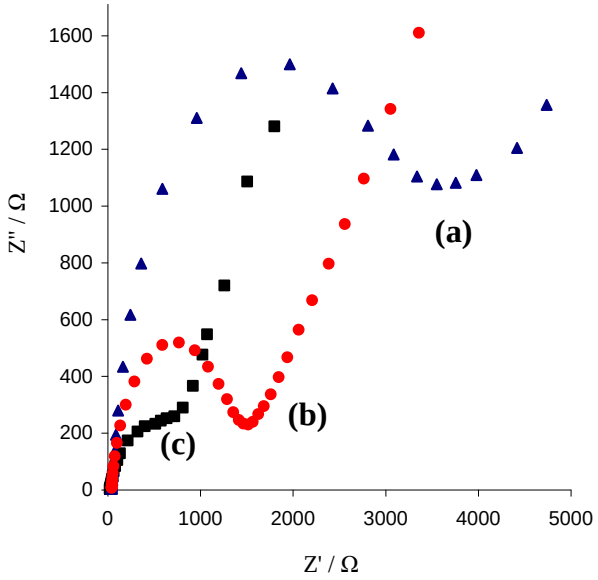

Figure 5. Nyquist plot of the PLE (a), GPLE (b) and CoOx/GPLE (c)

Oxygen evaluation reaction

For observing the electro-catalytic properties of prepared CoOx/GPLE, oxygen evaluation reaction has been conducted in 0.1 M KOH by employing linear sweep voltammetry method (LSV). The resulting LSVs of CoOx/GPLE, GPLE and PLE are represented in Figure 6A. By considering the current density of 10 mA cm^{-2}, the OER potential was shift to more negative value in the case of CoOx/GPLE proving its astonishing electrocatalytic performance in water oxidation. Also, the inset potential of CoOx/GPLE is more negative because of the high electrocatalytic ability of CoOx as well as elevated surface to volume ratio of the fabricated electrode.

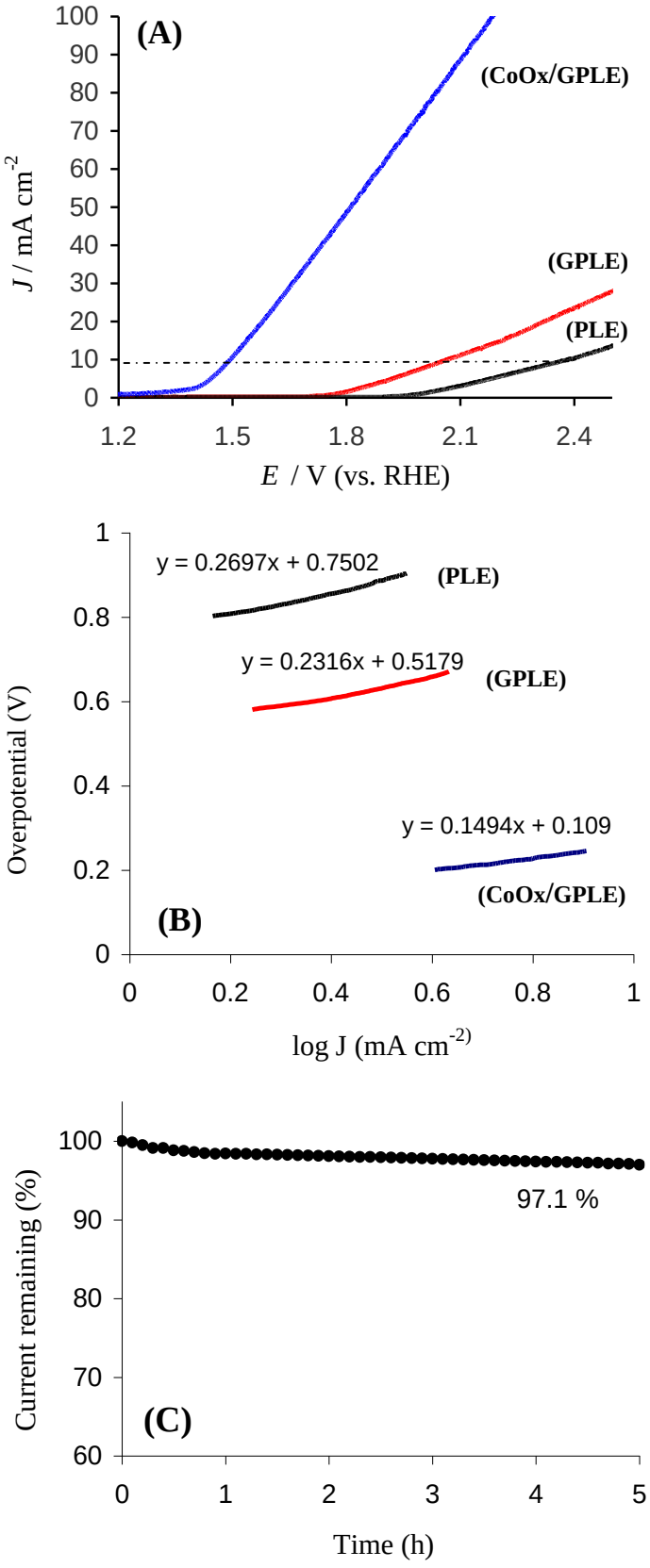

Figure 6. (A) OER curves and (B) Tafel plot of the CoOx/GPLE, GPLE and PLE; (C) OER I-t curve for stability assessment of CoOx/GPLE in a 0.1 M KOH solution

In order to evaluate the kinetic of OER on the electrode surfaces, the Tafel plot were recorded (Figure 6B) in 0.1 M KOH solution which are corresponding from Figure 6A. By comparing the results, it can be found that, CoOx/GPLE exhibits the highest slope in comparison with GPLE and PLE which reflect the suitable electrocatalysts behavior of CoOx/GPLE for the OER.

The matter of chemical and mechanical stability is vital for the developing of electro catalysts. The stability of fabricated Co-GPLE has been put to test for continues OER for 5 hours under the same conditions using E-t curve. As presented in Fig. 6C, after showing an initial drop, current density turns out to be rather stable and the values remain fairly fixated at this time period. Also, the OER test were conducted multiple times over a month using a single and same electrode. The recorded current densities did not show considerable changes proving high stability of the fabricated CoOx/GPLE.

Conclusions

In summary, a novel and efficient electrocatalyst for OER using graphenized pencil lead electrode modified cobalt oxide nanoparticles was reported. Controllable electrodeposition process improved the catalytic performance of the fabricated CoOx/GPLE. The superior properties of the prepared electrocatalyst originated from the 3D and porous structure of GPLE, and high catalytic properties and stability of CoOx/GPLE. Owing to the ease of the preparation method, inexpensive materials and highly effective OER catalytic activity, the developed electrocatalyst is a promising candidate for water splitting and energy conversion devices.

References:

[1] Alaedini AH, Tourani HK, Saidi M. Journal of Environmental Management. 2023, 329- 334
[2] Ma X, Gao Y, Yang B, Lou X, Huang J, Ma L, et al. EMaterials Today Nano. 2023, 21-29
[3] Liang N-N, Han DS, Park H. Applied Catalysis B: Environmental. 2023, 324-331
[4] Soltani MM, Ahmadi P, Ashjaee M. Fuel. 2023,333- 345
[5] Hoang AT, Pandey A, Chen W-H, Ahmed SF, Nižetić S, Ng KH, et al. ACS Sustainable Chemistry & Engineering. 202321-52

[6] Hota P, Das A, Maiti DK. International Journal of Hydrogen Energy. 2023, 523-541
[7] Gopinath M, Marimuthu R. International Journal of Hydrogen Energy. 2022, 47- 62
[8] Li X, Sun X, Song Q, Yang Z, Wang H, Duan Y. International Journal of Hydrogen Energy. 2022, 19-42
[9] Ahmad H, Kamarudin SK, Minggu LJ, Kassim M. Renewable and Sustainable Energy Reviews. 2015, 599-610.
[10] Maeda K, Teramura K, Lu D, Saito N, Inoue Y, Domen K. Angewandte Chemie International Edition. 2006, 6-9
[11] Reghunath BS, Rajasekaran S, Devi K R S, Pinheiro D, Jaleel Uc JR. International Journal of Hydrogen Energy. 2023, 6-19
[12] Lin J, Han X, Liu S, Lv Y, Li X, Zhao Y, et al. Applied Catalysis B: Environmental. 2023, 321- 330
[13] Chen S, Zheng Z, Wang F, Wan H, Chen G, Zhang N, et al. ACS Sustainable Chemistry & Engineering. 2022, 89- 97
[14] Alves GF, de Faria LV, Lisboa TP, Matos MAC, Matos RC. Journal of Applied Electrochemistry. 2023, 39-48
[15] Lisnund S, Blay V. Materials Chemistry, 2022, 13- 27

Communications In Catalysis
Vol. 2, No. 1, 2023, pp.74-86
DOI: 10.22049/CIC.2023.28352.1032

Azarbaijan Shahid Madani University

Conducting Polymer Nanocomposites: Main Focus on Polyaniline-Based Photocatalysts

Zahra Pasandeh[1], Fahimeh Farshi Azhar [2,*]

[1,2]Applied Chemistry Research Laboratory, Department of Chemistry, Faculty of Basic Sciences, Azarbaijan Shahid Madani University, Tabriz, Iran

Corresponding author Tel.: +98 (41) 31452105, Fax number: +98 (41) 4327521

E-mail: fahimeh.farshi@gmail.com

Received: 2023-02-23, Accepted: 2023-03-19

Abstract

As a unique group of advanced polymer-based materials, conducting polymer nanocomposites combine the flexibility and conductivity of the polymer with the distinct properties of nanofillers. Conducting polymers have been widely investigated in various applications. Several conducting polymers, such as polyaniline (PANI), polypyrrole (PPy), poly (3,4- ethylenedioxythiophene) (PEDOT), and polythiophene (PTH) have been loaded with various semiconductor nanomaterials to prepare the composite photocatalysts. In this review, we summarized the synthesis, characterization, properties, and novel applications of conducting polymer nanocomposites especially photocatalytic degradation of hazardous chemicals. The synergic effect between conducting polymers and semiconductor nanomaterials were observed for a lot of composite photocatalysts.

Keywords: Conducting polymer nanocomposites, Polyaniline, Photocatalyst, Hybrid, Semiconductor nanomaterials

Introduction

Polymers were considered to be electrical insulators before the invention of conducting polymers (CPs) (conjugate polymers), but these organic polymers have unique electrical and optical properties similar to those of inorganic semiconductors. A conjugated carbon chain consists of alternating single and double bonds, where the highly delocalized, polarized, and electron-dense p bonds are responsible for its electrical and optical behavior. Typical CPs include polyacetylene (PA), polyaniline (PANI), polypyrrole (PPy), polythiophene (PTH), poly(para-phenylene) (PPP), poly(-phenylenevinylene) (PPV), and polyfuran (PF) (Figure 1) [1].

Conventional polymers consist of thousands to millions of monomer units. They are stiff and soluble in solvents, but a conjugated polymer chain consists of a lower number of monomer units. The mechanical property is gained by the presence of alternating single and double bonds present within it. The solubility and processability of CPs depend mainly upon the attached side chains, and the attached dopant ions give them mechanical, electrical and optical properties [2]. CPs are crystalline and partially amorphous. CPs consist of both localized and delocalized states, and the delocalization of p bonds depends heavily upon disorder, and this delocalization plays an essential role in the generation of charge carriers like polarons, bipolarons, solitons, etc., which are responsible for the transition from insulator to metal [3]. The conductivity of conjugate polymers acts like an insulator to a semiconductor in their pure form, and the conductivity increases with dopant concentration. In the undoped state, they behave as an anisotropic, quasi-one-dimensional electronic structure with a moderate bandgap of 2–3 eV like a conventional semiconductor and they exhibit the electrical and optical behavior of semiconductors along with the mechanical action of typical polymers. When conjugated polymers undergo doping or photoexcitation, the p bond gets self-localized to undergo nonlinear excitation as polarons, solitons, bipolarons, etc., and the polymer transforms from a nonlinear excitation state to a metallic state [4]. Research on CPs is one of the hotspots in the field of materials due to their special polymeric structures and fascinating electrical, optical, mechanical, and biological properties, hence, they have been widely applied in many fields such as biotherapy, chemical/biological sensors, photo-/electrocatalysis, energy storage and conversion devices, electromagnetic shielding, and so on [5].

In comparison to conventional semiconductors, CPs possess unique bonding structures along the polymer backbones, consisting of alternating double (p) and single (s) bonds which endow them semiconducting properties. Once doped, the p-systems accommodate negative or positive charges that can pair with the dopants to form polarons, and can further be oxidized to bipolarons (supporting the transport of both holes and electrons) [6].

Conducting polymer nanocomposites are a class of hybrid materials synthesized using CPs with some inorganic materials of different sizes and nature using some chemical or electrochemical techniques giving rise to a new hybrid material with fascinating properties and significant application potential.

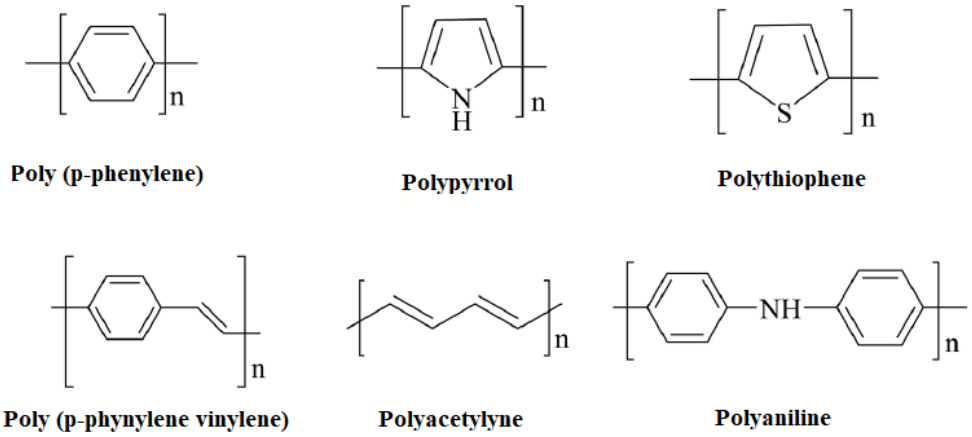

Figure 1. Structural illustration of different conducting polymers.

Conducting polymer nanocomposites has emerged as a boost and opened new doors for researchers in wide applications in the field of wastewater treatments, optoelectronic devices, batteries, electrochromic devices, biomedical materials, and devices such as sensing, imaging, etc [7].

Current research activities are highly focused towards the development of facile techniques for waste water remediation. Semiconductor based photocatalysis has been chosen as one of the promising methods for the degradation of toxic pollutants from the wastewater. Recently, CPs and its nanohybrids have attracted much attention due to their electrochemical properties, photo-stability, low cost, and efficacy. The nanohybrids of CPs with metal, metal oxides and other semiconductor materials have shown excellent photocatalytic activity for the degradation of toxic organic pollutants including dyes, pesticides and pharmaceuticals drugs [8]. In the present review, a brief overview of the concept of conducting polymer nanocomposites is provided with the synthesis methods, applications in various fields. Special emphasis has been given to application of polyaniline-based nanocomposites in photocatalytic degradation of hazardous materials.

Conducting polymer nanocomposites

In comparison with conventional polymeric materials, conducting polymer nanocomposites (CPNCs) have gained increasing interests due to their improved electrochemical behavior, facile synthesis, biocompatibility, large surface area, high electrical conductivity, elevated carrier transport, and unique optical behaviors. Previously, multi-sided CPNCs with varying architecture and morphologies have undergone synthetization, to form nanomaterials including 0D (nanoparticles, nano-spheres), 1D (nano-ribbons, nanorods, nano-wires, nanofibers, nano-belts, and hollow structured nanotubes), 2D (nano-rings, nanosheets, nano-discs, nano-clips). Numerous physical and chemical techniques have been utilized for fabrication of nanocomposites, including physical template synthesis (i.e., hard and soft method), and template-free approach (i.e., self-assembly or interfacial polymerization, electrospinning, seeding approach) [9, 10].

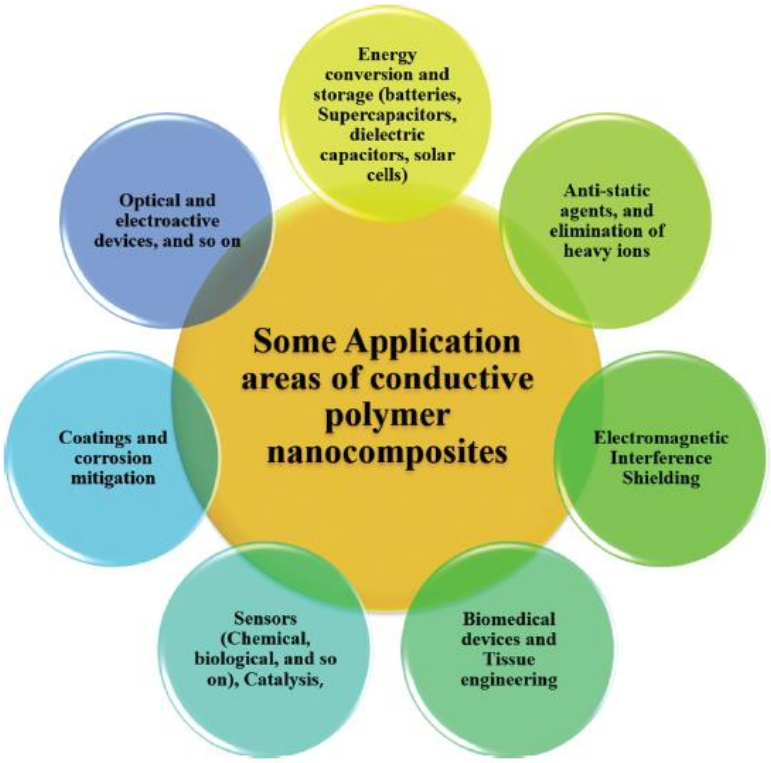

Figure 2. Some applications of CPNC [12]

Parameters to be considered in CPNCs development include charge transferring mechanism and charge mobility procedure during occurrence of redox reactions which result in excellent electrical behavior. Moreover, the doping procedure can notably escalate charge carrier entities, while enhancing conductivity. The basic attribute of CPs involves enlarged π conjugated mechanism along the polymeric chain which endows metallic propensity to their behaviors relative to electronics, magnetic and optical properties. Nevertheless, CPs also exhibit similar properties of conventional polymeric materials, such as good mechanical behavior, environmental stability, low temperature of processing, inexpensiveness, and so on. Moreso, it is essential to synthesize CPNCs to completely utilize inherent advantages in overcoming deficiencies, such as solubility. CPs ability to conduct and undergo solubility is managed through modification of their chemical architectures [11].

Nanocomposites fabricated through CPs comingling with varying nanomaterials, including metallic entities such as Ag, Au and Pd, metallic oxides including Fe_2O_3, MnO_2, NiO, CuO, TiO_2, WO_3, ZnO, SnO_2, V_2O_5, RuO_2, and chalcogenides including MoS_2, WS_2, Bi_2S_3, CdS, CdSe, CdTe, along with carbon derivatives such as graphene (GN), graphene oxide (GO), carbon fibers (CF) and nanotubes (CNT), and other nil-conductive polymeric materials, have been broadly elucidated. Fabrication of CPNCs exhibiting elevated mechanical behavior, flexibility, and conductivities have demonstrated CPs capacity to serve as major material parts in light-emitting diodes, transistors, electrochromic devices, actuators, electrochemical capacitors, photovoltaic cells, and sensors. Enhanced properties of CPNCs have resulted broad applications in energy conversion and storages (batteries,

supercapacitors, dielectric capacitors, solar cells, fuel cells), chemical sensors, biosensors, catalysis, optical devices, electro-active devices, biomedical devices, electromagnetic interference shielding, corrosion protection, antistatic agent, removal of heavy metal ions, tissue engineering and other applications as schematically elucidated in Figure 2 [12].

Mechanism of CPs polymerization

Oxidative cross-linking of monomers is used in synthesizing CPs. From a polymerization perspective, the initial step is monomer oxidation resulting in formation of a radical cation, which subsequently reacts with another monomeric entity or radical cation, resulting in formation of a dimer. This is a vital approach in initiation procedure of polymerization. There are three main routes of initiation vis-a-viz, chemically initiated, electrochemically attained, and photo-induced oxidation, whereby individual routes showcase their own merits and demerits. From the perspective of the first approach, oxidation of the monomer is attained using chemically oxidizing entities such as ammonium persulfate or ferric chloride. From the perspective of the second approach, monomeric entities undergo electrochemical oxidization, while in third approach, light enables the monomeric oxidization using a photo-initiator [13].

Techniques used in synthesis of CP nanocomposites

Relative to mechanism and fabrication procedures, techniques utilized in fabrication of CPNCs may be categorized into three main classes: (i) ex-situ or sequestered synthesis, (ii) in-situ or sequential synthesis, and (iii) single-pot or concurrent synthesis, as shown in Table 1 [14].

The major attribute of all the techniques detailed in the first classification is that the CPs and inorganic entities undergo individual synthetization, while hybridization is attained during next step via simplified or more intricate co-mingling of two or more entities where interfacial tension between varying entities determines notable properties of the resultant nanocomposite. These processes are simplified and normally highly appropriate for solution-oriented processing, which is a stepping-stone for enhancing mass production and processing using roll-to-roll printing. Added merit of this technique is the well-known synthesis step where each entity is individually fabricated using a well-established approach. Numerous other techniques exist for the hybridization procedure, ranging from very simplified approaches such as mechanical mingling of the two components, to highly intricate techniques such as ligand exchange preparation steps. Moreso, physical inculcation of CPs into inorganic nanomaterials can also be attained, resulting in highly aligned nanoarchitectures. However, this procedure is not simple because of the possibility of hindering the polymeric entities from penetrating the cavities of the nano-architecture host as a result of high interfacial tension because of physical constrains such as the hydro-dynamic polymeric radius, resulting in incomplete cavity filling where very poor pore filling ratios as low as 0.5% were attained [12, 15, 16].

Table 1. Techniques of synthesizing CP nanocomposites [12]

Main Croup	Merit	Demerit	Example
Ex-situ synthesis	Simplified Solution processability	Restrained usage, inferior control of the contact between each component	Mechanical mixing Layer-by-layer deposition
In situ synthesis	Variable approaches relative to Chemical or electrochemical approach. Facile control of numerous parameters	Highly complex due to consideration of many parameters	In-situ polymerization. Electrodeposition. In situ reduction
Single pot synthesis	Simplified and brief processing duration	Constrained control over architecture and morphology of the products	Redox reaction Co-deposition

Properties and multifunctional applications of CP nanocomposites

CPNCs display enhanced properties such as improvement in batteries and super-capacitors electrolytic diffusion, enhancement in dielectric behavior of ferroelectric polymeric-oriented capacitors, facilitating efficient dissociation in solar cells, minimization in response duration, and improvement in biosensors and chemical sensors sensitivity and increased corrosion inhibition. Additionally, the representative researches in CPNCs for specialized devices are also highlighted, as schematically illustrated in Figure 3 [17].

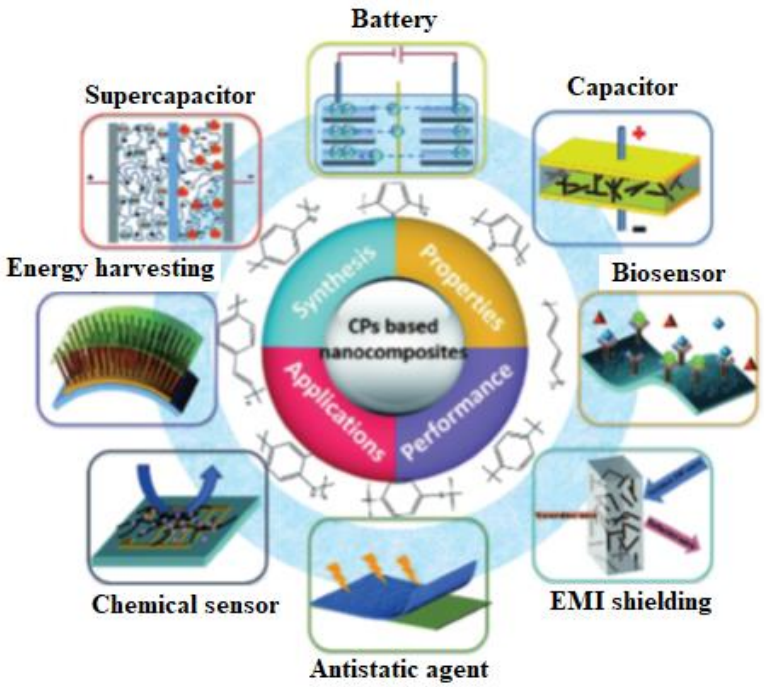

Figure 3. Elucidation of CPs nanocomposite applications [12]

Photocatalytic activity of CP nanocomposites

Water pollution has emerged as a serious problem all over the world due to the increased agricultural, industrial and domestic activities. The quality of river and ground water has undergone immense deterioration due to the pollution by hazardous wastes. These toxic pollutants have significantly affected the human health and the quality of the ecosystem. The major sources of water pollution include heavy metal ions, dyes, phenols, polychlorinated biphenyls (PCBs), haloacetic acids (HAAs), pharmaceutical drugs, pesticides, disinfection byproducts (DBPs), and other synthetic chemicals [18].

Among different methods to removal of these pollutants, advanced oxidation process (AOP) has been extensively reviewed for complete decomposition of organic pollutants through the generation of reactive oxidants/radicals such as $^{\bullet}OH$, $O_2^{\bullet-}$, etc. under different sources of light irradiation (UV, visible, microwave and solar light) [19]. Heterogeneous semiconductor photocatalysis is reported to be of low cost, eco-friendly as well as facile method for waste water treatment.

Inorganic metal oxides such as V_2O_5, MnO_2, WO_3, Nb_2O_5, SnO_2, TiO_2, ZnO, Fe_2O_3, and Fe_3O_4 have been extensively reviewed in literature for water treatment processes. However, these oxides face some serious challenges in the large scale application process such as inactivity under visible light, faster electron-hole recombination and presence of a large band gap [20, 21]. Significant approaches have been implemented for band gap modification to prevent the recombination of photo-generated electron–hole pair and improve the photocatalytic under visible light. The utilization of CPs as sensitizing agents has been shown to rapidly improve the photocatalytic activity due to the presence of p-conjugated systems containing electron rich species, which help in inserting electrons into the conduction band (CB) of most inorganic semiconductor oxides [22].

CPs possesses metallic conductivity and mechanical characteristics similar to metals/metal oxides. The conjugated one-dimensional structure of CPs offers outstanding electrical, optical and electronic properties, which are widely used for catalytic purpose [23]. Hence recent literature has been focused on the synthesis and application studies of the CP based nanocomposites, which show immense potential for environmental remediation in terms of facile synthesis, enhanced photocatalytic activity, reduced electron-hole recombination and variation of photocatalytic activity under UV–visible and solar light irradiation [24].

Photocatalytic mechanism of semiconductors under UV light irradiation

The photocatalytic activity of a material usually depends on its ability to create electron- hole pairs, which generate $^{\bullet}OH$, $O_2^{\bullet-}$ that can attack the pollutants via secondary reaction. Photocatalytic reaction is usually subjected to the wavelength of light (photon) energy as the irradiation of light stimulates redox process of electron-hole generation [25]. Schematic representation of metal oxides-based semiconductors photocatalytic mechanism is shown in Figure 4.

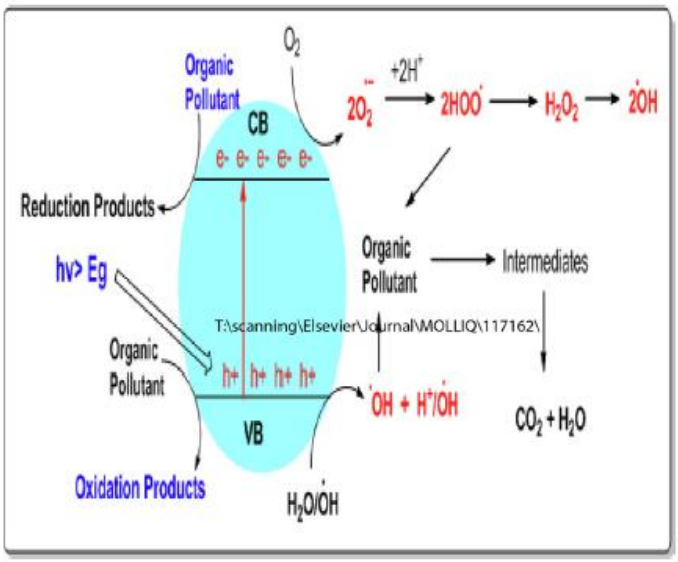

Figure 4. Schematic representation of metal oxides-based semiconductors photocatalytic mechanism [8].

The fundamental steps in the process of semiconductor photocatalysis are:

- Photoexcitation which is initiated by the photoelectrons that get promoted from the valence band (VB) of a semiconductor to the empty conduction band (CB) triggered by the source of irradiation.

Metal oxides semiconductor (MOS) + hυ (UV)→MOS[e^-(CB)+h^+(VB)] (1)

- Ionization of water: This occurs when the holes at VB react with water molecules to produce $^\bullet$OH radicals, as shown below:

$H_2O+h^+(VB)\rightarrow {}^\bullet OH+H^+$ (2)

These radicals attack the organic pollutants and result in the formation of fragments.

- Oxygen ion sorption: in this step the electron (e^-) in the CB is taken up by the oxygen to produce $O_2^{\bullet-}$.

$O_2+e^-(CB)\rightarrow O_2^{\bullet-}$ (3)

- Protonation of superoxide The $O_2^{\bullet-}$ radical undergoes protonation forming hydroperoxyl radical (HO_2^-) which degrades into hydroxyl radicals.

$O_2^{\bullet-}+H\rightarrow HOO$ (4)

$2HOO\rightarrow H_2O_2+O_2$ (5)

$H_2O_2\rightarrow 2{}^\bullet OH$ (6)

$Organicpollutant+OH\rightarrow CO_2+H_2O$ (7)

3.2. Role of conducting polymers (CPs) in photocatalysis

The rapid rate of photo-generated electron-hole pair recombination is prevented by the use of CPs as they help in tuning the band gap of semiconductors. As per density functional theory (DFT) calculations, CPs serve as low-band gap materials with wide adsorption spectra under visible light making them active photocatalysts under this source of irradiation [26]. Various metal oxides have been combined with CPs mainly comprising of PANI, PTH, PPy, poly(1-naphthylamine) (PNA), poly(ophenylenediamine) (POPD), polycarbazole (PCz), polyacetylene (PA) etc. to improve their photocatalytic performance. CPs can act as p-type and form a p-n junction with metal oxide to control the electron-hole recombination [27]. The photocatalysis of contaminants with CPs and CP based nanocomposites exhibit the first-order reaction kinetics as reported in most of the studies.

Table 2. Photocatalytic characteristics of pristine conducing polymers [8].

CP	Contaminant (s)	Light	% Removal/ time
PNA	Methyl orange (MO)	Microwave	84%, 96%/ 15 min
PANI	Acid orange 7 (AO)	Microwave	65% /10 min
PEDOT	Metformin and PPCPs	UV light	99% /60 min
PNA nanotubes	Comassie Blue (CB) dye	Solar light	55% /60 min
PPy	Phenol	UV light	100% /4.5 h
Poly (3-hexylthiophene)(P3HT)	Phenol	UV and visible light	92% /240 min

Photocatalytic performance of pristine CPs

The studies conducted by the Riaz et al. [28], Ghosh et al.[29] and Yuan et al. [30] have shown that PNA, PANI, POPD, PCz, PEDOT and PPy nanostructures show excellent photocatalytic activity for removal of dyes and phenol. Kumar et al. [31] reported the photocatalytic degradation of mixture of PPCPs by PEDOT under UV light and found 99% degradation efficiency within very short time. Table 2 presents a comprehensive overview of photocatalytic activity of CPs.

Photocatalytic performance of CP based nanohybrids

The nanocomposites of CPs with metal oxides and other supporting material have shown excellent photocatalytic performance under different light irradiation. The hybrid material usually has high photo-response and delayed recombination of charge carriers. The hybrid system of CPs with metal oxides has distinct exciton-plasmon interactions and exhibit higher surface area for high absorption. Therefore, the current research focus has been on hybrid material development for increasing the efficiency of photocatalysis. PANI, PPy, PTh, PCz, PNA and PEDOT based nanocomposites are the most studied photocatalysts for waste water remediation.

Polyaniline based nanohybrids

PANI is one of most investigated conducting polymers among all CPs due to its high conductivity, facile synthesis procedure and good environmental stability. The research group of Riaz and coworkers [32] prepared PANI/SnO_2 nanohybrids via ultrasound assisted chemical polymerization using SnO_2 nanoparticles extracted from Psidium Guajava. The nanohybrids were tested as catalysts for the degradation of dichlorodiphenyltrichloroethane (DDT). Around 97wt% of DDT degradation was achieved within a very short period of 12 min under microwave irradiation. Similarly, Wang and Min [33], Chen et al. [34] and Reddy et al. [35] synthesized PANI/TiO_2 nanohybrids which showed higher photocatalytic efficiency as compared to pristine PANI or TiO_2 for the degradation of methylene blue (MB) as well as Rhodamine B (RhB) dye. The PANI/TiO_2 nanohybrids showed degradation efficiency of 81.74% for MB and 99 % for RhB under visible light irradiation. Gulce et al. [36] prepared PANI/CdO nanocomposites in aqueous solution of diethylene glycol via chemical oxidative polymerization method and

investigated its photocatalytic activity against the MB and malachite green (MG) dyes under UV light and natural sunlight irradiation. Photocatalytic decolorization rate was increased up to 7 times by the addition of CdO with PANI. Around 99% degradation efficiency was achieved under natural sunlight irradiation within 60 min. The nanocomposites of PANI with ZnO were also prepared by few researchers and these nanocomposites were reused multiple times in photocatalytic degradation process with a minimal loss of its catalytic reactivity [37]. Qin et al. [38] investigated the photocatalytic activity of MB dye under visible light irradiation. PANI/ZnO showed significantly enhanced photocatalytic properties, the reaction rate constant was found to be 0.01944 min^{-1} which was higher than the pure ZnO (0.00245 min^{-1}) and PANI (0.00585 min^{-1}). Mitra et al. [39] investigated the photocatalysis of dyes with aluminium-doped ZnO-PANI hybrids. They found that beyond an optimum weight percentage of Al-ZnO, there is a significant decrease in the photocatalytic activity of the hybrid. The synergistic effect of PANI and Al-ZnO led to higher photocatalytic activity. Cheng et al. [40] synthesized Ag-Cu_2O/PANI using a simple, low-cost process and results showed that the Ag–Cu_2O/ PANI exhibited a high long-term antibacterial activity against *S. aureus* and *P. aeruginosa*. Kadi et al. [41] developed core shell like CeO_2/PANI nanocomposites and the photocatalytic degradation efficiency of the synthesized nanocomposites was investigated against the degradation of nitrobenzene under visible light irradiation. The photocatalytic performance of CeO_2/PANI nanocomposite was found to be 6.6 times higher than PANI and 14.3 times higher than CeO_2. PANI based nanocomposites doped with $SrTiO_3$ were explored by Shahabuddin et al. [42] for the degradation of MB dye. Results showed that the degradation efficiency of nanocomposites which were doped with the $SrTiO_3$ nanocubes was higher than that of the undoped PANI and around 97% degradation efficiency was achieved after 90 min under solar light irradiation. Shang et al. [43] and Wu et al. [44] explored PANI/bismuth oxide, PANI/Bismuth vanadate ($BiVO_4$), and PANI/bismuth niobite Bi_3NbO_7 nanocomposites. They noticed remarkable photocatalytic ability with high organic carbon content removal ability of the nanocomposite. Bu and Chen [45] investigated PANI/Ag/Silver phosphate (Ag_3PO_4) hetero-structure formed through in-situ deposition of Ag_3PO_4 nanoparticles on PANI chains and concluded that the nanocomposite had superior photocatalytic ability and stability because of an improved interfacial electric field resulting in profound electron-hole separation and migration efficiency. They found Ag formation on the PANI surface because of PANI assisted reduction of Ag^+ to Ag^0, which played an important role in the separation of photo-generated electron and holes. Studies on PANI/graphene and graphene oxides also reported excellent photocatalytic activity under visible light radiation for the degradation of toxic organic pollutants [46]. Zhang et al. [47] developed PANI nanorods arrays on graphitic carbon nitride (g-C_3N_4), and showed superior photocatalytic activity under visible light. Pandiselvi et al. [48] reported carbon nitride/polyaniline/ZnO

composite with excellent photocatalytic ability under visible light for degradation of dyes.

Conclusion and future prospects

Conducting polymers and their nanocomposites have proven to be promising photocatalysts for decontaminating water. The role of CP based nanocomposites as photocatalysts are dependent upon the radical generation and transfer of photoelectrons to CB of the metal oxides. Among pristine CPs, PANI was noticed to show high catalytic activity. Similarly, among PANI nanohybrids, superior catalytic activity was noticed for PANI/SnO_2. Hence the photocatalytic activity could be tuned to obtain optimum performance under UV/visible/solar or microwave irradiation. For future work, the design of metal ferrites/metal oxides nanoparticles via green routes and its nanohybrids with CP could be attempted and compared with the commercially available nanomaterials. The application of these green route derived nanohybrids materials is expected to add value to the knowledge pool of basic scientific research as well as technological development dealing with the designing of photocatalytic nanohybrids. These nanohybrids materials could also be developed at industrial scale for catalytic degradation of pollutants under microwave and visible light irradiation.

Acknowledgements

The authors acknowledge the research office of Azarbaijan Shahid Madani University for financial support.

References

[1] Namsheer K., Rout, C. S. RSC Adv. 2021, 5659-5669

[2] Skotheim T. A., Handbook of conducting polymers, CRC press, 1997.

[3] Le T. H., Kim Y., Yoon H., Polymers, 2017, 150-169

[4] Kohlman R. S., Epstein A. J., Skotheim T. A., Elsenbaumer R. L., Reynolds J. R., Handbook of Conducting Polymers. Marcel Dekker, New York, 85, 1998.

[5] Zhao, F., Shi, Y., Pan, L., Yu, G. Acc. Chem. Res. 2017, 1734-1745

[6] Xue, Y., Chen, S., Yu, J., Bunes, B. R., Xue, Z., Xu, J., Zang, L. J. Mater. Chem. C, 2020, 10136-10152

[7] Jadoun, S., Chauhan, N. P. S., Chinnam, S., Aepuru, R., Sathish, M., Chundawat, N. S., Rahdar, A. Biomed. Mater. Dev. 2022, 1-9

[8] Zia, J., Riaz, U. J. Mol. Liq. 2021, 340-357

[9] Fan, P., Wang, S., Liu, H., Liao, L., Lv, G., Mei, L. Electrochim. Acta, 2020, 331-350

[10] Shaheen, I., Ahmad, K. S., Zequine, C., Gupta, R. K., Thomas, A. G., Malik, M. A. J. Energy Storage, 2020, 29-47

[11] Singh, P., Shukla, S. K. J. Mater. Sci. 2020,1331-1352

[12] Idumah, C. I., Ezeani, E. O., Nwuzor, I. C. Polym.-Plast. Technol. Mater. 2021, 756-771

[13] Nguyen, D. N., Yoon, H. Polymers, 2016, 118-135

[14] Tomboc, G. M., Kim, H. Electrochim. Acta, 2019, 318-325

[15] MacDiarmid, A. G. Angew. Chem. Int. Ed. 2001, 2581-2596

[16] Martin, C. R. Acc. Chem. Res. 1995, 61-75

[17] Zhang, L., Du, W., Nautiyal, A., Liu, Z., Zhang, X. Sci. China Mater. 2018, 303--314
[18] Haseena, M., Malik, M. F., Javed, A., Arshad, S., Asif, N., Zulfiqar, S., Hanif, J. Environ. Risk Assess. Remed. 2017
[19] Chong, M. N., Jin, B., Chow, C. W., Saint, C. Water Res. 2010, 2997-3006
[20] Khan, M. M., Adil, S. F., Al-Mayouf, A. J. Saudi Chem. Soc. 2015, 462-481
[21] Serpone, N. A. V. E., Emeline, A. V. J. Phys. Chem. Lett. 2012, 673-689
[22] Lee, S. L., Chang, C. J. Polymers, 2019, 206-218
[23] Kumar, R., Singh, S., Yadav, B. C. Int. Adv. Res. J. Sci. Eng. Technol. 2015, 110-125
[24] Lu, X., Zhang, W., Wang, C., Wen, T. C., Wei, Y. Prog. Polym. Sci. 2011, 671-691
[25] Zhu, D., Zhou, Q. Environ. Nanotechnol. Monitor. Manag. 2019, 12-21
[26] Kashyap, J., Riaz, U. RSC Adv. 2018, 13218-13227
[27] Kumar, R., Travas-Sejdic, J., Padhye, L. P. Chem. Eng. J. Adv. 2020, 100047-100056
[28] Riaz, U., Ashraf, S. M., Aqib, M. Arab. J. Chem. 2014. 79-87
[29] Ghosh, S., Mallik, A. K., Basu, R. N. Solar Energ. 2018, 548-557
[30] Yuan, X., Floresyona, D., Aubert, P. H., Bui, T. T., Remita, S., Ghosh, S., Remita, H. Appl. Catal. B Environ. 2019, 242- 284.
[31] Kumar, R., Akbarinejad, A., Jasemizad, T., Fucina, R., Travas-Sejdic, J., Padhye, L. P. Sci. Total Environ. 2021, 751-769
[32] Riaz, U., Zia, J. Environ. Pollut. 2020, 259-268
[33] Wang, F., Min, S., Han, Y., Feng, L. Superlattices Microstruct. 2010, 170-185
[34] Chen, X., Li, H., Wu, H., Wu, Y., Shang, Y., Pan, J., Xiong, X. Mater. Lett. 2016, 172-179
[35] Reddy, K. R., Karthik, K. V., Prasad, S. B., Soni, S. K., Jeong, H. M., Raghu, A. V. Polyhedron, 2016, 120-169.
[36] Gulce, H., Eskizeybek, V., Haspulat, B., Sarı, F., Gülce, A., Avcı, A. Ind. Eng. Chem. Res. 2013, 10924-10938
[37] Ameen, S., Akhtar, M. S., Kim, Y. S., Yang, O. B., Shin, H. S. Colloid Polym. Sci. 2011, 289-299
[38] Qin, R., Hao, L., Liu, Y., Zhang, Y. ChemistrySelect, 2018, 6286-6295
[39] Mitra, M., Ghosh, A., Mondal, A., Kargupta, K., Ganguly, S., Banerjee, D. Appl. Surf. Sci. 2017, 402-418.
[40] Ma, C., Yang, Z., Wang, W., Zhang, M., Hao, X., Zhu, S., Chen, S. J. Mater. Chem. C, 2020, 2888-2897
[41] Kadi, M. W., Mohamed, R. M. Front. Nanosci. Nanotech. 2019, 5-18
[42] Shahabuddin, S., Muhamad Sarih, N., Mohamad, S., Joon Ching, J. Polymers, 2016, 27-41
[43] Shang, M., Wang, W., Sun, S., Ren, J., Zhou, L., Zhang, L. J. Phys. Chem. C, 2009, 20228-20239
[44] Wu, W., Liang, S., Shen, L., Ding, Z., Zheng, H., Su, W., Wu, L. J. Alloys Compd. 2012, 213-220
[45] Bu, Y., Chen, Z. ACS Appl. Mater. Interfaces, 2014, 17589-17596
[46] Ma, J., Dai, J., Duan, Y., Zhang, J., Qiang, L., Xue, J. Renew. Energ. 2020, 1008-1019
[47] Zhang, S., Zhao, L., Zeng, M., Li, J., Xu, J., Wang, X. Catal. Today, 2014, 224-237

[48] Pandiselvi, K., Fang, H., Huang, X., Wang, J., Xu, X., Li, T. J. Hazard. Mater. 2016, 3